The Dissertation Committee for Elizabeth Ann Collister Certifies that this is the approved version of the following dissertation:

Studies of Nontraditional High Resolution Thin Film Patterning Techniques

Committee:

C. Grant Willson, Supervisor

Roger Bonnecaze

John Ekerdt

Thomas Truskett

Gerard Schmid

Studies of Nontraditional High Resolution Thin Film Patterning Techniques

by

Elizabeth Ann Collister, B.S.

Dissertation

Presented to the Faculty of the Graduate School of

The University of Texas at Austin

in Partial Fulfillment

of the Requirements

for the Degree of

Doctor of Philosophy

The University of Texas at Austin

May, 2009

Dedication

To my family.

Acknowledgements

The work within this document would not have been possible without the support I received from my family, fellow group members and teachers. I would not be the person I am today without the love of knowledge, strong work ethic, and curiosity instilled in me by my parents. My graduate career was mainly shaped by my supervisor Dr. Willson who continued to indulge my curiosity and took great efforts to expand my knowledge base outside my research area.

My research was aided by many members of the Willson research group. My main collaborator was Michael Dickey, whom served as a mentor as well as a collaborator. My work was aided immensely by the machine fabricated by Allen Raines. My synthesis work was successful due to the guidance of Matthew Pinnow, Nick Connely, and Brian Long. Fabrication of experimental materials would not have been possible with the resources of the microelectronics research center and with training from the staff, particularly Marylene Palard and Johnny Johnson. Help was also rendered by Mike Ronalter of the glass shop. I also have to thank Dr. Hoyle of the University of Southern Mississippi for the donation of materials.

My modeling work was accomplished through the guidance of Jason Meiring and a large group of individuals from I.C.E.S.. Of these, Paul Bauman and Chetan Jhurani provided both support by contributing code as well as teaching me more advanced coding

methods. Other members of the I.C.E.S. team: Dr. Oden, Serge Purdhomme, Dr. Rodin, Dr. Demkowicz, and John Bass played a large part in shaping the mechanics of the code. The running of the simulations was aided by the availability of the resources at TACC.

I would like to thank my mentors and teachers throughout the years for their advice and support: Dr. Kathy Chung at NASA Glenn who gave me my first taste of working in a research lab, and Dr. John Merrick at NASA Glenn, who arranged for me during my internship to visit other labs throughout NASA Glenn and talk to the researchers. My undergraduate professors Dr. Lupina, Dr. Evans, and Dr. Ju who once they learned I was going to go to graduate school continued to give their advice and always had an open door. I also like to thank my committee from their support and time.

Studies of Nontraditional High Resolution Thin Film Patterning Techniques

Publication No._____

Elizabeth Ann Collister, Ph.D.

The University of Texas at Austin, 2009

Supervisor: C. Grant Willson

This thesis discusses two patterning techniques: Step and Flash Imprint Lithography, a nanoimprint technique, and patterning thin films utilizing electrohydrodynamic instabilities.

Step and Flash Imprint Lithography, SFIL, is promising alternative approach to photolithography. SFIL replicates the relief pattern of a template in a photocurable liquid that has been dispensed on a substrate. The pattern is then crosslinked when the photocurable liquid is exposed to UV light through the template.

In order to study the volume change in the created features upon exposure, a stochastic mesoscale model was formulated. This model allows the study of the possibility of defects forming, from under cured etch barrier, or particle contamination of the template. The results showed large defects should not occur regularly until the minimum feature size is below 3 nanometers. The mesoscale model proved to computationally intensive to simulate features of engineering interest.

A base multiscale model was formulated to simulate the effects of the densification of the photocurable liquid as well as the effects of the polymerization on the feature integrity. The multiscale model combines a continuum model (compressible Mooney-Rivlin) coupled to the mesoscale code using the Arlequin method. The multiscale model lays the framework that may be adapted to the study of other SFIL processes like template release.

Patterning thin films utilizing electrohydrodynamic instabilities allows for the creation of periodic arrays of pillar like features. These pillars form due to the electric field destabilizing the thin film. Prior work has focused on utilizing polymeric films heated above their glass transition temperatures.

In order to decrease the process time in the pillar formation process, work was done to study photocurable systems. The systems which proved favorable to the pillar creation process were the thiol-ene system as well as the maleimide systems. Further work was done on controlling the packing and ordering of the formed pillar arrays by using patterned templates. The result of these studies is that control was only able to be achieved to the third generation of pillars formed due to the inability to fully control the gap over the entire active area.

Table of Contents

List of Tables

List of Figures

Chapter 1

The patterning of thin films is a technique important to a wide variety of industries, such as the microelectronics industry. It is used to create devices such as microelectromechanical systems (MEMS), patterned media for magnetic data storage, photonic devices, and the many layers of patterned materials that make up computer chips. Photolithography has been the work horse of the electronics industries since the 1960s. This technique has enabled the industry to continually chase the bench marks provided by Moore's Law[1], which states that the number of transistors on a chip double every two years (Figure 1.1).

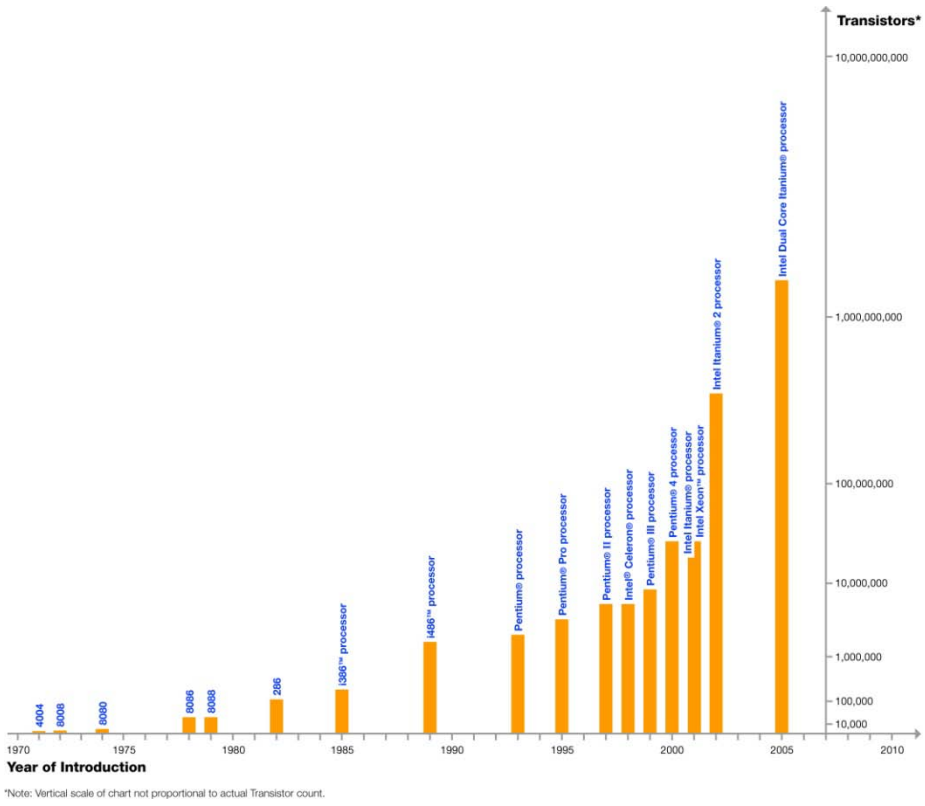

Figure 1.1. Copyright 2005 Intel Corporation; Moore's law illustrated through the Intel processor line.

1.1 PHOTOLITHOGRAPHY

Photolithography is a process used to pattern thin films through the selective exposure of the film to ultraviolet (UV) light. The process generally begins by coating a thin film of photoresist onto a substrate, typically a silicon wafer. The "photo" portion of the name refers to the fact that when exposed to light of a specific wavelength, a chemical change takes place in the film causing areas that are exposed to either become soluble in some developer (positive tone) or become insoluble in some developer (negative tone), see Figure 1.2 . The "resist" portion of the term photoresist refers to the ability of the patterned features to withstand the etch medium during the image transfer of the features into the underlying layer.

Besides tone, photoresists can be further categorized as one-component or two-component systems. In one-component systems, a pure polymer is used. This polymer must respond to the exposure to light, be able to resist etch, have good adhesion to the substrate, and form uniform films. Poly(methyl methacrylate) is a common one-component resist system. In two-component systems, the polymer generally acts as an inert matrix, which has good adhesion properties and has good thermal and chemical resistance. The second component is a photoactive compound (PAC), which slows or inhibits the dissolution rate of the resist. The novolac-diazonapthoquinone (DNQ) system is a good example of a positive tone two-component system. Novolac is a phenolic polymer that is soluble in aqueous base. Adding up to 10 to 20% w/w of DNQ to Novolac causes it to dissolve an order of magnitude slower, thus DNQ is known as a dissolution inhibitor. When DNQ is exposed to light the resulting photoproduct is an acid, which is soluble in aqueous base. Thus, novolac is also soluble in aqueous base a positive tone image is formed.

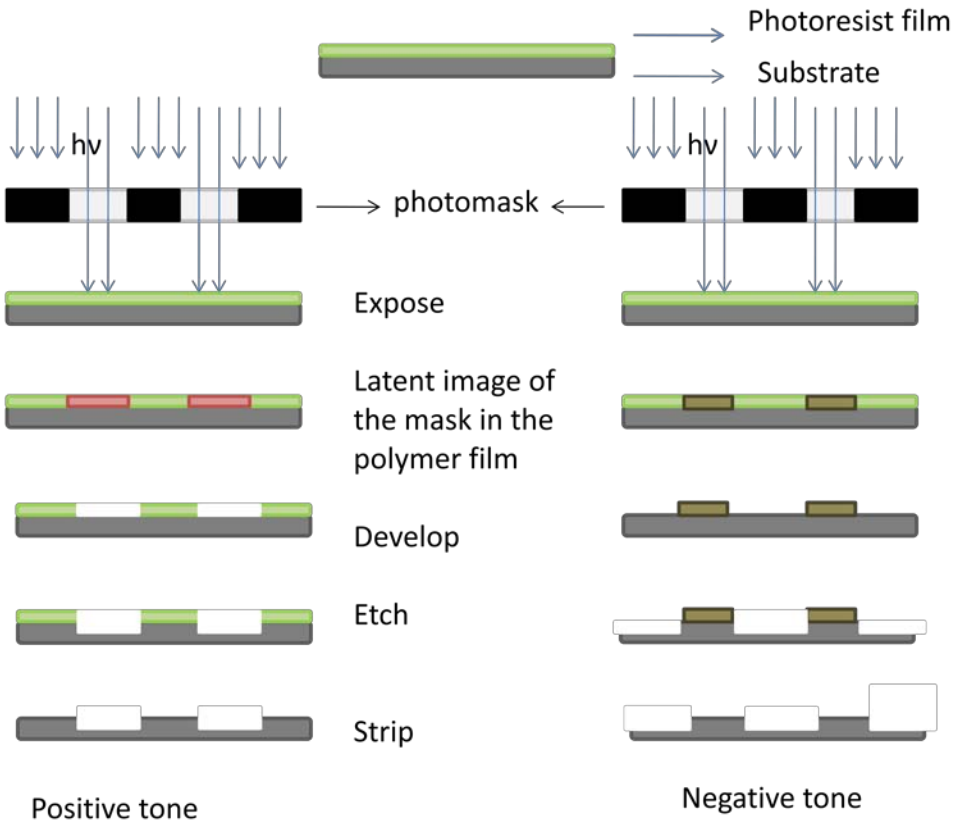

Figure 1.2. The depiction of the process steps in the patterning of a photoresist film. The film is first coated onto a substrate. It is then exposed to UV light through a photomask. This will create a latent image (colored areas in the picture) of the mask in the polymer film. Depending on the tone of the resist, the exposed areas will either become soluble, left, or insoluble in a developer solvent, right. The feature is then transferred into the underlying layer via an etch process. Finally, the remaining photoresist is stripped off the substrate.

In order to selectivity expose the film to light a photomask, which is usually a glass or quartz substrate that has a chromium pattern on it, is employed. An image of the mask is focused into the photoresist by a projection system that reduces the image on the mask by 4X when it exposes the photoresist film. The masks are typically made using electron beam lithography.

In order to keep up with Moore's law, continuous improvement has had to be made in the field of lithography. Each technology cycle or node has relied on some combination of new resist materials, a new exposure source wavelength, and/or improvements to the machines and lenses involved in the process. The governing equation guiding this process is the Rayleigh criteria:

$$R = \frac{k * \lambda}{NA} \qquad (1.1)$$

where R is the resolution limit or the minimum feature size that can be produced, k is a constant of the lithographic process, λ is the wave length of light utilized, and NA is the numerical aperture of the lens used. The wavelength of light utilized has progressed from 436 nm in 1980 to 365 nm in 1988, to 350 nm in 1994, to 248 nm in 1998, to the current 193 nm.[3] The NA of the lens system has increased from 0.1 to today's 1.3 and k has increased from approximately 0.8 to 0.3. New resist materials were required with increased sensitivity as power output dropped with each change in wavelength. This led to more complicated chemistries. The initial films simply cross-link upon exposure. The current systems are based on chemically amplified resists (CAR), which rely on an acid catalyzed deprotection reaction to induce the solubility change and give the system gain.[2]

The CAR system is a two component system in which the resist has protecting groups which stop the resist from being soluble in developer. These protecting groups are acid liable. The second component is a photoacid generator, which upon exposure to UV light decomposes into an acid molecule. After exposure the film, the post exposure bake allows the acid to move in the film and remove the protecting groups from the

resist. This leads to the gain in the system since one acid molecule can deprotect many sites on the resist.

A road block appeared when trying to migrate to 157 nm wavelength exposure source, due to stringent needs for a nitrogen environment, new lens materials and new resist materials so the industry had to look at other technologies to continue the chase toward smaller structures.

The International Technology Roadmap for Semiconductors (ITRS) helps guide the industry by projecting technology requirements for the next 15 years. It not only indicates possibly technology implementations at the various nodes but also gives the critical dimension requirements (Figure 1.3). This is all done in hope of keeping up with Moore's law and avoiding road blocks. Traditional 193 nm lithography is believed to be applicable down to the 45 nm node. Glancing at the roadmap one can see that 193 nm lithography ends at the 65 nm node and new technologies dubbed next generation lithography techniques will have to be utilized to reach the next technology nodes.

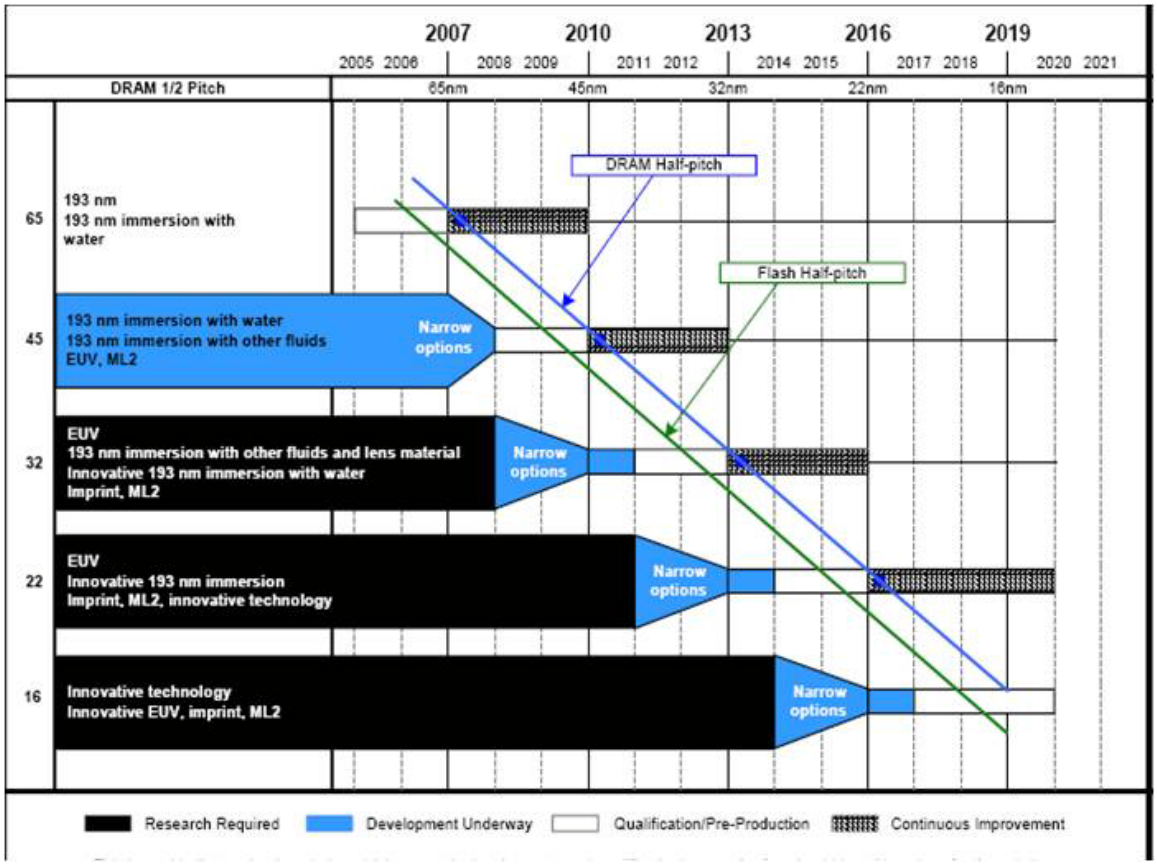

Figure 1.3. ITRS Roadmap a guide for the possible techniques to employ for the next technology nodes and their projected timeline to deployment.

1.2 Next Generation Lithography

1.2.1 Immersion Lithography

Immersion lithography, 193i, is similar to traditional photolithography with the exception that between the film to be imaged and the lens a liquid is present (Figure 1.4). This liquid, which is highly purified water for the first generation fluid, is used to enable an increase in the numerical aperture (NA) of the system as well as a higher depth of focus. The theoretical limit of feature size when employing highly purified water and using a 193 nm source is approximately 37 nm, see Equation 1.2.

$$R = \frac{k*\lambda}{NA} = \frac{k*\lambda}{n*sin\theta} \quad (1.2)$$

In Equation 1.2, k is the numerical constant of the tool/ process, λ is the wavelength of light used, n is the index of refraction of the medium between the lens and the film, and θ is the maximum half angle of light that reaches the film. Unfortunately, this means that immersion with water will not carry into the 22 nm node and may not even enable the 32 nm node without the use of additional techniques such as double patterning.

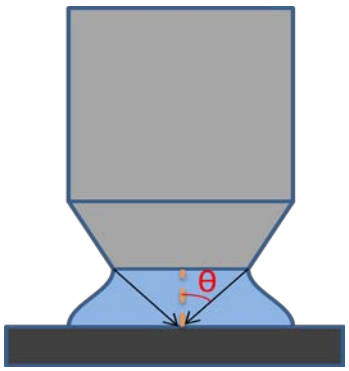

Figure 1.4. A cartoon of immersion lithography setup, with a fluid present between the wafer and lens.

The resists used in immersion lithography are traditional 193 nm resists, but a top coat is employed to prevent leaching of resist materials into the water, which would change the resist composition and thus the lithographic response and cause defects or foul the lens.[4] The transition to immersion was smooth since existing materials were compatible with the technique once the top coat was developed and fluid handling systems were developed. In order to extend 193i to the 21 nm node a technique called double patterning must be employed.

In double patterning the desired image is split between two masks and each is exposed sequentially (Figure 1.5). This increases the capital cost of the technique as well

as decreasing the throughput. Twice the number of lithography and etch steps are necessary to create the desired pattern.

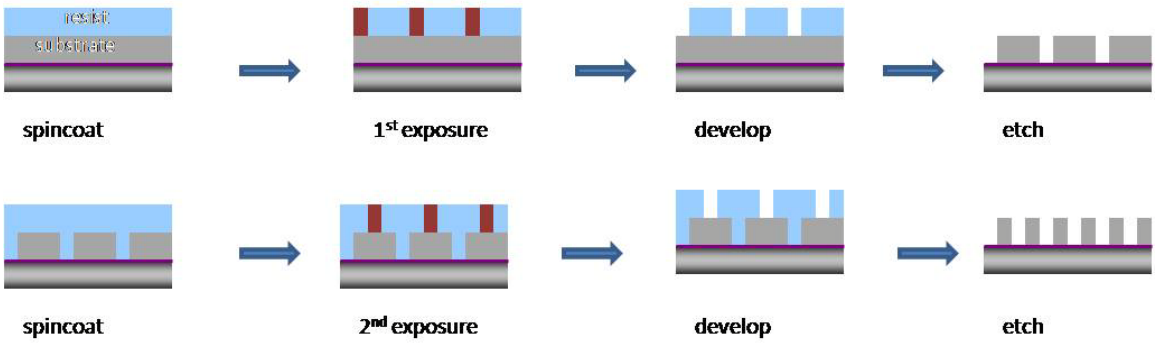

Figure 1.5. The double patterning process flow. The process requires two lithographic steps as well as two etch steps to create the desired pattern.

A second generation fluid with an index of refraction greater than 1.64 and absorption of less than 0.10/cm is being sought. Hydrocarbons such as decalin or cyclohexane are currently favored. The index of refraction of decalin is 1.65 at 193 nm and combined with a lens material with an index of refraction of 2 it is possible to achieve a NA of 1.55 which gives a theoretical limit of 32 nm features. By employing double patterning, the minimum feature size could be 25 nm. Second generation fluids till under development have problems with flammability, oxygen absorption, and photodegradation products that tend to be absorbing.[5-8] There are also problems with the fluids' high viscosity or surface tension that is too low, which will require tool changes and lower process throughput. There are also problems with the fluids interacting with the photoresist and fouling the lens.[9] There is a high probability that due to the many

changes necessary for the second generation of immersion lithography and the small processing gain it provides that this may not be the route to extend Moore's Law.[10]

1.2.2 Extreme Ultraviolet Lithography

Extreme Ultraviolet lithography or EUV is based on a mirror projection system that uses a 13.5 nm wavelength source. This system must be kept in ultra high vacuum since all matter absorbs EUV radiation. This also means special reflecting masks must be created as well as special optics. The special optics are created by layering materials such as molybdenum and silicon that reflect light by making use of interlayer interference. These layered materials must withstand the high powered photons, 92 eV for EUV light vs. 6.4 eV for 193 nm light, from the EUV source which are more powerful than those of all the previous sources. Each layer must also be virtually defect free.

One of the main problems with EUV is that to date there is no source that can run for a full production day. There are also issues with flare that lead to line edge roughness.[11] Contamination of the mask or mirrors from sources such as photoresist outgasing can ruin the process. Intel has already announced that EUV will not be used in the 22 nm node due to developmental delays.[12] There are also those who believe EUV will never make it to the production floor due to its high costs and low throughput, again it will not extend Moore's law.[13]

1.2.3 Imprint Lithography

Imprint lithography can be carried out by at least two separate methods. The first is a thermal route, which requires heating a polymer above its glass transition temperature so that it may flow and then imprinting the melted polymer with a patterned template. The second process, dubbed Step and Flash Imprint Lithography (SFIL) utilizes liquid

monomers that undergo a photochemical reaction and solidify when exposed to UV light through a transparent template which is typically fused silica. The resolution of the process has been demonstrated at the molecular scale at less than 4 nm resolution by utilizing carbon nanotubes as templates.[14]

Both processes rely on capillary flow to completely fill the template, but viscosity tends to be much higher in polymer melts leading to longer fill times. The features formed by thermal imprint are known to undergo thermal relaxation,[15] while this does not happen in SFIL materials. The heating in the thermal system can make alignment difficult due to the mismatches in the coefficient of thermal expansion and heating of the different layers and also causes additional stresses to the already patterned films; furthermore heating and cooling are slow processes. Using a multilevel template enables printing multiple levels at once, which enables both cost and processing savings.[16-18] In terms of capital costs, imprint machines are the least expensive of the next generation tools making SFIL an attractive alterantive.[19]

1.3 PATTERNING FOR OTHER INDUSTRIES

The costs associated with photolithography equipment are very high. A corollary to Moore's law called Rock's law[20] states the cost of microprocessor fabrication facilities double every four years. Thus, alternative methods of patterning are continuously sought, especially for industries that do not require the exacting precision of semiconductor manufacturing. One such technique recently demonstrated utilizes

electrohydrodynamic instabilities in liquid films to create both periodic microscale arrays of pillars and direct copies of patterned templates.[21] While this technique may not be ideal for semiconductor manufacturing due to the exacting pattern requirements, it is a low cost method that has other potential applications. These include micromechanical systems, microfluidic devices, magnetic data storage devices, and photonic bandgap materials.[22] Pillar arrays have already been shown to be excellent templates for the creation of highly porous membranes with nearly monodisperse pores on the micron scale.[23]

The creation of pillar arrays is a directed self assembly technique. Another self assembly technique that creates arrays of features utilizes block copolymers. Block copolymers are polymers in which there are chemically distinct monomers that are chemically bond to one another. These materials can be induced to minimize their interfacial area and form phase separated morphologies including spherical, cylindrical, gyroid, or lamellar phase depending upon the copolymer composition.[24] The size, shape and ordering of the features created by the morphologies or microdomains are dependent on the volume fraction of each block, the rigidity of the segments in the block, the strength of the interactions between the blocks, and the molecular weight.[24] When using block copolymers to create patterns on a substrate, the interaction between each block and the substrate is also important. Depending on the interaction, one block may segregate to the surface and/or to the substrate. One method to influence this arrangement is to apply external fields.

One approach that has successfully guided block copolymers to form the desired microdomains normal to the film surface is an applied electric field.[25-37] Another method to orient the microdomains is achieved by chemically modifying the surface of the substrate.[38, 39] Solvent evaporation can also induce order and orientation of block copolymer microdomains.[24]

All of these methods of orienting the microdomains of block copolymers are dependent on the quality of the block polymers. That is, block copolymers of narrow polydispersity are necessary for uniform microdomains. Recent advances in polymer synthesis including the discovery of living radical polymerization processes,[40, 41] like atom-transfer polymerization, have provided a path to narrow molecular weight distribution homopolymers as well as random and block copolymers at a low cost.

The success of block copolymers gave incentive to explore the ability to control the pillar array formation in photocurable thin films. This document details both material exploration and methods for controlling the ordering of pillars formed in photocurable thin films.

1.4 Research Presented

There are two main focuses in the research contained within this document. The first focus is the SFIL process and some of the earlier modeling work done within the Willson research group. The focus of the modeling moves from continuum models to a mesoscale model. The mesoscale model is introduced to capture the stochastic nature of the polymer chains. Unfortunately, the ability to simulate large features is too computationally intensive for this model alone and thus a multiscale model is presented.

The multiscale model is used to focus on a certain area interest rather than a bulk property. The multiscale model is presented as a possible method for studying template release in SFIL. The model consists of three components: the continuum model, the mesoscale code and the interface/gluing region.

The second focus of the research is on the creation of pillar arrays via electrohydrodynamic instabilities. The background is presented along with the work done to reproduce the initial findings in homopolyer films. The work then switches from using polymer thin films above their Tg to monomer solutions that are liquid at room temperature. These UV curable films reduce the processing time required for pillar experiments drastically. A variety of UV curable films are presented as well as improved experimental techniques. The research then shifts to trying to find methods to induce order in the created pillar arrays by utilizing patterned templates.

1.5 REFERENCES

1. Moore, G. E., Cramming more Components onto Integrated Circuits. *Electronics Magazine* **1965,** 19.

2. Thompson, L. F. W., C. G.; Bowden, M. J., *Introduction to Microlithography*. Second ed.; American Chemical Society: Washington, DC, 1994.

3. Trenkler, H. E. a. J., EUV lithography: technology for the semiconductor industry in 2010. *Europhysics News* **2004,** 35, (5).

4. Taylor, J. C. Advanced lithographic patterning technologies: materials and processes. University of Texas, Austin, 2007.

5. French, R. H.; Tran, H. V.; Adelman, D. J.; Rogado, N. S.; Kaku, M.; Mocella, M.; Chen, C. Y.; Hendrickx, E.; Van Roey, F.; Bernfeld, A. S.; Derryberry, R. A., High-index immersion fluids enabling cost-effective single-exposure lithography for 32 nm half pitches. *Proceedings of SPIE* **2008,** 6924, (Pt. 1, Optical Microlithography XXI), 692417/1-692417/8.

6. Furukawa, T.; Kishida, T.; Yasuda, K.; Shimokawa, T.; Liu, Z.; Slezak, M.; Hieda, K., High refractive index materials design for the next generation ArF immersion lithography. *Proceedings of SPIE* **2008,** 6924, (Pt. 1, Optical Microlithography XXI), 692412/1-692412/8.

7. Liberman, V.; Rothschild, M.; Palmacci, S. T.; Bristol, R.; Byers, J.; Turro, N. J.; Lei, X.; O'Connor, N.; Zimmerman, P. A., High-index immersion lithography: preventing lens photocontamination and identifying optical behavior of LuAG. *Proceedings of SPIE* **2008,** 6924, (Pt. 1, Optical Microlithography XXI), 692416/1-692416/11.

8. Sewell, H.; Mulkens, J.; Graeupner, P.; McCafferty, D.; Markoya, L.; Donders, S.; Cortie, R.; Meijers, R.; Evangelista, F.; Samarakone, N., High-n immersion lithography. *Proceedings of SPIE* **2008,** 6924, (Pt. 1, Optical Microlithography XXI), 692415/1-692415/12.

9. Tran, H. V. Evaluation of Next Generation Fluids for ArF Immersion Lithography Beyond Water. http://www2.dupont.com/Semi_Fabrication/en_US/assets/downloads/pdf/science/ArFImmersionpaper.pdf

10. Wilson, R. Immersion-lithography road map hits dead end. http://www.edn.com/index.asp?layout=article&articleid=CA6355060 (7/27/2008),

11. Chandhok, M.; Lee, S. H.; Bacuita, T., Effects of flare in extreme ultraviolet lithography: Learning from the engineering test stand. *Journal of Vacuum Science & Technology, B: Microelectronics and Nanometer Structures* **2004,** 22, (6), 2966-2969.

12. Lammers, D. Intel: 'EUV Facts Don't Add Up' for 22 nm in 2011. http://www.semiconductor.net/article/CA6553758.html

13. Mutschler, A. S. Why design engineers need to know about lithography. http://www.edn.com/article/CA6504364.html (7/27/2008),

14. Hua, F.; Sun, Y.; Gaur, A.; Meitl, M. A.; Bilhaut, L.; Rotkina, L.; Wang, J.; Geil, P.; Shim, M.; Rogers, J. A.; Shim, A., Polymer Imprint Lithography with Molecular-Scale Resolution. *Nano Letters* **2004,** 4, (12), 2467-2471.

15. Ding, Y.; Ro, H. W.; Germer, T. A.; Douglas, J. F.; Okerberg, B. C.; Karim, A.; Soles, C. L., Relaxation Behavior of Polymer Structures Fabricated by Nanoimprint Lithography. *ACS Nano* **2007,** 1, (2), 84-92.

16. Schmid, G. M.; Stewart, M. D.; Wetzel, J.; Palmieri, F.; Hao, J.; Nishimura, Y.; Jen, K.; Kim, E. K.; Resnick, D. J.; Liddle, J. A.; Willson, C. G., Implementation of an imprint damascene process for interconnect fabrication. *Journal of Vacuum Science & Technology, B: Microelectronics and Nanometer Structures--Processing, Measurement, and Phenomena* **2006,** 24, (3), 1283-1291.

17. Palmieri, F.; Stewart, M. D.; Wetzel, J.; Hao, J.; Nishimura, Y.; Jen, K.; Flannery, C.; Li, B.; Chao, H.-L.; Young, S.; Kim, W. C.; Ho, P. S.; Willson, C. G., Multi-level step and flash imprint lithography for direct patterning of dielectrics. *Proceedings of SPIE-The International Society for Optical Engineering* **2006,** 6151, (Pt. 1, Emerging Lithographic Technologies X), 61510J/1-61510J/9.

18. Stewart, M. D.; Wetzel, J. T.; Schmid, G. M.; Palmieri, F.; Thompson, E.; Kim, E. K.; Wang, D.; Sotodeh, K.; Jen, K.; Johnson, S. C.; Hao, J.; Dickey, M. D.; Nishimura, Y.; Laine, R. M.; Resnick, D. J.; Willson, C. G., Direct imprinting of dielectric materials for dual damascene processing. *Proceedings of SPIE-The International Society for Optical Engineering* **2005,** 5751, (Pt. 1, Emerging Lithographic Technologies IX), 210-218.

19. Sreenivasan, S. V.; Willson, C. G.; Schumaker, N. E.; Resnick, D. J. In *Cost of Ownership Analysis for Patterning Using Step and Flash Imprint Lithography*, Proc. SPIE 4688, 2002; 2002.

20. Kanellos, M. Soaring costs of chipmaking recast industry. http://news.cnet.com/Semi-survival/2009-1001_3-981418.html (11/21/2008),

21. Chou, S. Y.; Zhuang, L., Lithographically induced self-assembly of periodic polymer micropillar arrays. *Journal of Vacuum Science & Technology, B: Microelectronics and Nanometer Structures* **1999,** 17, (6), 3197-3202.

22. Pease, L. F.; Russel, W. B., Electrostatically induced submicron patterning of thin perfect and leaky dielectric films: A generalized linear stability analysis. *Journal of Chemical Physics* **2003,** 118, (8), 3790-3803.

23. Yan, X.; Liu, G.; Dickey, M.; Willson, C. G., Preparation of porous polymer membranes using nano- or micro-pillar arrays as templates. *Polymer* **2004,** 45, (25), 8469-8474.

24. Hawker, C. J.; Russell, T. P., Block copolymer lithography: Merging "bottom-up" with "top-down" processes. *MRS Bulletin* **2005,** 30, (12), 952-966.

25. Karim, A.; Berry, B. C.; Bosse, A.; Jones, R. L.; Douglas, J. F., Evolution of orientational order in directed assembly of block copolymer films. *Abstracts of Papers, 235th ACS National Meeting, New Orleans, LA, United States, April 6-10, 2008* **2008**, POLY-562.

26. Yang, J.; Sekine, R.; Aoki, H.; Ito, S., Localization and Orientation of Homopolymer in Block Copolymer Lamella: A Near-Field Optical Microscopy Study. *Macromolecules* **2007,** 40, (21), 7573-7580.

27. Mita, K.; Tanaka, H.; Saijo, K.; Takenaka, M.; Hashimoto, T., Cylindrical Domains of Block Copolymers Developed via Ordering under Moving Temperature Gradient. *Macromolecules* **2007,** 40, (16), 5923-5933.

28. Tsori, Y., Lamellar Phases in Nonuniform Electric Fields: Breaking the In-Plane Rotation Symmetry and the Role of Dielectric Constant Mismatch. *Macromolecules* **2007,** 40, (5), 1698-1702.

29. Olszowka, V.; Hund, M.; Kuntermann, V.; Scherdel, S.; Tsarkova, L.; Boeker, A.; Krausch, G., Large scale alignment of a lamellar block copolymer thin film via electric fields: a time-resolved SFM study. *Soft Matter* **2006,** 2, (12), 1089-1094.

30. Boeker, A.; Schmidt, K.; Knoll, A.; Zettl, H.; Haensel, H.; Urban, V.; Abetz, V.; Krausch, G., The influence of incompatibility and dielectric contrast on the electric field-induced orientation of lamellar block copolymers. *Polymer* **2006,** 47, (3), 849-857.

31. Schmidt, K.; Boeker, A.; Zettl, H.; Schubert, F.; Haensel, H.; Fischer, F.; Weiss, T. M.; Abetz, V.; Zvelindovsky, A. V.; Sevink, G. J. A.; Krausch, G., Influence of Initial Order on the Microscopic Mechanism of Electric Field Induced Alignment of Block Copolymer Microdomains. *Langmuir* **2005,** 21, (25), 11974-11980.

32. Xiang, H.; Lin, Y.; Russell, T. P., Electrically Induced Patterning in Block Copolymer Films. *Macromolecules* **2004,** 37, (14), 5358-5363.

33. DeRouchey, J.; Thurn-Albrecht, T.; Russell, T. P.; Kolb, R., Block Copolymer Domain Reorientation in an Electric Field: An in-Situ Small-Angle X-ray Scattering Study. *Macromolecules* **2004,** 37, (7), 2538-2543.

34. Boeker, A.; Elbs, H.; Haensel, H.; Knoll, A.; Ludwigs, S.; Zettl, H.; Zvelindovsky, A. V.; Sevink, G. J. A.; Urban, V.; Abetz, V.; Mueller, A. H. E.; Krausch, G., Electric field induced alignment of concentrated block copolymer solutions. *Macromolecules* **2003,** 36, (21), 8078-8087.

35. Xu, T.; Hawker, C. J.; Russell, T. P., Interfacial Energy Effects on the Electric Field Alignment of Symmetric Diblock Copolymers. *Macromolecules* **2003,** 36, (16), 6178-6182.

36. Tsori, Y.; Tournilhac, F.; Leibler, L., Orienting Ion-Containing Block Copolymers Using Ac Electric Fields. *Macromolecules* **2003,** 36, (15), 5873-5877.

37. Elhadj, S.; Woody, J. W.; Niu, V. S.; Saraf, R. F., Orientation of self-assembled block copolymer cylinders perpendicular to electric field in mesoscale film. *Applied Physics Letters* **2003,** 82, (6), 871-873.

38. Huang, E.; Russell, T. P.; Harrison, C.; Chaikin, P. M.; Register, R. A.; Hawker, C. J.; Mays, J., Using Surface Active Random Copolymers To Control the Domain Orientation in Diblock Copolymer Thin Films. *Macromolecules* **1998,** 31, (22), 7641-7650.

39. Mansky, P.; Liu, Y.; Huang, E.; Russell, T. P.; Hawker, C., Controlling polymer-surface interactions with random copolymer brushes. *Science* **1997,** 275, (5305), 1458-1460.

40. Braunecker, W. A.; Matyjaszewski, K., Controlled/living radical polymerization: Features, developments, and perspectives. [Erratum to document cited in CA147:486671]. *Progress in Polymer Science* **2008,** 33, (1), 165.

41. Matyjaszewski, K.; Spanswick, J., Controlled/living radical polymerization. *Plastics Engineering* **2005,** 70, (Handbook of Polymer Synthesis (2nd Edition)), 895-941.

Chapter 2

This chapter introduces the SFIL process. It explains some of the process savings gained by the ability to create 3D features in one step. The focus then moves on to some early work on modeling the densification of the SFIL etch barrier material after curing using continuum models. The modeling then moves to discuss a finer mesoscale model that was developed to study the stochastic nature of the polymerization.

2.1 Step and Flash Imprint Lithography

Step and Flash Imprint Lithography (SFIL) is a process developed at The University of Texas at Austin[1], is a next generation lithographic technology that can pattern substrates using a photopolymerizable liquid to replicate a template's relief features. The process used to pattern a substrate involves five general steps (Figure 2.1). First, the etch barrier, a photopolymerizable silicon containing mixture, is dispensed upon the transfer layer or straight onto the substrate. A patterned quartz template brought in contact with the etch barrier liquid. Upon UV exposure through the template, the etch barrier polymerizes and crosslinks, becoming a solid replica of the template pattern. The template is then separated from the replicated pattern. Two etch steps follow, to transfer the pattern through to the substrate.

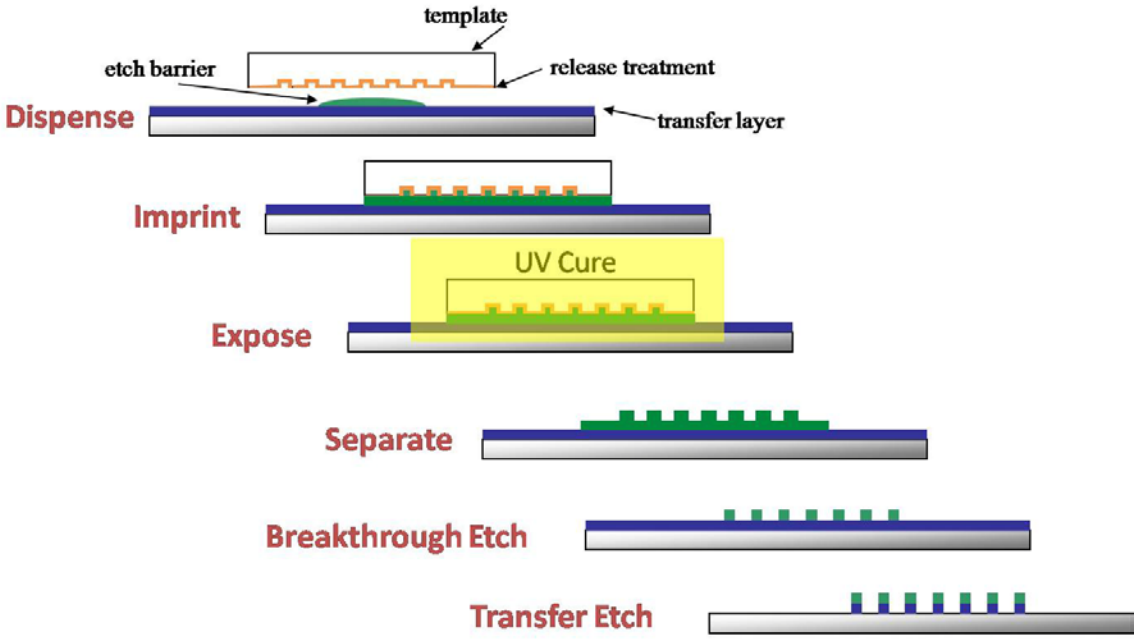

Figure 2.1. The SFIL process: dispense the etch barrier, imprint the features, expose the etch barrier through the template, separate, and etch the pattern into the underlying layers.

Tools are commercially available based on the SFIL process through Molecular Imprints. These production tools are marketed for the 32-16 nm node, and are capable of multiple layer alignment. The dispense step is carried out using inkjet technology that dispense drops in the pico-liter range. This technology, dubbed Drop-on-Demand™, allows for the simultaneous patterning of both dense and isolated features by controlling the drop pattern of the dispensed etch barrier. The templates are patterned through the existing lithographic mask making infrastructure. The imprint machines are capable of patterning substrates of different sizes as well as patterning both sides of the substrate for applications like hard disk drives.

2.2 PROCESS SAVINGS USING SFIL'S 3-D REPLICATION

The ability to create 3-D features with SFIL gives it an advantage over traditional lithography. One process in particular where SFIL could reduce the number of process steps is the dual damascene process. The dual damascene process creates the vias and wires that connect the various levels of the device to one another and to the outside world. The method, as pictured in Figure 2.2, consists of about thirteen separate unit processes which involve moving the substrates between tools.

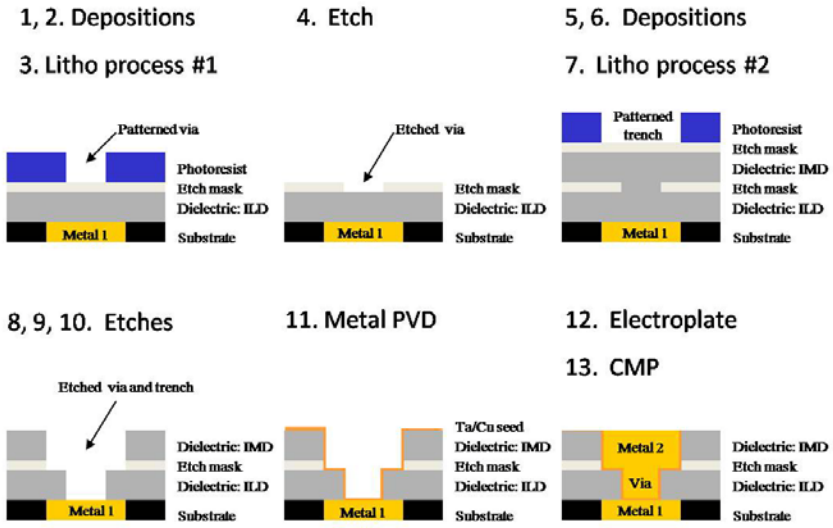

Figure 2.2. Dual Damascene Process is used to create the via connection between wires in different layers of the device.[2] The first two unit processes are deposition steps of the dielectric followed by the etch mask. The next unit process is the lithographic process to create the patterned via. This lithographic process involves coating a photoresist over the etch match and then exposing the photoresist film to UV light through a mask to create the via. The film is then developed to yield the picture in the top left. The image is then etched into the etch mask and the residual photoresist is removed. Another layer of dielectric and an etch mask are again deposited. The lithographic step is repeated but with another mask to create the trench. Next the trench created in the top right step is transferred via and etch step into the etch mask and then into the dielectric and finally into the metal 1 layer. A seed layer is then deposited to stop metal 2 from diffusing. Metal 2 is then electroplated into the trench and the via. The excess metal 2 is removed by chemical mechanical polishing.

The dual damascene process carried out using SFIL saves a number of processing steps and provides cost saving. There are two methods of carrying out the creation of the via chains, they both require 3-D templates. The first dubbed the sacrificial imprint process consists of five unit processes; see the left side of Figure 2.3. The other process utilizes a photocurable dielectric material that becomes part of the device, hence called the directly patternable dielectrics process, see right side Figure 2.3. This process saves at least one additional etch step.

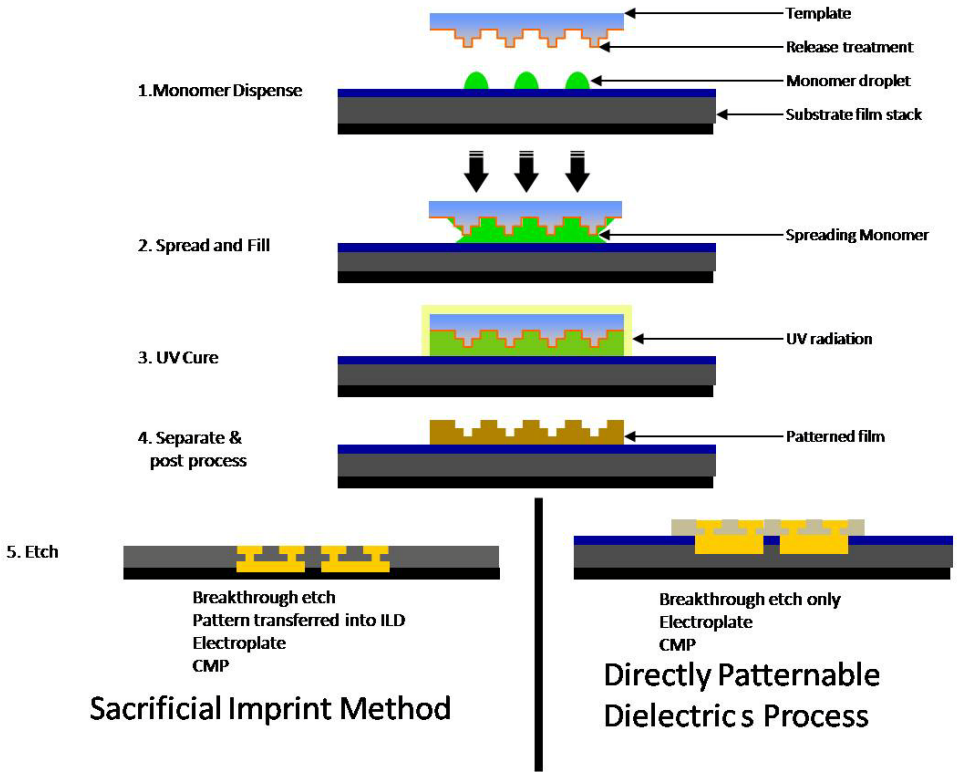

Figure 2.3. Two methods for the dual damascene process can be carried out using SFIL technology.[2] Left: the sacrificial method where the imprinted material acts as an etch mask to transfer the pattern into the underlying layer. Right: The directly patternable dielectric process the imprinted material becomes part of the device.

2.3 NEED FOR SFIL SIMULATION PACKAGE

In the semiconductor industry time is money and in order to adopt changes the industry typically relies on process simulation tools such as KLA-Tencor's PROLITH and SIGMA-C's SOLID-C rather than interrupting the production line for tests or investing in a designated research tool. These simulation tools aid in the design of masks, exposure source selection, resist selection and even etch processing. If SFIL is to be adopted, the semiconductor industry will require a similar simulation package that could act as a guide for template design and material selection. This simulation could also be used to test new materials and work on minimizing the force required to release the etch barrier from the template.

2.4 SFIL CONCLUSIONS

SFIL is a low cost next generation lithography technique. SFIL's high resolution and ability to create 3D features in one step give it a significant advantage over traditional lithography techniques. SFIL could benefit from the creation of a simulation package that would allow for material testing as well as studying of the release of the imprinted material from the template. This document will describe an initial approach to an SFIL simulation package.

2.5 MODELING THE SFIL PROCESS: CAPTURING VOLUME CHANGE

During the exposure step, polymerization causes densification within the patterned feature. This densification is a result of the transition from liquid to a solid, i.e. from van der Waals interactions to covalent bonds. The standard etch barrier formulation consists of several monomers, one containing silicon to provide etch resistance, another

that is a reactive diluent to keep the viscosity low, a crosslinker, and a photoinitiator. The crosslinker is necessary to provide mechanical stability to the cured features. The amount of the crosslinker component in the formulation directly affects both the mechanical properties of the feature as well as the amount of shrinkage that occurs, since a crosslinker can create multiple covalent bonds.

Semiconductor manufacturing requires a highly repeatable and accurate printing process in order to create devices. The placement of the printed features and their shape must be controlled with nanometer accuracy. This precision is required for the alignment of subsequent layers of patterns to create devices. Thus, it is necessary to gauge the effect of the shrinkage on both the resultant features as well as on pattern placement.

Colburn[3] and Johnson[4] used finite element/continuum models to study the effect of the polymer densification on the features' height, side wall angle, and width. This was done by performing SFIL experiments with various formulations and once completed cross-sectioning the template and using a scanning electron microscope to measure the templates' feature dimensions, and comparing them to the SFIL imprints. It was found that the majority of the shrinkage was in the vertical direction (Figure 2.4) and dependant on the feature geometry. Material selection was also found to affect the overall shrinkage, with long pendant groups on the monomers decreasing the shrinkage and larger amounts of crosslinker increasing it. With this information in hand, work was carried out to create a predictive model.

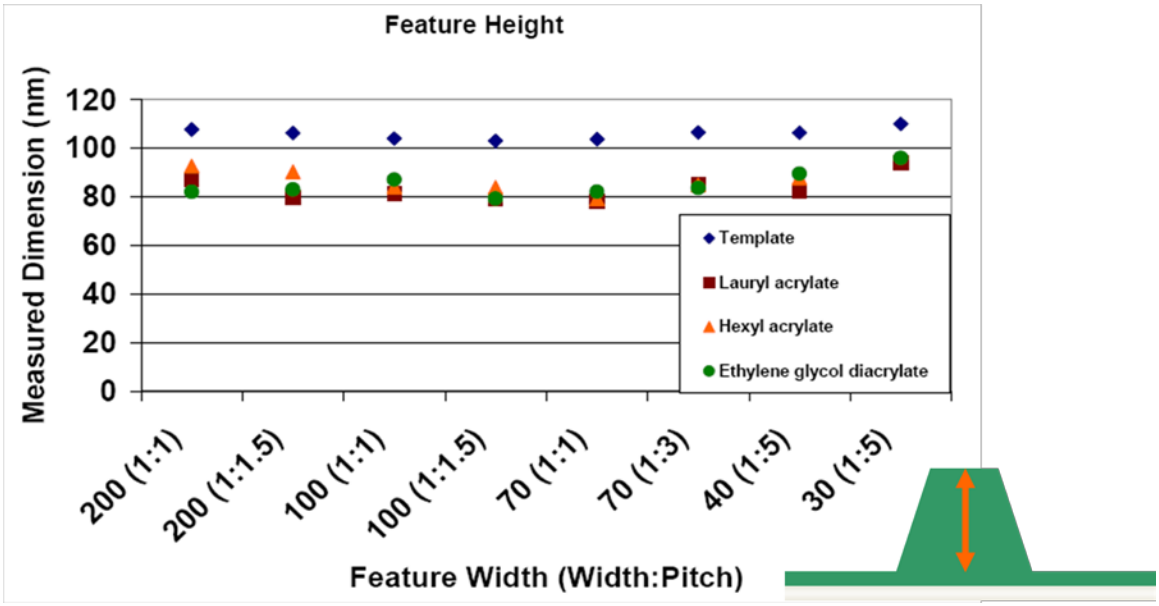

Figure 2.4. The results of various S-FIL imprint experiments with features of different spacing and geometry done with different materials, comparing the height of the template with the imprinted feature heights.[4]

2.6 Initial SFIL Models

In order to aide in the design of templates, a finite element, FE, model was created in Pro/E®. Both Colburn and Johnson used an isotropic densification to simulate the worst case scenario. The model only predicted the feature shape after template removal and did not take into account any template interactions. The adjustable parameters were the coefficient of thermal expansion (CTE), the Poisson's ratio, and Young's modulus. With this model, the pattern layout was tested to determine the final pattern displacement as result of pattern proximity. The effects of the etch barrier formulation on the feature shape were also determined. The FE model gave confidence that in the worst case scenario displacements are minimal for the structures studied as seen in Figure 2.5.

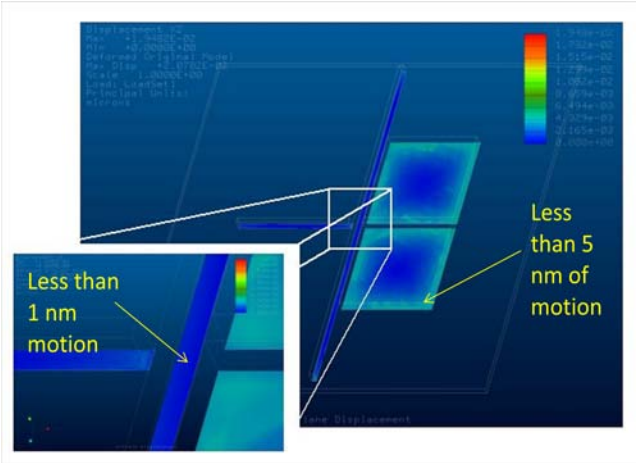

Figure 2.5. Finite Element model of the SFIL process which predicted the movement of the thin line near large patterned features as upon curing is nominal.[5]

At dimensions on the order of 40 nm, it has been shown that material properties in nanoscopic features vary from that of the bulk.[6-11] This is due in part to the stochastic nature of the polymer chains. By using an FE approach, this stochastic nature is lost and thus it is impossible to take into account variations in material properties. A stochastic model was chosen to aide in determining the mechanical properties based on the etch barrier formulation as well as to test for possible defects in the created features.

2.7 Mesoscale Model: Capturing Volume Change and Stochasticity

The mesoscale model is based on the interactions of the components of the etch barrier formulation. It is a model in which each chemical entity is represented by a bead and the interactions are all represented by springs. In the first model developed by Ryan Burns, the etch barrier components were populated as points on a lattice with template molecules as the outer most layer.[12] The model focuses on the polymerization of the etch

barrier. A Monte Carlo method was used to simulate the reaction kinetics. The kinetics follow a standard free radical scheme, with initiation, propagation and termination reactions all governed by probabilities. The use of voids on the lattice allowed for the diffusion of non-bonded molecules on the lattice. The guide for the reactions kinetics was real-time infrared spectroscopy measurements.[13]

Once the connectivity of the polymer molecules was established, the stress, τ, between the molecules was then calculated. This was done using a quadratic potential function (Equation 2.1). The input to the potential was the distance between neighbors, r, and a spring constant to denote the bond strength, k. Covalent bonds were modeled using a large spring constant. The van der Waals force between non-bonded molecules was modeled by a small spring constant. The distance between covalently bonded molecules was less than that for the nonbonded molecules. The interaction with the template was given its own spring constant and distance. The equilibrium distance between molecules was denoted by r_{eq}.

$$\tau = k\left(r - r_{eq}\right)^2 \qquad (2.1)$$

To solve for the end feature geometry based on the stress between molecules the matrix of simultaneous equations:

$$[A][x] = [B] \qquad (2.2)$$

was solved. Where A is the stiffness matrix, B is the load matrix and x is the displacement matrix. The interaction of every molecule with its six neighbors located on the main axes is resolved into its x, y, and z vector components The displacement matrix

was then solved using a Gauss-Siedel routine for each row of vectors, in each direction, until the solution converged to a chosen tolerance.

The Gauss-Siedel approach to the displacement solution is very slow. The iterative solution for a 25 nm^3 feature took over thirty minutes with a tolerance of 0.1 angstrom. This would certainly not facilitate the modeling of an entire 65 x 65 mm template, so a new approach was necessary.

2.7.1 CURRENT MESOSCALE MODEL

The model is based upon a standard acrylate SFIL etch barrier formulation. The formulation consists of: a free radical initiator, Darcur 1173, a reactive diluent, t-buytl acrylate (tBA), a silicon containing monomer for etch resistance, Gelest SIA-0210 (SIA), and a crosslinker, ethylene glycol diacrylate (EGDA) (Table 2.1). The first step in the simulation is to randomly populate the lattice with the formulation's constituents based upon the input ratios along and ten percent voids to allow some movement on the lattice.

Component	Purpose	Weight %
Gelest SIA-0210	Provides etch resistance	44
Ethylene Glycol Diacrylate	Provides mechanical strength through crosslinking	15
t-Butyl Acrylate	Reactive diluent	37
Darocur 1173	Photoinitiator	1-4

Table 2.1. Components of the Monomat SFIL etch barrier formulation.

An initial exposure step is simulated by randomly reacting a small number of initiators. Although the initiator may form two radicals upon decomposition, only one radical is simulated. The success of the reaction is determined through probability based upon reaction kinetics. The reaction proceeds through free radical mechanism and the conservation of species yields Equations 2.3-2.5. It was through the study of the polymerization with real time infrared spectroscopy that reaction rate coefficients: k_I, k_p, and k_t were determined.[14] With the reaction rate coefficients in hand, the Arrhenius law, Equation 2.6, can be used to get the activation energy, E_a. The probability of the reaction success is then found through Equation 2.7, once a site has been randomly chosen a trial reaction is attempted.

Initiator: $$\frac{d[I]}{dt} = -\Phi' k_I [I] \quad (2.3)$$

Radicals: $$\frac{d[R]}{dt} = 2\Phi k_I [I] - k_{O2} [O_2][R] - 2k_t [R]^2 \quad (2.4)$$

Monomer: $$\frac{d[M]}{dt} = -k_p [M][R] \quad (2.5)$$

Arrhenius law: $$k_i(T) = A \exp\left(\frac{-E_a}{k_B T}\right) \quad (2.6)$$

Probability: $$P \propto \exp\left(-\frac{E_a}{k_B T}\right) \quad (2.7)$$

Initial exposure is simulated by looping from the top of the feature and trying initiation reaction with the initiator species present to create radicals. Once the desired amount of radicals, typically 4%, is created the propagation loop begins. In this loop, sites are selected at random and based upon the identity of the species four things may happen:

Void: If the species is a void no moves are attempted.

Radical: If the species is a radical, a neighbor is chosen and a trial reaction is then carried out. If the neighbor in the reaction is a monomer capable of bonding, a trial reaction is attempted. If the reaction is accepted then the radical identity is passed to the neighbor and the polymer identity is assigned to the former radical species. If the neighbor is another radical, then a termination reaction is attempted and if successful the radical identity is removed from both and they are instead labeled polymer.

Monomer: If the species is a monomer, the monomer will randomly choose a neighbor and if that neighbor is a void it will change position with it every time. This is done to allow movement on the lattice, since bonding is restricted to the major axes.

Initiator: If the species is an initiator, an initiation reaction is attempted and if successful the initiator is given the radical identity.

Throughout this process the number of bonds to each species is tracked and the bond direction is stored. Initiators with the identity radical can only bond to one species. Monomers may bind to two species. Crosslinkers may bind to four species. The bonding only occurs on the six major lattice axes with the diagonal interaction taken into account in the nonbonding potential.

The polymerization routine was changed to speed up the time required to reach a desired conversion by looping through a small number of randomly chosen chain ends when the conversion stalls. The criteria for stopping the polymerization loop were changed to reflect a desired overall conversion to polymer instead of just iterations. A chain statistic routine was added to track the average degree of polymerization as well as the minimum, maximum and standard deviation of the chains. An analysis routine was added to track failures in the resulting polymer network in the way of non-bonded materials or clumps of voids in columns and planes. It was also found that the intial model developed by Ryan Burns did not capture shear since it only considered the six major axes neighbors the current version. The current model considers interaction with the eighteen nearest neighbors.

2.7.2 Mesoscale Failure Analysis Results

The motivation for the failure analysis is that as the features get smaller they will approach the size of tens of monomers. The question then is, are there areas in a created feature where an open could occur due to voids or non-bonded material in long lines. The results from this work show that using the standard SFIL formulation with 10% voids added for lattice movement there are very few full xy planes of failure until there are less than 5 monomers in one dimension in the feature.

The results (Table 2.2) show that for lines of length of 5.9 microns there is a dependence on the width of the feature as to the number of defects. This is due to the fact that the monomer molecules are more likely to become confined and not encounter radicals in order to form polymer.

Dimension WxHxL (XxYxZ)	Average dead columns/micron (length)	Average Shorted Planes/micron (length)	Number of Simulations
4x10x10000	3.94	0	100
3x10x10000	5.39	0.08	88

Table 2.2. Failure analysis results for very thin lines.

Shorts and whole plane failures do not occur often under normal formulation concentrations but other errors can occur that cause the feature to fail. A major contributing to defectivity in SFIL is particle contamination. Although imprint templates have been shown to be self cleaning upon successive imprints[15], any device failure detracts from the appeal of using SFIL. To study particle contamination by uncured material, the failure analysis routine was changed to check for non-bonded material in the

outer most layer of the feature, which is in contact with the template. While it is not certain that all non-bonded materials will stick to the template or that just those on the outer most layer of the feature will, it was thought that using the outer most layer would capture the phenomenon as a worst case scenario.

Two simulations were run with the standard etch barrier formulation with 10% voids added to allow diffusion the results are shown in Table 2.3. For a 50x50x50 monomer cube, after 193 realizations showed no dead columns or planes and on average 8.6 possible edge defect particles. For a 50x50x1000 monomer case, after 65 realizations there were no dead columns or planes and an average of 17.1 possible edge defects were found.

Size WxHxL (XxYxZ)	Minimum edge defect/nm (length)	Maximum edge defect/nm (length)	Average Number edge defect/nm (length)	Realizations
50x50x50	0.034	0.508	0.292	193
50x50x1000	0.014	0.042	0.029	65

Table 2.3. Results from the edge defect simulations as a worst case scenerio.

2.7.3 Mesoscale Failure Analysis Discussion

There appears to be a small possibility of shorts and opens in the current features sought which are tens of microns in the smallest dimension. The one possible flaw in the anaylsis is that if the polymer is all in one plane it may be missed by the full plane short analysis, since the criteria for flagging an error is the absence of covalent bonds. This can be adjusted by checking the directions of the bonding.

As for the edge defects, this appears to be a high number of defects possible and does not match experimental evidence. The simulation does not take into account whether the particles actually get pulled from the feature and stick to the template and this may account for most of the discrepancy. This interaction would be an excellent addition to the simulation. Also this would inspire changing formulations to improve performance.

2.7.3 Mesoscale Parameter Estimation

With the hope of a faster and more physically accurate solution, work was done to determine better representations of the model parameters. The spring constants were given a more physical basis by use of bond energy and other published interaction data. An error was found in the initial model, due to the fact that only the six main neighbors are considered. By ignoring the diagonal neighbor interactions, the shear behavior of the material was lost. Thus the model now considers the interaction between eighteen neighbors.

Further improvement to the lattice spacing and equilibrium molecule distance was found using Sparta® to find the van der Waals volumes of the etch barrier components. In order to more accurately portray the van der Waals bonds, the potential was changed to the Lennard-Jones potential function. The Lennard-Jones parameters, σ and ε, were calculated based on the relationship in Equations 2.8 and 2.9, which were devised by regressing both experimental and second viral coefficient data to find a best fit.[16] The

acentric factor ω, and the critical properties are calculated through group contribution theory.[17, 18]

$$\varepsilon = k(0.7915 + 0.1693\omega)T_{cr} \tag{2.8}$$

$$\sigma = \left(\frac{P_{cr}}{T_{cr}}\right)^{\frac{-1}{3}}(2.3551 - 0.0874\omega) \tag{2.9}$$

From the Lennard-Jones parameters, it is possible to calculate and effective spring constant using Equation 2.10 to offer a comparsion.[19]

$$k_{eff} = \frac{36(2^{2/3})\varepsilon}{\sigma^2} \tag{2.10}$$

Component	σ (Å)	ε (J)	k_{eff} (J/ Å^2)
Gelest SIA	8.78	9.30x10^{-5}	6.89x10^{-5}
EGDA	6.71	7.79x10^{-5}	9.88x10^{-5}
tBA	6.31	6.80x10^{-5}	9.77x10^{-5}
Darocur 1173	6.84	1.00x10^{-4}	1.23x10^{-4}
Methyl methacrylate	5.90	6.44x10^{-5}	1.06x10^{-4}

Table 2.4. Lennard-Jones parameters and their resultant effective spring constants dervived from Equations 2.8-2.10 for the etch barrier components and methy methacrylate.

2.8 ENERGY MINIMIZATION: SHRINKAGE CALCULATION

In order to improve the solution time and increase the ability to simulate larger areas, collaboration was begun with researchers at the Institute for the Computational Engineering and Sciences (ICES) at UT. The model was split into two parts, the polymerization code and the solver which the ICES group took charge of. Both linear and nonlinear solvers have been formulated. The most recent version of the solver uses an algorithm that employs two software packages: PETSc[20] and TAO.[21] The algorithm follows an inexact Newton trust-region method and is described here.[22]

The collaboration led to the conclusion that in order to simulate and entire template, a multiscale model is required due to the fact that a square lattice with a 14.7 nm size requires over a day of calculation time and one gigabyte of memory to solve.

2.8.1 Solver Model Improvements

In order to study the effect of other potential models, the solver was adapted to run for two other potential systems. The first dubbed the mix potential system utilizes the harmonic potential for the bonded monomer interaction and for the non-bonded interactions it utilizes the Lennard-Jones 6-12 potential. The second potential model is the finitely extensible nonlinear elastic (FENE) potential which again uses the Lennard-Jones 6-12 potential for the non-bonded interactions but uses a different attractive potential for the bonded interactions. More information on these potentials is discussed in section 3.2.1.2.

2.9 CONCLUSION

SFIL is a low cost next generation technology with the ability to directly pattern 3D features. With the feature sizes decreasing to the limit where it is believed that bulk properties no longer apply and thus continuum models fail, a stochastic model was developed. This stochastic model was used to study two possible defects in the patterned features, shorts and edge particle defects. The simulations showed that shorts do not become common until smallest feature size is below 3 nm. Edge defects are more prevalent and the model should add template interaction to see if in fact the defects stick to the template every time. The stochastic model is much more computationally intensive than the continuum model and was not feasible to utilize to simulate large features even with help from the ICES collaboration. In order to be able to simulate larger problems it is necessary to find some balance between the rigor of the mesoscale model and the speed of the continuum model. Thus, a multiscale scale model is proposed as the solution to tackle simulation of larger scale features.

2.10 REFERENCES

1. Colburn, M. Step and flash imprint lithography: a low-pressure, room-temperature nanoimprint lithography. University of Texas, Austin, 2001.

2. Palmieri, F. Step and Flash Imprint Lithography: Materials and Applications for the Manufacture of Advanced Integrated Circuits. University of Texas, Austin, 2008.

3. Colburn, M.; Johnson, S.; Stewart, M.; Damle, S.; Bailey, T. C.; Choi, B.; Wedlake, M.; Michaelson, T.; Sreenivasan, S. V.; Ekerdt, J.; Willson, C. G., Step and flash imprint lithography: a new approach to high-resolution patterning. *Proceedings of SPIE-The International Society for Optical Engineering* **1999,** 3676, (Pt. 1, Emerging Lithographic Technologies III), 379-389.

4. Johnson, S. C. Step and flash imprint lithography materials and process development. University of Texas, Austin, 2005.

5. Johnson, S.; Burns, R.; Kim, E. K.; Schmid, G.; Dickey, M.; Meiring, J.; Burns, S.; Stacey, N.; Willson, C. G.; Convey, D.; Wei, Y.; Fejes, P.; Gehoski, K.; Mancini, D.; Nordquist, K.; Dauksher, W. J.; Resnick, D. J., Step and flash imprint lithography modeling and process development. *Journal of Photopolymer Science and Technology* **2004,** 17, (3), 417-420.

6. Bohme, T. R.; de Pablo, J. J., Evidence for size-dependent mechanical properties from simulations of nanoscopic polymeric structures. *Journal of Chemical Physics* **2002,** 116, (22), 9939-9951.

7. Stoykovich, M. P.; Yoshimoto, K.; Nealey, P. F., Mechanical properties of polymer nanostructures: measurements based on deformation in response to capillary forces. *Applied Physics A: Materials Science & Processing* **2008,** 90, (2), 277-283.

8. Cheng, W.; Sainidou, R.; Burgardt, P.; Stefanou, N.; Kiyanova, A.; Efremov, M.; Fytas, G.; Nealey, P. F., Elastic Properties and Glass Transition of Supported Polymer Thin Films. *Macromolecules* **2007,** 40, (20), 7283-7290.

9. Yoshimoto, K.; Jain, T. S.; Van Workum, K.; Nealey, P. F.; De Pablo, J. J., Mechanical Heterogeneities in Model Polymer Glasses at Small Length Scales. *Physical Review Letters* **2004,** 93, (17), 175501/1-175501/4.

10. Fryer, D. S.; Nealey, P. F.; de Pablo, J. J., Scaling of Tg and reaction rate with film thickness in photoresist: A thermal probe study. *Journal of Vacuum Science & Technology, B: Microelectronics and Nanometer Structures* **2000,** 18, (6), 3376-3380.

11. Torres, J. A.; Nealey, P. F.; de Pablo, J. J., Molecular Simulation of Ultrathin Polymeric Films near the Glass Transition. *Physical Review Letters* **2000,** 85, (15), 3221-3224.

12. Burns, R. L.; Johnson, S. C.; Schmid, G. M.; Kim, E. K.; Dickey, M. D.; Meiring, J.; Burns, S. D.; Stacey, N. A.; Willson, C. G.; Convey, D.; Wei, Y.; Fejes, P.; Gehoski, K. A.; Mancini, D. P.; Nordquist, K. J.; Dauksher, W. J.; Resnick, D. J., Mesoscale modeling for SFIL simulating polymerization kinetics and densification. *Proceedings of SPIE-The International Society for Optical Engineering* **2004,** 5374, (Pt. 1, Emerging Lithographic Technologies VIII), 348-360.

13. Dickey, M. D.; Burns, R. L.; Kim, E. K.; Johnson, S. C.; Stacey, N. A.; Willson, C. G., Study of the kinetics of Step and Flash imprint lithography photopolymerization. *AIChE Journal* **2005,** 51, (9), 2547-2555.

14. Dickey, M. D.; Willson, C. G., Kinetic parameters for step and flash imprint lithography photopolymerization. *AIChE Journal* **2006,** 52, (2), 777-784.

15. Bailey, T.; Choi, B. J.; Colburn, M.; Meissl, M.; Shaya, S.; Ekerdt, J. G.; Sreenivasan, S. V.; Willson, C. G., Step and flash imprint lithography: Template surface treatment and defect analysis. *Journal of Vacuum Science & Technology, B: Microelectronics and Nanometer Structures* **2000,** 18, (6), 3572-3577.

16. Reid, R. C. P., J.M.;Sherwood, T.K., *The Properties of Gases and Liquids*. McGrawHill: 1977.

17. Constantinou, L.; Gani, R.; O'Connell, J. P., Estimation of the acentric factor and the liquid molar volume at 298 K using a new group contribution method. *Fluid Phase Equilibria* **1995,** 103, (1), 11-22.

18. Marrero, J.; Gani, R., Group-contribution based estimation of pure component properties. *Fluid Phase Equilibria* **2001,** 183-184, 183-208.

19. Retkute, R.; Gleeson, J. P., Dynamics of two coupled particles: comparison of Lennard-Jones and spring forces. *Proceedings of SPIE-The International Society for*

Optical Engineering **2005,** 5845, (Noise in Complex Systems and Stochastic Dynamics III), 61-71.

20. Balay, S.; Buschelman, K.; Gropp, W. D.; Kaushik, D.; Knepley, M. G.; McInnes, L. C.; Smith, B. F.; Zhang, H. PETSc Web page. http://www.mcs.anl.gov/petsc

21. S. Benson, L. C. M., J. Morre, T. Munson, and J. Sarich TAO user manual (revision 1.9). http://www.mcs.anl.gov/tao

22. Bauman, P. T. Adaptive Multiscale Modeling of Polymeric Materials Using Goal-Oriented Error Estimation, Arlequin Coupling, and Goals Algorithms. University of Texas, Austin, 2008.

Chapter 3

This chapter introduces the concept of multiscale modeling. The multiscale model consists of three components: the continuum model, the mesoscale model, and the interface model which couples the two models. Each model is introduced and the calibration of the models is discussed.

3.1 MULISCALE MODELING

Multiscale modeling focuses on the marriage of models with phenomena on different scales of both time and length. It began with upscaling methods where models were combined by first solving the fine scale model and then passing the information to a coarser model, like a continuum model. The coupling for such a model is said to be one way with the information going from the finer scale to the coarser scale model. This upscaling method is employed whenever first principles are used to predict macroscopic behavior. An example of this is using a fine scale model like ab initio methods to parameterize reaction rate coefficients. From there, a broad selection of methods has been developed that are defined by the scale of the phenomena that they cover. Hybrid models can be used when there are large differences in the scales between phenomenons. Coarse graining or multigrid–type methods can be used when there is no separation of scales. A review of the different models is available here.[1]

For the SFIL simulation, the two models involved are the mesoscale code which is to be joined to a continuum code. The idea being that in the area of interest, the finer

model is used and in less critical areas the continuum is used. In this manner, the benefit of speed of the continuum model is possible along with the accuracy of the mesoscale model in the area of interest. It is not a direct mapping of one code to the other instead, between the two codes an interface region is used to accurately map the energy effects to match the differing scales of the models, as seen in Figure 3.1.

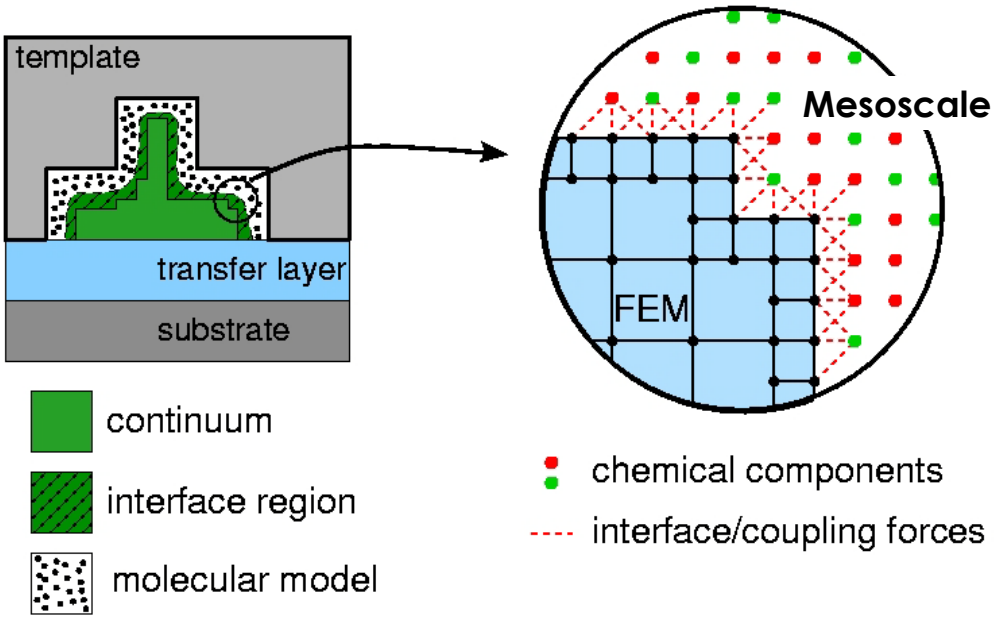

Figure 3.1. Cartoon of the possible mapping of the multiscale model in the SFIL shrinkage simulation.

3.2 Model Components

The multiscale model consists of three distinct regions. The fine scale model which is the mesoscale model described in Chapter 2, a continuum model and the interface where the gluing takes place. Each will be discussed in terms of possible methods and the methods used to calibrate them. The simulations and data used in

calibrating the models have been completed with a more simplified component system that is well characterized. This system is poly(methyl methacrylate). In this model, the lattice population routine contains only one monomer in this case.

3.2.1 Mesoscale Model Calibration

The mesoscale model is treated as the truth and it is from this model that the error estimation is made. Thus the model must reflect the real physical properties of the material. In order to get the correct potential parameters for the model, an inverse problem was formulated to calibrate the parameters to actual experimental data.

In order to do this calibration, I used the inverse model formulated by Chetan Jhurani, a graduate student in ICES. The inverse problem is basically an optimization problem where simulated experiments are conducted and then the results are compared to actual experimental data. The experimental data are based on uniaxial tensile experiments (Table 3.1).[2] The inverse problem uses the steepest descent method to minimize the error as a function of the potential parameters for the harmonic spring case. A more in depth description of the method can be found in Appendix B.

Force (N)	350	650	1100	1350	1750
Stress (MPa)	7	13	22	27	35
Axial strain(%)	0.25	0.5	0.75	1	1.25

Table 3.1 Tensile data used in the calibration of the potential parameters for the mesoscale model.

The basic algorithm to the inverse problem is as follows:

1. Apply the force the desired force to the relaxed feature
2. Minimize the energy and then calculate the strain

3. Compare the strain to the experimental value, if within the tolerance stop
4. Else update the potential parameters and repeat

3.2.1.1 Calibration Results

My simulated experiments were conducted on cubic features and then scaled against the true experiment's dimensions. The lattice spacing was held constant and the spring constants allowed to vary. The initial potential used to represent both bonded and non-bonded interactions was a harmonic potential. In order to find an appropriate representative volume element multiple cases were run on different size cubes to find where the parameters vary the least over multiple realizations. It was found that the 50 monomer cube was the appropriate representative volume element.

Size XxYxZ	Bonded Spring ($J/Å^2$)	Non-bonded Spring ($J/Å^2$)
10x10x10	$9.2x10^{-12}$	$2.1x10^{-12}$
20x20x20	$1.3x10^{-10}$	$5.2x10^{-11}$
50x50x50	$5.1x10^{-12}$	$4.7x10^{-12}$

Table 3.2. Inverse problem results for the spring parameter estimations of three different cubes.

In order to run the inverse problem and achieve results in a timely manner, Lonestar, a Dell cluster system, from the Texas Advanced Computing Center was utilized. For the 10 monomer unit cube, it was possible to run the inverse problem on eight processors and get about one result a day. The 20 monomer cube unit, was run on

ten processors and gave one result in about a day and a half. The 50 cube case was run on 40 processors and took about forty hours for one solution in some cases and in other cases the forty-eight hour limit of the Lonestar system was exceeded before an appropreiate solution was found.

The procedure for each inverse case run was first to create a polymer lattice of the proper size from the mesoscale code. The lattice data were then uploaded to Lonestar where the inverse problem was run. The starting guess for the lattice constants was changed after several successful solutions to decrease the computation time. The requirement for the acceptance of the calculated spring constants was that the calculated points of the stress-strain curve were within ±20%. An example of the convergence of the spring constants can is shown in Figure 3.2. An example of the stress-strain for several iterations can be seen in Figure 3.3.

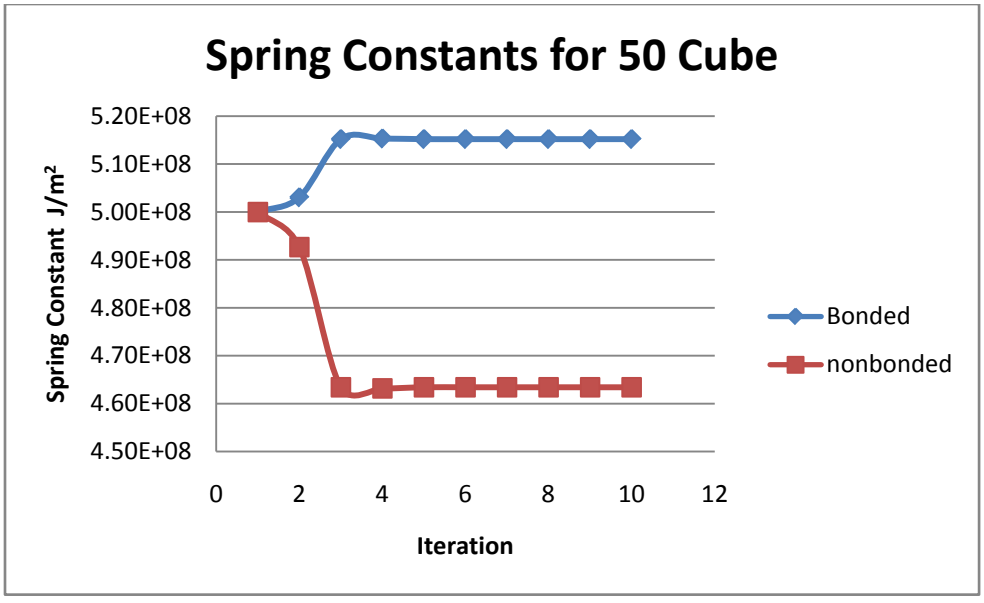

Figure 3.2. Inverse problem results for one realization of a 50 monomer cube for a harmonic potential.

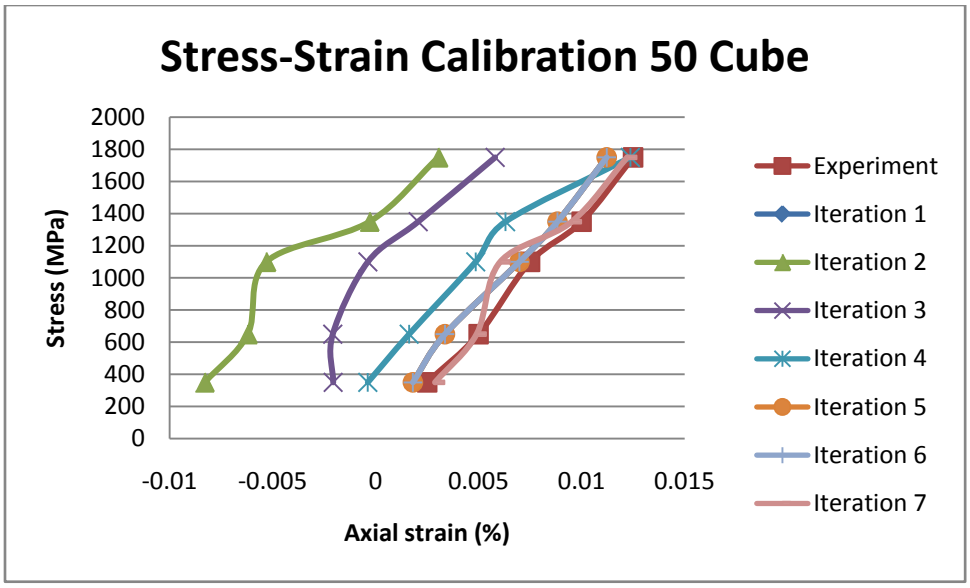

Figure 3.3. Inverse calibration to the experimental stress-strain data shown are the results for one realization of a 50 monomer cube.

3.2.1.2 Calibration Discussion

The results of the calibration show that the calculated k_{eff} in Table 2.4 are several orders of magnitude greater. It is also interesting to see that two of the cases the spring constants for the bonded and non-bonded springs are of the same order of magnitude. Since the relationship between the two is hard to put into physical description it was thought that by switching from harmonic potentials to that of potentials which parameters more easily related to physical properties.

3.2.1.3 Inverse Problem Improvements: Other Potential Models

The inverse problem has been adapted to utilize two other potential models. The first is a mixed potential that uses the Lennard-Jones 6-12 potential for the non-bonded interactions and the other a harmonic potential for the bonded interactions. The other is

the finitely extensible nonlinear elastic, FENE, potential which again uses the Lennard-Jones 6-12 potential for the non-bonded interactions and uses Equation 3.1 for the bonded interactions:

$$-33.75 * \varepsilon * \ln\left(1 - \left(\frac{r}{1.5*\sigma}\right)^2\right) \quad (3.1)$$

where ε and σ are the Lennard-Jones potential parameters and r is the distance between monomers.

The mixed potential was chosen to be closer to more realistic interactions between monomers. The FENE is an even better approximation with the bonus of having consistent parameters between the two potentials. Unfortunately, the current inverse solver was not able to calibrate the models as it stands. Once the calibration began reducing the error it ran into an area where numerical errors were received. More work will have to be done to find a way to adapt the algorithm to these other potential models.

3.2.2. Continuum Model

The continuum model is based on the model of a compressible Mooney-Rivlin material. The model is formulated on the principle invariants of the right Cauchy-Green deformation tensor. These three invariants can be written in terms of the principle stretches of the material line elements shown in Equations 3.2-3.4.

$$I_1 = \lambda_1 + \lambda_2 + \lambda_3 \quad (3.2)$$

$$I_2 = \lambda_1\lambda_2 + \lambda_2\lambda_3 + \lambda_1\lambda_3 \quad (3.3)$$

$$I_3 = \lambda_1\lambda_2\lambda_3 \quad (3.4)$$

The Mooney-Rivlin written in terms of the principle invariants is given in Equation 3.5. In order to calibrate the model, three coefficients must be found: C_1, C_2, and C_3. The calibration was done by performing both uniaxial tensile experiments as well as biaxial tensile experiments on polymer realizations from the mesoscale model and equating the total energy density calculated from the mesoscale model to continuum energy, W. The representative volume element for determining the coefficients was a 30 cube. The values found for the coefficients are C_1 (0.67), C_2 (0.23), and C_3 (0.22).[3]

$$W = C_1(I_1 - 3) + C_2(I_2 - 3) + C_3\left(\sqrt{I_3} - 1\right)^2 - (2C_1 + 4C_2)\ln\sqrt{I_3} \qquad (3.5)$$

3.2.3 Arlequin Method

One way to marry models of different scales is the Arlequin method.[4] This method differs from other methods in that at the intersection of the models at the interface region the models are glued together. Thus the method allows for the superposition of models of different scales, it allows for the conservation of local energy via weighting functions and transfers energy between the models via the gluing zone. The models are constrained at the gluing zone with Lagrange multipliers ensuring compatibility of the two models.

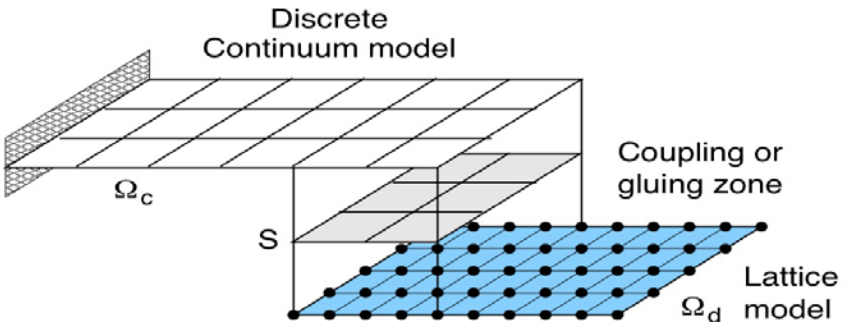

Figure 3.4. Visualization of the Arlequin method, showing the gluing region, where both model the continuum model and the lattice models coexist. [3]

Paul Bauman formulated the multiscale model using the Arlequin method with the mesoscale model and the nonlinear elastic continuum model.[3] The coupling was done using a linear interpolation of the displacements between the two models at the interface or overlap region, S. Thus the weighting functions for each model vary linearly across the overlap region.

In order to judge which areas need to be modeled by which model, as well as the size of the interface region necessary to properly glue the models error estimation is preformed. Once it is known which areas contain the highest error it is then possible to perform enrichment and reassign the models in that area to reduce the error. It is possible to have the code automatically adapt the models to reduce the error.

3.3 ADAPTIVITY

The error estimation, the difference in the result of a pure mesoscale simulation from the multiscale scale case, is performed by comparing the current continuum configuration with that of a similar particle region. The error is estimated by projecting

particles onto the continuum configuration and interpolating their displacement and then comparing the error in the projected particles. The adaptive algorithm written by Paul Bauman uses the error estimation to then partition the error over the domain, find the regions of highest error, assign those regions as mesoscale code, then reconfigure the overlap region and solve the enriched problem.[3] This enrichment process continues until the error is within a given tolerance.

An example of the enrichment process using a uniform springs case can be seen in Figure 3.5. The uniform springs case assumes that all monomers are bonded in all major axes with the same spring constant, this is a highly ideal case. The area of interest in this case is defined as the displacement of the center most portion of the top of the cube. The pink area represents where the mesoscale code is used, the red area is the interface region and the green area is where the continuum model is utilized. As seen in Figure 3.5, the uniform springs case has symmetry. The need for multiple enrichments is due the small problem size.

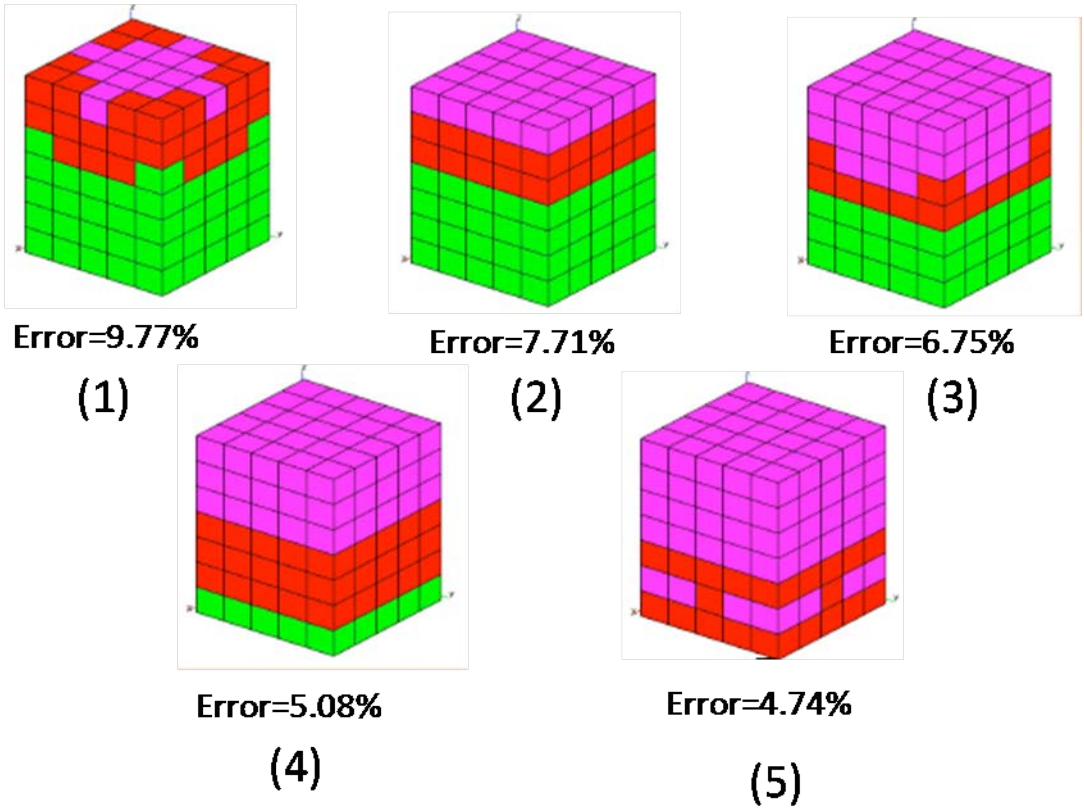

Figure 3.5. Solutions from the adaptive algorithm for a uniform springs case with the displacement of the center portion of the top of the cube defined as the area of interest.[3] The pink portion represents the mesoscale code, the red is the interface region and the green is the continuum. It took five enrichment steps to lower the error to less than five percent.

In Figure 3.6, the same quantity of interest is considered for a case derived from the mesoscale code for PMMA. The loss of symmetry highlights the stochastic nature of the polymerization greatly effects the solution as well as the error. The need for the large level of enrichment is due to the small problem size.

While this method can work on small scale features, the need to calculate the full mesoscale code to get the error is not practical. Other methods of error estimation must be evaluated in order of the adaptive error-estimation routine to work.

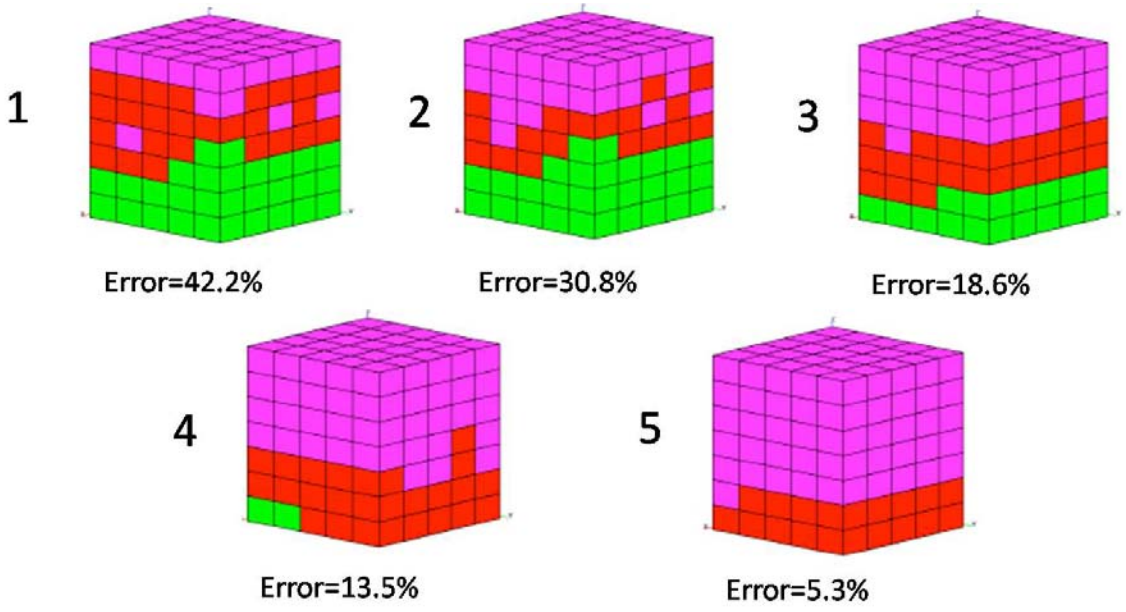

Figure 3.6. Solutions from the adaptive algorithm for a PMMA case with the displacement of the center portion of the top of the cube defined as the area of interest.[3] The pink portion represents the mesoscale code, the red is the interface region and the green is the continuum. It took five enrichment steps to lower the error to about five percent.

3.4 CONCLUSIONS

The multiscale code with adaptivity is a viable option for simulating features created in the SFIL process if a specific quantity of interest is desired. The code is still computationally intensive and is not suited to run on a single processor. The code lays the frame work that can readily adapt to study such things a template release from the mold if a better method of error estimation can be found.

The calibration of the mesoscale code was run for the pure harmonic potential model. The representative volume element was found to be a 50 monomer cube. The calibrated spring parameters were of the same order magnitude for both bonded and nonbonded interactions and 6 orders of magnitude smaller than those calculated in

Chapter 2. Work was begun on adopting the inverse problem to work with other potentials systems.

3.5 REFERENCES

1. Marin, G. B., *Advances in Chemical Engineering: Multiscale Analysis [electronic resource]*. Elsevier: Burlington, 2005; p 323.

2. Naqui, S. I.; Robinson, I. M., Review Tensile dilatomeric studies of deformation in polymeric materials and their composites. *Journal of Materials Science* **1993,** 28, 1421-1429.

3. Bauman, P. T. Adaptive Multiscale Modeling of Polymeric Materials Using Goal-Oriented Error Estimation, Arlequin Coupling, and Goals Algorithms. University of Texas, Austin, 2008.

4. Ben Dhia, H., Multiscale mechanical problems: the Arlequin method. *C. R. Acad. Sci., Ser. IIb: Mec., Phys., Astron.* **1998,** 326, (12), 899-904.

Chapter 4

This chapter introduces the background on the creation of pillar arrays. It highlights the work done to recreate the initial findings as well as our efforts to expand the knowledge of how materials and the electric field effect such things as pillar spacing, size and the time scale to formation. It introduces multilayer systems and their novel pillar structures.

4.1 Background of the Creation of Pillar Arrays

The technique for creating pillar arrays in thin films was first documented by Dr. Chou's research group at Princeton University. The arrays were formed during a nanoimprint lithography experiment.[1] The imprint process failed due to the presence of dust particles which prevented intimate contact of the template with the molten polymer film. The dust created a small air gap between the template and the liquid polymer film; it was across this gap that the pillars formed. These findings were replicated by placing a template above a thin film using spacers to control the gap size. The entire set-up of the template, polymer film and substrate were then uniformly heated above the polymer's glass transition temperature (Tg) and then cooled to harden pillars in place, it was theorized that a thermal flux caused instabilities to form and span the gap.

At the University of Massachusetts, Dr. Russell's group modified Chou's approach by applying an electric field across the polymer film heated above its Tg, creating a capacitor like device see Figure 4.1. This method was tested on a variety of

homopolymers. The method was dubbed electrostatic lithography.[2] Thus, the pillar formation process was further elucidated.

Dr. Chou group also utilized electric field to destabilize the molten films and further added a patterned top template to adjust the gap and thus the electric field strength. This method was dubbed lithographic induced self-assembly (LISA).[3] Following up on this the group found by having a smaller gap the pillars would coalesce together and form a replica of the features on the patterned top electrode. This method was dubbed lithographic induced self-construction.[4] With this work the effects of patterned templates on pillar formation was introduced.

Pillars form when a destabilizing force amplifies undulations in thin films. In order for pillars to form, the destabilizing force needs to overcome the surface tension at the air-polymer interface, which acts as a restoring force. The destabilizing force could be generated by an applied electric field or by a thermal flux. The undulations grow until they span the gap between the template and substrate. With this basic understanding of the process models were formulated.

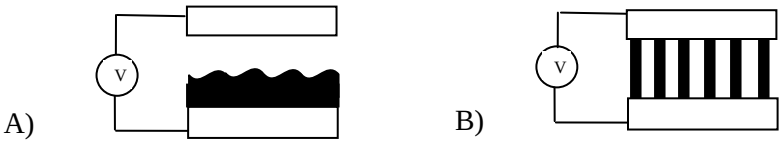

Figure 4.1. The formation of a pillar array. A) The initial spun coat film with top electrode placed above to create the capacitor live device. B) After the potential is applied the pillars form and grow to span the gap between the electrodes.

4.2 MODELING THE PILLAR FORMATION PROCESS

Schaffer et al.[2, 5] employed linear stability analysis to model the pillar formation process and assumed the polymer film was a perfect dielectric. This model showed that the pillar spacing varied inversely with the electric field, following experiment data. The model was also able to match the predicted fastest growing wave lengths to the experimental spacing. Lin et al.[6] added to Schaffer's model by adding the affect of a dielectric medium other than air in the gap. Russell and Pease[7] developed a leaky dielectric model, finding pillar formation will be less orderly for leaky dielectric materials than a perfect dielectric. Pease and Russel[8] also showed that at small surface tension and large electric fields the lubrication approximation fails. Models have also been formulated for alternative pillar patterns such as cylindrically symmetric systems.[9] Several nonlinear models have been developed that try to capture the fine details in the patterning process.[10-12] All of these models capture the initial pillar process but they all tend to fail at longer time periods in the formation process. That being said the models highlight the main factors to be studied in the pillar formation process.

The determining factor for pillar stability within a given system is partially governed by the fill factor. Pillar stability refers to the fact that under certain conditions pillars form and then coalesce into other structures. The fill factor is defined as the total gap distance between the template and the film divided by the height of the film, see Figure 4.2. Models have predicted three main behaviors based on the fill factor for a flat template.[12] For a fill factor of 1/3, pillars form quickly and coalesce together, then lines,

and after a long period of time holes are the only distinguishable features. For a fill factor of one, pillars form in a generally unordered manner then coalesce. For a fill factor greater than three, pillars form into hexagonal closed spacing and persist without coalescing for long periods of time.

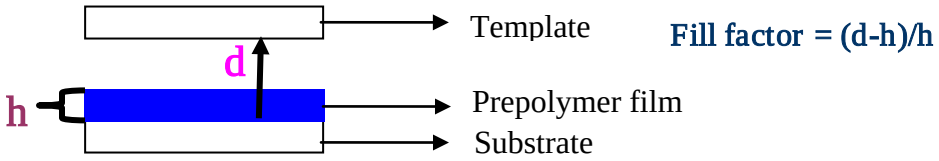

Figure 4.2. The fill factor is defined as the gap between the film and the top electrode divided by the film thickness.

Michael Dickey[13] refined these models and developed an expression that predicts the fastest growing wavelength determines the characteristic spacing of the pillars. The expression for the characteristic wavelength is shown below:

$$\lambda = 2\pi\left(\frac{\gamma U}{\varepsilon_o \varepsilon_p (\varepsilon_p - 1)^2}\right)^{\frac{1}{2}}\left(\frac{U}{\varepsilon_p d - (\varepsilon_p - 1)h}\right)^{\frac{-3}{2}} \qquad (4.1)$$

where U is the applied voltage, γ is the surface energy of the polymer, ε_p is the dielectric constant of the polymer, ε_o is the permittivity of air in vacuum, d is the gap, and h is the thickness of the film. Equation 4.1 shows that increasing the voltage decreases the pillars' spacing and size.

Another useful equation in modeling the pillar formation process is the character disturbance growth rate, s, which is the inverse of the time scale of growth.[13]

$$s = \frac{h^3}{\mu}\left(\frac{2\pi}{\lambda}\right)^2\left(-\gamma\left(\frac{2\pi}{\lambda}\right)^2 + \epsilon_0 \frac{U^2}{\left(d+\frac{\epsilon_0-\epsilon_p}{\epsilon_p}h\right)^3}\frac{\epsilon_0-\epsilon_p}{\epsilon_p}\right) \quad (4.2)$$

Equation 4.2, highlights the fact that time scale for growth of the pillar arrays is directly proportional to the material's viscosity, since it is the inverse of s. Thus materials of low viscosity are good candidates for study.

Our initial goal was to investigate the material and electric field effects on such things as the pillar spacing, the pillar size as well as the time scale to formation.

4.3 Experimental Setup: Homopolymer films

The first polymer systems studied were poly(methyl methacrylate), PMMA, and poly(styrene), PS, this was due to the work already published work on the pillar formation by the two systems.[5] PMMA and PS of various molecular weights were tested to gauge the best conditions for pillar formation.

In collaboration with Michael Dickey[13] experiments were conducted that utilized a microscope slide as the top template. This template is created in a two step process (Figure 5.3). The gap area was created through an etch step, usually a buffered oxide wet etch, in the desired area of the slide. The depth of the etch was controlled by the etch time and was measured via profilometry. The etched area was then rendered electrically active through the deposition of a conducting metal, chromium or indium tin oxide (ITO) film, by thermal or e-beam evaporation. The thickness of the deposited metal can affect

the template's transparency which can be a troublesome for tracking the pillar formation process.

The monomer thin film was created by spin coating the monomer system onto a conducting substrate, such as a doped silicon wafer. The thickness of the film is readily adjustable through the spin rate or via dilution of the monomer with solvent. The film's thickness was measured by ellipsometry. The films were confined to the active area of the template by carefully washing the extraneous film away.

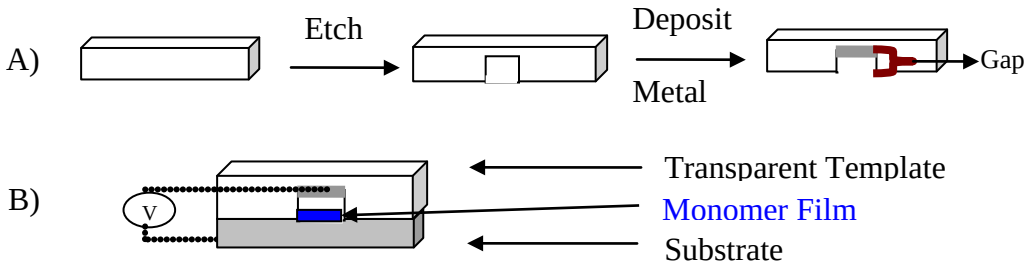

Figure 4.3. Experimental Setup A) The template is made in a two step process in order to create the recess which creates the gap between the top electrode and the monomer film. B) Setup prior to pillar formation.

The template was placed over the monomer film and secured in place with binder clips. Electrical contact was made to the substrate and the deposited metal on the template. If the deposited film is thin enough, pillar formation can be monitored using an optical microscope. The time frame for pillar formation is on the order of several minutes due to the need to heat the film above the films Tg. Pillars are locked into place by quickly cooling the film to room temperature.

Unfortunately, this setup had several limitations and drawbacks. The binder clips and the applied electric field often caused the system to bow, this led to an uneven gap across the active area and pillars of multiple sizes or the system would bow enough to make contact with the top electrode and short. Also dust would often interfere and cause the gap to be greater than originally designed. A new method was sought that could maintain a constant gap between two substrates over a large area in the presence of an electric field for further experiments. This problem led to a collaboration with Professor S.V. Sreenivasan and graduate student Allen Raines to produce a tool that could keep the template and the wafer at a constant gap under the electric field, this tool is discussed in Chapter 5.

4.3.1 Typical Experimental Conditions

The monomer films were formulated to be one to two micron thick. The gaps etched in the microscope slide were typically two to eight micron thick with four microns being the mean gap used. A typically formulation was a 15 weight percent solution of PMMA in chlorobenzene which was spin cast at 2500 RPM and then baked at 90^{o}C for thirty second to remove excess solvent. The film was then carefully removed from the area that is outside of the gap area or active area by washing. The top electrode was then attached via the binder clips. The electrode stack was then either placed on a hot plate or in an oven. Electronic connection was made to both the top and bottom electrode via alligator clips. The film was then heated above the homopolymer's Tg, usually to 120 ^{o}C. Once the film had been above the Tg for several minutes, voltage was applied as a

step function. The typical voltage used was about 150 to 200 volts for a four micron gap. If the metal film on the top electrode was thin enough, pillar formation could be tracked visually by the appearance of a diffraction pattern. Experiments were required run times of 30 to 45 minutes to complete after the voltage was applied. A typical result can be seen in Figure 4.4. This result is consistent with the literature.

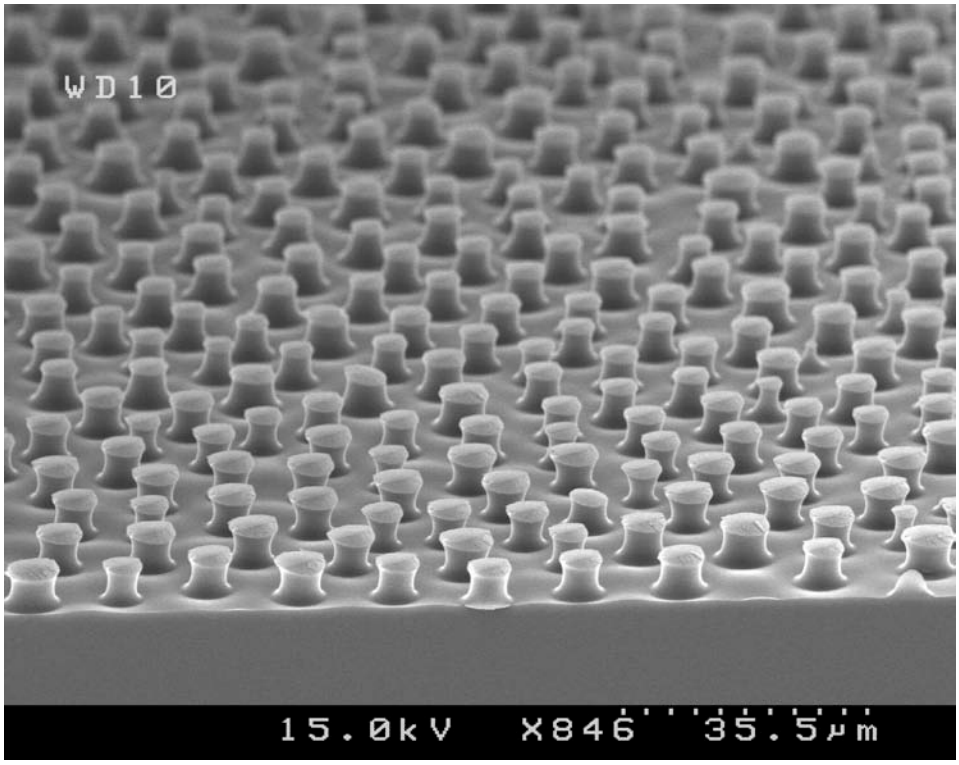

Figure 4.4. A typical PMMA sample of pillar arrays.

In collaboration with Micheal Dickey,[13] I demonstated that while the electrode stack is still intact and after the pillars have formed it is possible to use the pillars to create a porous membrane. This is done by wicking a material such as poly(ethylene glycol) diacrylate, PEG diacrylate, with some Darocure 1173 into the gap area. The PEG diacrylate can be cured via UV exposure through the microscope slide. Once cured the

electrode stack can be disassembled. The pillars can then be removed by exposure to a selective solvent in which they are soluble and that the PEG diacrylate matrix is insoluble in. A selective solvent for PS is cyclohexane, while for PMMA acetic acid is used. A membrane created in this fashion from PS pillars dissolved in cyclohexane is shown in Figure 4.5. This work was eventually published with a different set of authors.

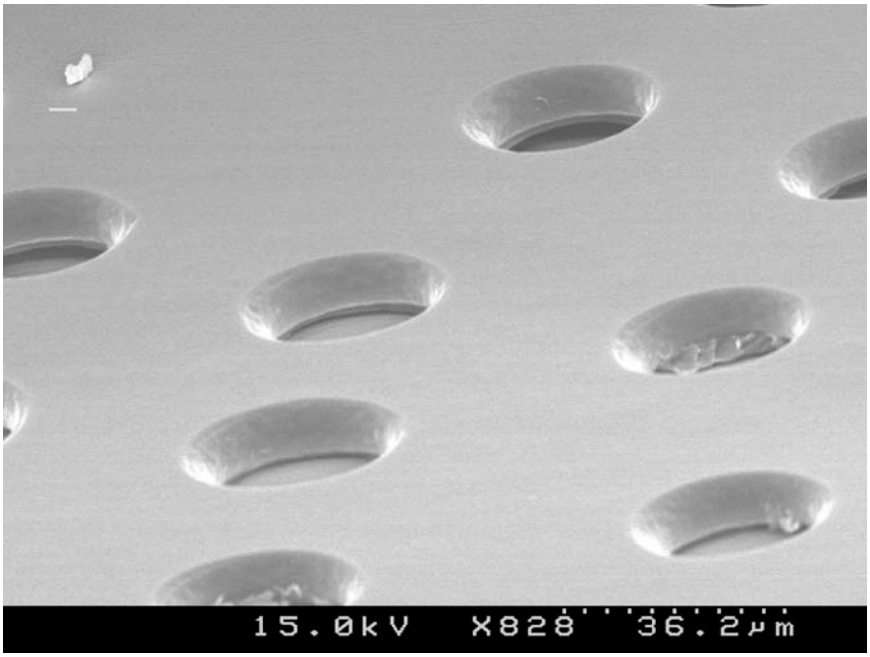

Figure 4.5. Porous membrane template that resulted from the removal of PS pillars from a PEG diacrylate matrix through exposure to cyclohexane.

4.4 MULTILAYER PILLAR STUDIES

Homopolymer films tend to be insoluble with one another and have different dielectric constants. By laying homopolymer films and introducing an electric field across them, hierarchical structures can be formed due to the internal forces between the the polymers.[14-16] In order for the homopolymer films to form layers correctly, they need to be cast from solvents that do not interact with the previously deposited film.

Prior studies had shown that in a PS on PMMA system, that after the PS columns have grown the PMMA would form a sheath around the PS pillar and grow up to the electrode.[16] With this in mind, experiments were carried out in which a second film was spin coated on top of the first film after it was baked. This required selective solvents for casting the films such that the casting of the second film would not remove the first. The chosen solvents were toluene for PS and chlorobenzene for PMMA. The top film was chosen to be thinner than the bottom film since the bottom film would encompass the structures formed by the top film. In collaboration with Michael Dickey[13] and some University of Massachusetts graduate students experiments were carried out on these bilayer systems.

4.4.1 PS Films on PMMA- Bilayer Experiments

I concentrated my efforts on the PS on PMMA bilayer system. The experiments were conducted by first spinning coating the PMMA solution onto a n-doped silicon wafer. The film was then baked at 90 ^{o}C for approximately thirty seconds. Once cooled the PS solution was then cast over the PMMA film and again baked at 90 ^{o}C for approximately thirty seconds. The film which was outside the active area was selectively washed away. The top electrode was the attached over the remaining film stack and held in place by binder clips. The pillar formation process was then broken into two heating cycles. The first cycle the film stack was heated to 120 ^{o}C, once at temperature the voltage was applied, typically 150-200 V. After visual evidence of pillar formation was confirmed, typically 30-45 min, the film stack was heated to 190 ^{o}C, with the potential maintained. These conditions were maintained for 45 minutes, after which the films were cooled to room temperature and the potential was removed.

In order to study the pillar formation process, the experiments were stopped at different points to capture the growth of the outer PMMA layer. The PS portion of the pillars was removed via a cyclohexane wash. It was found that the PMMA tends to grow in finger like tendrils up the PS pillar, see Figure 4.6 and Figure 4.7. PMMA has a more preferential interaction with the chromium layer on the top electrode so it displaces the already present PS. The PMMA then can encapsulate the PS, creating a concentric structure, see Figure 4.8. PMMA is easily spotted in the SEM due to the fact that PMMA is an electron beam resists and deforms in the SEM. The fact that the structure in Figure 4.8 is not fully encapsulated is most likely due to contamination on the template that preferentially favored PS. This behavior can be reproduced by coating the template with a fluoropolymer that favors PS interactions.[14]

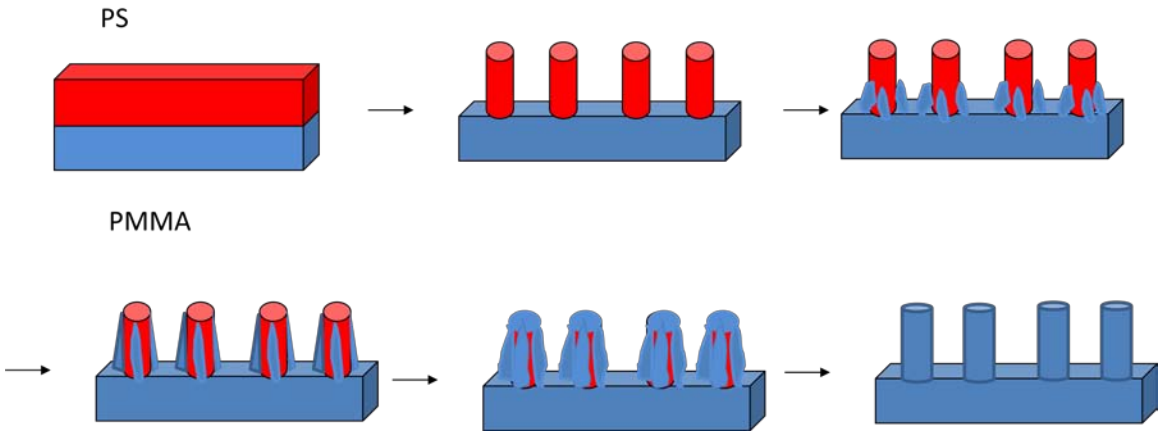

Figure 4.6. The growth of PMMA pillars over already formed PS pillars tends to begin as finger like tendrils that grow up the PS pillars. The tendrils grow up to the electrode surface where the PMMA preferentially wets and displaces the PS. The PMMA finally covers the entire PS column.

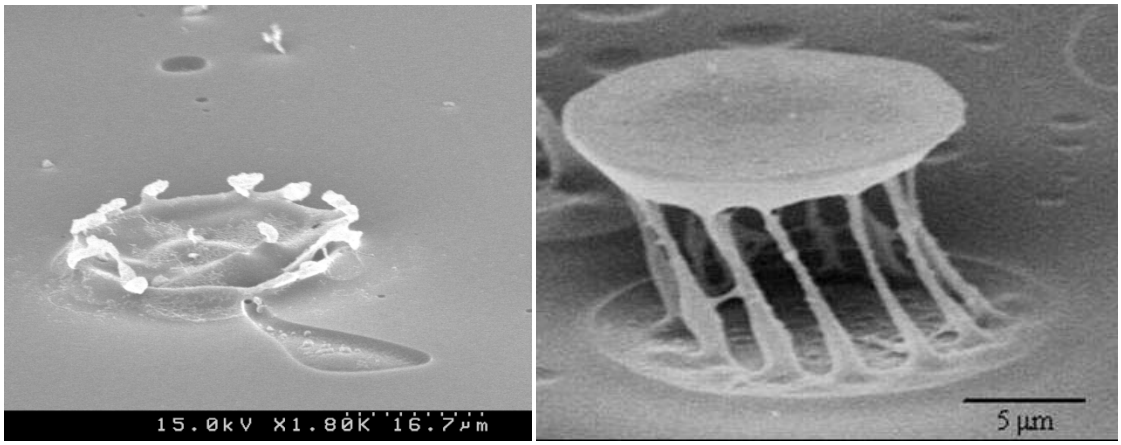

Figure 4.7. Left: SEM image of initial PMMA finger like growths over a PS column which was removed by exposure to cyclohexane. Right: SEM by University of Massachusetts collaborators of later growth of PMMA over PS columns that have been removed by cyclohexane. PMMA preferably wet the chromium and displaces the PS, creating a cage-like structure.

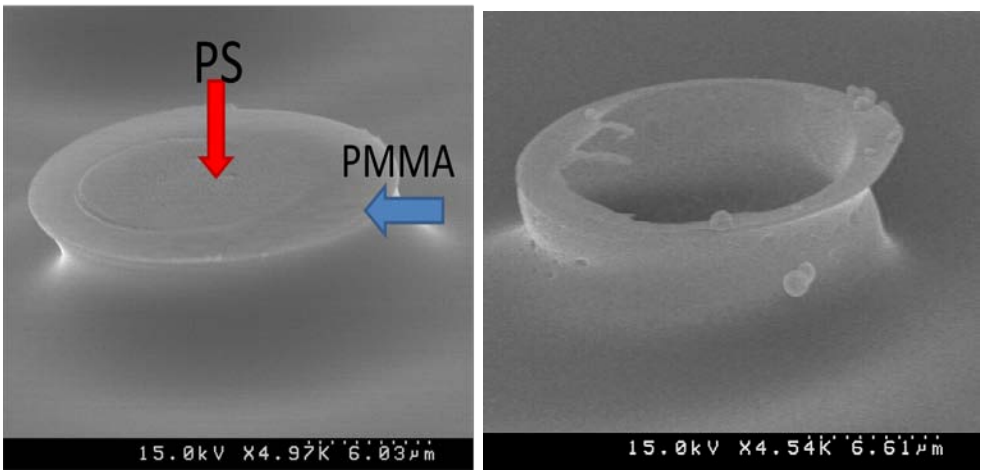

Figure 4.8. Left: SEM of concentric pillars I formed from a PS on PMMA system. Right: SEM of the sample after treatment with cyclohexane to selectively remove the PS portion.

The fact that these hierarchical structures can form is due to the differences in the hoomopolymer and hence the differences in the time scale to formation. The PS-air interface has the lowest time scale to formation and thus pillar form there first. The PS-PMMA interface has the longest time scale to formation since viscous flow from both polymers is required. Thus the PMMA can act like a substrate even above its Tg and allow the PS pillars to form first. Due to the fact that the homopolymers are insoluble, they try to minimize surface contact and can then form the concentric structures.

4.5 CONCLUSIONS

Homopolymer systems heated above their Tg can create pillar arrays readily. There is very little control of ordering in the pillar formation other than initiating at the edges of the top electrode. This is consistent with literature. Biliayer systems form more unique structures due to the immiscibility of the homopolyer films. In the case of PS on top of a PMMA film it was found that the PS pillar forms first and the PMMA then grows over the PS pillar as fingers before encapsulating the PS pillar.

The main drawback to this method is the process time. The polymer films must be heated above their Tg's before pillars can form. The high viscosity of most polymer melts leads to slow pillar formation. Once pillars form the films must be cooled to lock the pillars in place. This process can take hours. The ability to use multilayer systems to form unique structures is an added benefit to this process. The process can easily be accelerated by skipping the heating and cooling cycle by using photocurable liquids as starting materials that are liquids at room temperature and crosslink into stable features upon exposure to UV-light. This new set-up will also require a transparent electrode to allow the film to cure. I set out to explore this possibility in collaboration with Michael

Dickey and Allen Raines. Allen was responsible for the building and maintaining of the active gap tool. Michael and I shared the materials work and process optimization.

4.6 REFERENCES

1. Chou, S. Y.; Krauss, P. R.; Renstrom, P. J., Imprint of sub-25 nm vias and trenches in polymers. *Applied Physics Letters* **1995,** 67, (21), 3114-16.

2. Schaffer, E.; Thurn-Albrecht, T.; Russell, T. P.; Steiner, U., Electrically induced structure formation and pattern transfer. *Nature (London)* **2000,** 403, (6772), 874-877.

3. Chou, S. Y.; Zhuang, L., Lithographically induced self-assembly of periodic polymer micropillar arrays. *Journal of Vacuum Science & Technology, B: Microelectronics and Nanometer Structures* **1999,** 17, (6), 3197-3202.

4. Chou, S. Y.; Zhuang, L.; Guo, L., Lithographically induced self-construction of polymer microstructures for resistless patterning. *Applied Physics Letters* **1999,** 75, (7), 1004-1006.

5. Schaffer, E.; Thurn-Albrecht, T.; Russell, T. P.; Steiner, U., Electrohydrodynamic instabilities in polymer films. *Europhysics Letters* **2001,** 53, (4), 518-524.

6. Lin, Z.; Kerle, T.; Baker, S. M.; Hoagland, D. A.; Schaffer, E.; Steiner, U.; Russell, T. P., Electric field induced instabilities at liquid/liquid interfaces. *Journal of Chemical Physics* **2001,** 114, (5), 2377-2381.

7. Pease, L. F.; Russel, W. B., Electrostatically induced submicron patterning of thin perfect and leaky dielectric films: A generalized linear stability analysis. *Journal of Chemical Physics* **2003,** 118, (8), 3790-3803.

8. Pease, L. F., III; Russel, W. B., Limitations on length scales for electrostatically induced submicrometer pillars and holes. *Langmuir* **2004,** 20, (3), 795-804.

9. Deshpande, P.; Pease, L. F., III; Chen, L.; Chou, S. Y.; Russel, W. B., Cylindrically symmetric electrohydrodynamic patterning. *Physical Review E: Statistical, Nonlinear, and Soft Matter Physics* **2004,** 70, (4-1), 041601/1-041601/12.

10. Wu, N.; Pease, L. F., III; Russel, W. B., Electric-Field-Induced Patterns In Thin Polymer Films: Weakly Nonlinear and Fully Nonlinear Evolution. *Langmuir* **2005,** 21, (26), 12290-12302.

11. Wu, N.; Russel, W. B., Dynamics of the formation of polymeric microstructures induced by electrohydrodynamic instability. *Applied Physics Letters* **2005,** 86, (24), 241912/1-241912/3.

12. Verma, R.; Sharma, A.; Kargupta, K.; Bhaumik, J., Electric Field Induced Instability and Pattern Formation in Thin Liquid Films. *Langmuir* **2005,** 21, (8), 3710-3721.

13. Dickey, M. Development of Photocurable Pillar Arrays Formed via Electrohydrodynamic Instabilities. Doctor of Philosophy, University of Texas, Austin, 2006.

14. Dickey, M. D.; Gupta, S.; Leach, K. A.; Collister, E.; Willson, C. G.; Russell, T. P., Novel 3-D Structures in Polymer Films by Coupling External and Internal Fields. *Langmuir* **2006,** 22, (9), 4315-4318.

15. Leach, K. A.; Gupta, S.; Dickey, M. D.; Willson, C. G.; Russell, T. P., Electric field and dewetting induced hierarchical structure formation in polymer/polymer/air trilayers. *Chaos* **2005,** 15, (4), 047506/1-047506/5.

16. Morariu, M. D.; Voicu, N. E.; Schaeffer, E.; Lin, Z.; Russell, T. P.; Steiner, U., Hierarchical structure formation and pattern replication induced by an electric field. *Nature Materials* **2003,** 2, (1), 48-52.

Chapter 5

This chapter introduces the use of photocurable monomer formulations for use in the pillar creation process. The goal of the study was to find photocurable systems that were amiable to the process and had various physical properties. During this work the experimental process was improved with the creation of the Active Gap Tool.

5.1 Creation of Pillar arrays from Photocurable Systems

Our goal was to find photocurable monomer formulations that create uniform stable film upon spin coating, have a rapid cure time, and a dielectric contrast with the gap medium, which is typically air. Photocurable systems are well known to the coatings industry as well as the adhesive industry. Photocurable systems are commercially available in a variety of viscosities as well as functionalities and cure mechanisms. Since the systems are well studied the pros and cons of each system are already known. Common chemistries in coating systems are free radical and cationic. In the adhesive industries epoxies are commonly used and cured via a cationic system or by heating. Hence we explored this chemistry for our application.

5.2 Photocurable Materials Studied

The material requirements for use in creating photocurable pillars include: having a uniform stable film upon spin coating, a rapid cure time, and a dielectric contrast with the gap medium, this is typically air. In order for the pillars to be stable after photocuring, multifunctional materials are required to crosslink and lock the chains into

place. The systems studied include: acrylates, vinyl ethers, epoxies, thiol-ene and maleimide systems. The physical properties relevant to the pillars process (viscosity, dielectric constant, and surface energy) were characterized and the pillar formation process was studied.[1] Some brief information on the traditional UV curing systems can be seen in Table 5.1.

Chemical Functionality	Reaction Type	Pros	Cons
Acrylate	Free Radical	Rapid curing, commercially available	Inhibited by Oxygen
Vinyl Ether	Cationic	Rapid curing, commercially available	Highly volatile, template fouling, strong adhesion force
Epoxy	Cationic	Commercially available	Slow curing, high viscosity
Thiol-ene	Free Radical	Self initiating commercially available	Electro-curing, dark curing
Maleimide comonomer system	Free Radical	Self initiating	Few Liquid Monomers, Low Soluble Solids

Table 5.1. Systems of materials examined for photocurable pillars.

5.2.1 Acrylates

Acrylates are commonly used as coating materials. Acrylates undergo free radical polymerization that can be initiated with a free radical initiator like Ciba's Darocur 1173. Acryloxy terminated polydimethylsiloxane (DMS-U22, Gelest), Figure 5.1, is an example of an acrylate studied. This monomer showed oxygen inhibition typical of acrylate systems.[2, 3] In order for the system to fully cure, the experiments had to be carried out in a nitrogen glove bag. This made the system cumbersome.

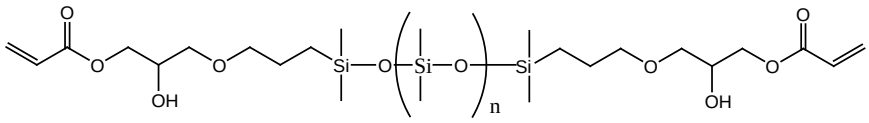

Figure 5.1. Acryloxy terminated polydimethylsiloxane, a difunctional acrylate.

5.2.2 Vinyl Ethers

Acid catalyzed polymerization of vinyl ethers is known to have a reaction rate greater than that of acrylates. The reaction proceeds via a cationic polymerization initiated by a photoacid generator (PAG) and is not inhibited by oxygen but can be quenched by base and water.[4] An example of this system is tris [4-(vinyloxy)butyl] trimellitate with Cyracure Photoinitiator UVI-6992 (Dow / Union Carbide) (Figure 5.2). Most commercially available vinyl ethers tend to be volatile and thus incompatible with pillar creation.[5] Solubility was also an issue with many of the PAGS tested. Vinyl ethers also tend to have higher adhesive forces than acrylates.[6] The adhesion forces were high enough to strip the conductive layer off the template in several experiments. The PAG was also incompatible with the indium tin oxide conductive layer since ITO is etched by acids. So research was directed to other systems.

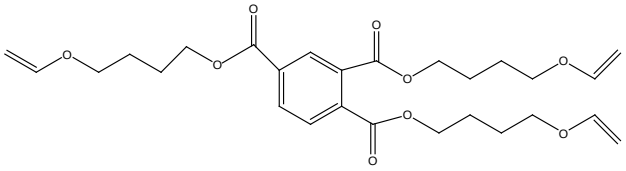

Figure 5.2. Tris [4-(vinyloxy)butyl] trimellitate, a tri-functional maleimide monomer.

5.2.3 Epoxies

The epoxy systems tested had the highest viscosity and thus the slowest pillar formation time. The epoxy polymerization proceeds by a cationic mechanism and

Cyracure Photoinitiator UVI-6992 (Dow / Union Carbide) again was used. Epon 828 from Polysciences is an example of an epoxy system that was formulated with Cyracure UVI-6992 (Figure 5.3). Due to slow formation time the epoxies where abandoned.

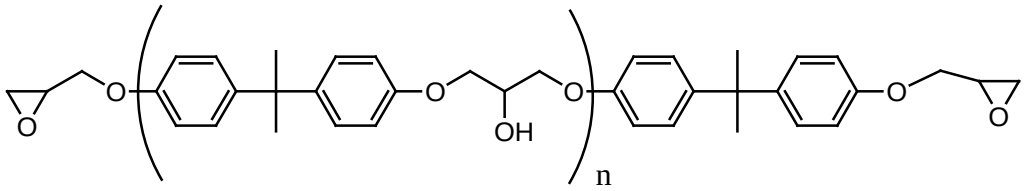

Figure 5.3. Epon 828, a difunctional epoxy.

5.2.4 Thiol-ene system

The term "thiol-ene" refers to a system in which one monomer contains a thiol functionality and one an allene. This allows for great flexibility during formulation. The order of reactivity of the thiol with various ene monomers is generally: norbornene> vinyl ether > propenyl>alkene≈ vinyl ester> n -vinyl amides> allyl ether≈ allytriazine ≈ allylisocyanurate> acrylate> unsaturated ester> n-substituted maleimide > acrylonitrile≈ methacrylate> styrene> conjugated dienes.[7] In general, the thiol reactivity decreases as stronger electron withdrawing groups are attached to the ene bond. A history of the development of this system has been published.[7, 8]

The thiol-ene reaction is self-initiating, with the thiol bond decomposing into two radicals once excited by high pressure mercury lamp. The two step polymerization process consists of a step growth reaction, followed by a chain transfer event (Figure 5.4). The step growth event consists of a thiyl radical adding across the ene bond creating a carbon centered radical. In the chain transfer event, the carbon centered radical

abstracts a hydrogen from a thiol bond, regenerating the thiyl radical. Due to this step growth mechanism, thiol-ene polymerizations due not suffer from auto acceleration.

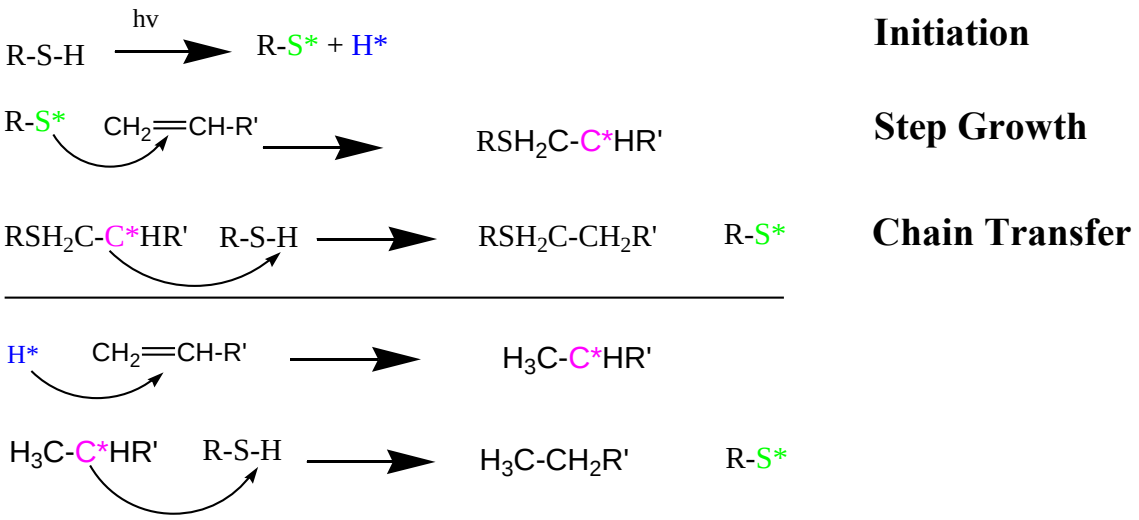

Figure 5.4. The thiol-ene reaction mechanism. Top: Initiation by the excitation of the thiol bond. Followed by, the step growth and chain transfer steps. Bottom: Second radical's pathway to the creation of a thiyl radical that can then follow top step growth/chain transfer steps.

While some free radical polymerizations suffer from oxygen inhibition, the thiol-ene reaction does not.[9] This is due to the fact that the peroxy radical generated can still abstract a hydrogen from the thiol bond, regenerating a thiyl radical. This property, along with flexibility in formulations, makes the thiol-ene an attractive system for pillar formation.

The step growth/chain transfer mechanism is an alternating copolymerization. A di-functional thiol reacted with a di-functional ene will only lead to a linear polymer. In order to get crosslinked, mechanically stable pillars, one of the monomers must at least be

tri-functional; the other must be at least di-functional. This leads to the need to control the stoichiometric ratios of the functional groups in order to get complete curing.

The main monomer used for the thiol portion of the thiol-ene system is pentaerythritol tetrakis(3-mercaptopropionate), a monomer with four thiol functional groups (Figure 5.5). The standard formulation used was a 1:1 w:w of the thiol with tris [4-(vinyloxy)butyl] trimellitate as the ene.

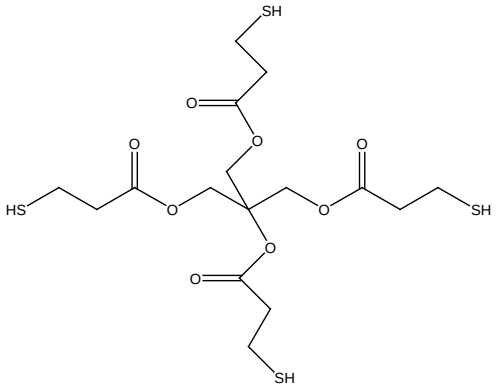

Figure 5.5. Pentaerythritol tetrakis(3-mercaptopropionate) a monomer with four thiol groups.

The thiol-ene system seemed to be ideal candidate but an unusual phenomenon was discovered. When the electric field is applied to the monomer film, it begins to polymerize. This is helpful in eliminating pillar movement but also creates some residual layer. The thiol-ene systems are also known to undergo dark curing and thus long term storage of the system is problematic. Thus, another system was sought out.

5.2.5 Maleimide system

The maleimide system is another self-initiating polymerization. Not only are maleimides capable of forming alternating copolymers[10], they are also used as photoinitatiors.[11, 12] When used as a copolymer, the system is often referred to as an acceptor/donor type. This refers to the fact that one monomer must act as an electron acceptor while the other as an electron donor. The maleimide is the electron acceptor and possible donors include: vinyl ethers[12, 13], dioxolanes[14], acrylates[15], and styryloxy[15] monomers. While working with the maleimide system some synthesis work to create maleimide derivatives was preformed, a summary of this work is in Appendix A.

While the kinetics have been studied via photocalorimetry and real-time infrared spectroscopy, the true mechanism for the copolymerization has yet to be confirmed.[13] The initiation and propagation steps are both believed to involve a hydrogen abstraction. This is reinforced by the fact that rapid polymerization upon UV irradiation only takes place when a readily abstractable hydrogen is available on either of the monomers.[13] UV exposure of the maleimide monomer results in an excited triplet state. This excited maleimide is capable of hydrogen abstraction, generating radicals. Once enough radicals are present, it is believed that the ground state maleimide reacts with the comonomer.[16] This system is not significantly hindered by oxygen.

Recent work has focused on accelerating the maleimide copolymerization rate. It has been shown that the cure rate is greatly enhanced by adding a triplet sensitizer and a tertiary amine co-initiator.[17] This phenomena has the added benefit of alleviating some

initial difficulties with curing the maleimide systems under glass although it is unnecessary with the quartz templates in the active gap tool. The cut off wavelength of light for transmission through glass is around 300 nm. Unfortunately, wavelengths around 250 nm are required for the maleimide excitation. The use of sensitizers such as Michler's ketone and thioxanthen-9-one which have high absorbencies above 300 nm enable the maleimides to cure under glass. This work also lends itself to the use of photobase generators, molecules which upon UV exposure produce a photoproduct with a basic functionality. Luckily the reaction rate may also be increased with the addition of a free radical photoinitiator like Ciba's Darocur 1173 if the ene used is an acrylate.

A generous donation by Dr. Hoyle of the University of Southern Mississippi of a liquid bismaleimide, Q-bond® (Figure 5.6) enabled a quick route to a photocurable system for pillar research. The co-monomer in this system was di(trimethylolpropane) tetraacrylate (Figure 5.6). In order to speed up the reaction, Darocur 1173 was added. Q-bond® is known to undergo homopolymerization upon exposure to UV light and its polymerization rate is dependent upon the concentration of the comonomer present.[18]

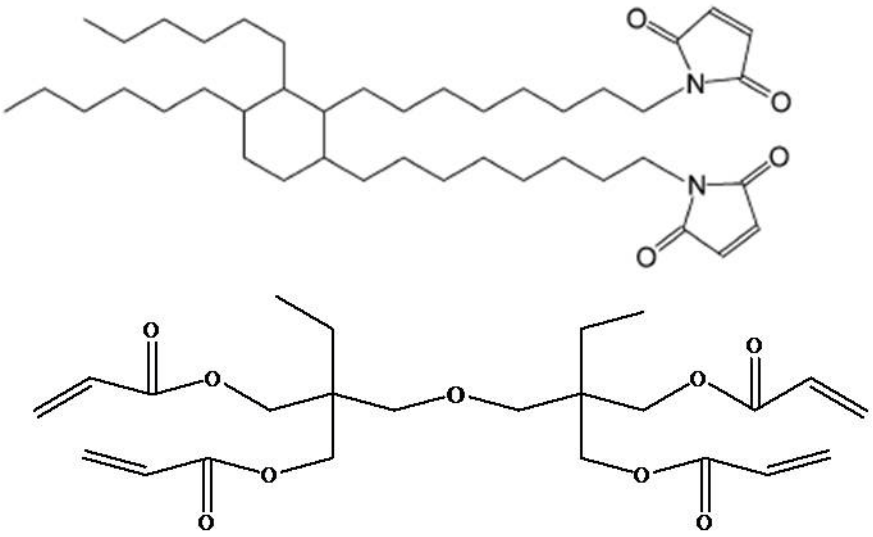

Figure 5.6. Top: Q-bond® a liquid bismaleimide. Bottom: Di(trimethylolpropane) tetraacrylate a tetra-functional acrylate.

The Q-bond®/ di(trimethylolpropane) tetraacrylate system with a small amount of Darocur 1173 was the system chosen that had the least detrimental effect on the template's conductive layer.

5.2.6 Material Kinetics

The photocurable systems' polymerization rates were evaluated via real time Fourier transform infrared spectroscopy (RTIR). RTIR is an *instu* based technique that relies on IR measurements to track the real time disappearance or appearance of functional groups.[19] The results of the systems studied are presented in Figure 5.7. From these results it can be seen that in the case of the thiol-acrylate system the acrylate portion of the system is homopolymerizing, this is evident by the extent of depletion of the acrylate functionality (Acrylate-TA) when compared to the thiol functionality (Thiol-TA). The thiol-vinyl ether system also appears to show the vinyl ether (Ene-TE) is homopolymerizing since the extent of the reaction of the thiol (Thiol-TE) is much less.

In the case of the Q-bond® system it can be seen that the relative rate of reaction for just the Q-bond® system (QB) is less than that of a mixed system (QB-VE).

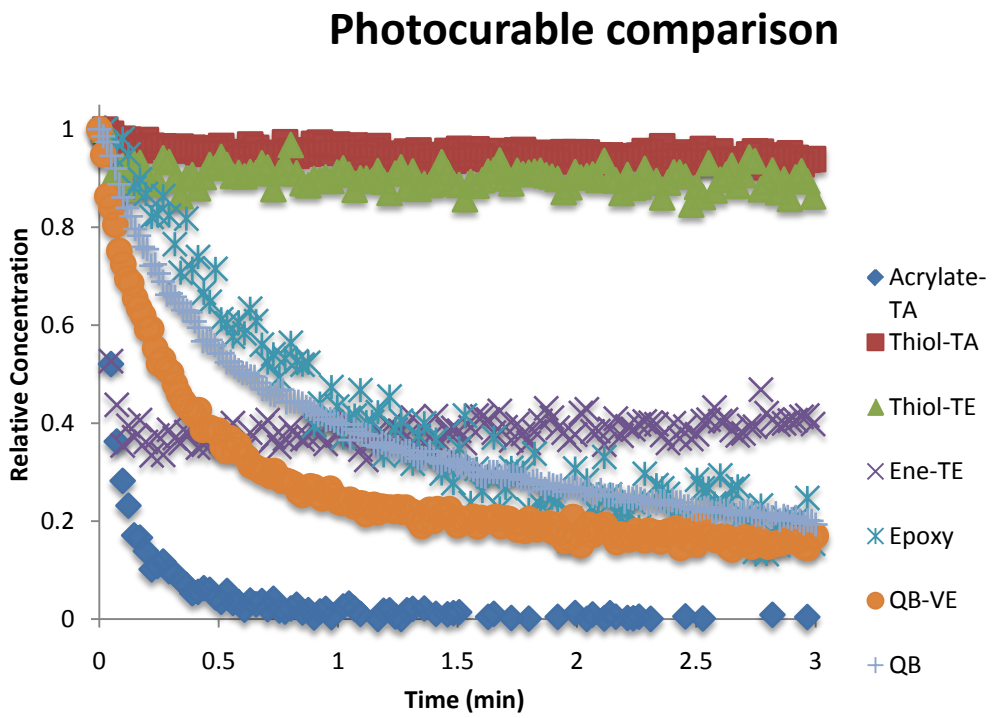

Figure 5.7. Real time IR data for some of the photocurable systems tested. The first part of the name refers to the functionality traced in the IR and the last part of the name is an abbreviation for the photocurable system.

5.3 Experimental Set-up

The initial experimental setup was the same as that of the homopolymer film experiments it consisted of an etched microscope slide as a UV transparent template, although it is only transparent to 300 nm. Due to the fact that the thickness of the deposited metal can affect the template's transparency and can hinder some

photochemistry if too thick, thinner chromium films were utilized typically on the order of 5 nm. The monomer system was again deposited via spin coating and the electrodes were held in place by binder clips. Typical potentials applied were again 100-200 V for gaps of 4 to 8 microns. Experiments were carried out in less than 5 minutes with a one minute exposure.

As noted in the homopolymer case this setup had several limitations and drawbacks. The binder clips and the applied electric field often caused the system to bow, this would lead to an uneven gap across the active area and pillars of multiple sizes or the system would bow enough to make contact with the top electrode and short. A new method was sought out that could maintain a constant gap between two substrates over a large area in the presence of an electric field.

5.3.1 Active Gap Tool

Collaboration was begun with a mechanical engineering student, Allen Raines, in order to construct a machine dubbed the active gap tool (Figures 5.8), which was capable of bringing two substrates into parallel alignment and could maintain the gap in the presence of an electric field. The machine uses three micrometer motors to bring the template into parallel alignment with the wafer. The machine is mounted on a laser bench to minimize vibrations and in a clean room to minimize particle contamination. The substrates used in this tool are 4” doped silicon wafers for the bottom substrate and a 65 mm x 65 mm quartz top template which is created from a 6025 quartz mask blank. The wafer is held in place via a vacuum wafer chuck whose stage is controlled by an air solenoid for loading and unloading of samples. The template is held into place via a customized template holder which uses vacuum as well. In the center of the template

holder, a 10 mm x 10 mm square hole is cut out to allow UV light exposure through the back of the template.[20]

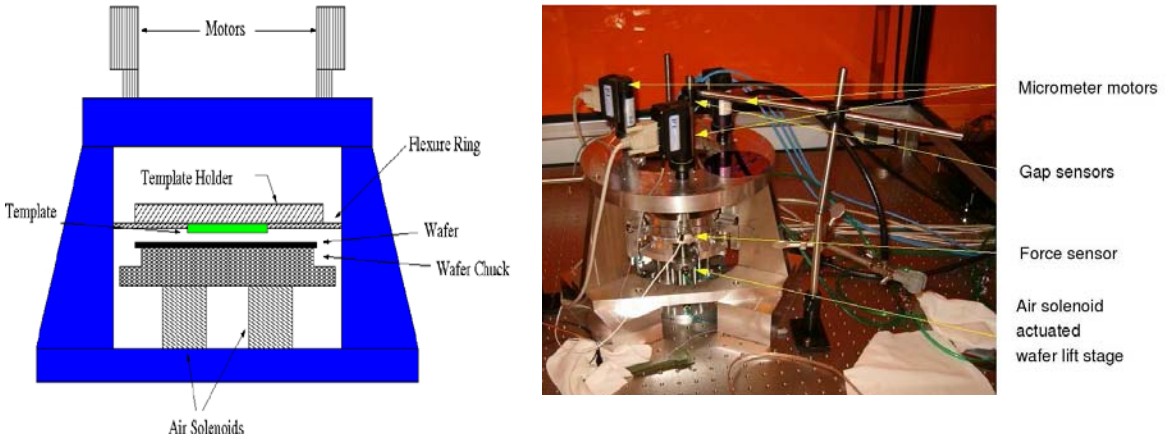

Figure 5.8. Left: a two dimensional representation of the active gap tool with the motor arms left off for clarity purposes. Right: an actual picture of the active gap tool.

Gap sensing is carried out optically via four sensors using white light interferometery. Three of the sensors are arranged permanently in a one inch circle around center of the template holder and the fourth sensor is in the center of the template where the hole is cut to allow curing and is removable to allow the light guide access for curing. The substrates are brought into planarity by reading the differences in the sensors' measurements and adjusting the different motors' positions. The ability to adjust the templates and substrate gap also allows for the increase in the aspect ratio of the formed pillars by stretching the liquid pillars before curing them.[21]

In order to reduce both the electric force and the adhesion forces on the template a one inch square mesa is created via lithographical means in the center of the template. This mesa area is considered the active area where the experiments take place.

The longest part of the experiment was getting the alignment of the template with the wafer. Typically voltages applied were 40-60 V for a four micron gap with films

typically one micron thick. The potential was generally applied for about 5 minutes and the film was cured with a Novacure mercury arc lamp with a 60 second exposure.

Unfortunately, in this original configuration the machine was not stiff enough to maintain gaps below one micron and would often suck down under the influence of the applied electric field onto the wafer and destroy the pillars. Thus an effort was undertaken by Allen Raines to stiffen the machine.

5.3.2 Hybrid Active Gap Tool

The hybrid active gap tool uses voice coils in addition to the micromotors and peizoes to counteract the applied electrical force and maintain the gap.[20] The template's active area was also reduced to a 10 mm square to reduce the overall forces, this change complicates the alignment of the substrates due to the fixed sensor arrangement. The template holder had to be replaced to accommodate the voice coils (Figure 5.9). The machine is now capable of maintaining 400 nm air gaps. Unfortunately, over time there is drift in the system about from 100-50 nm/ minute which can be attributed to the relaxation of the motors and peizoes and adjustments to temperature variations. It is with this tool that the majority of the experiments discussed in this chapter have been done.

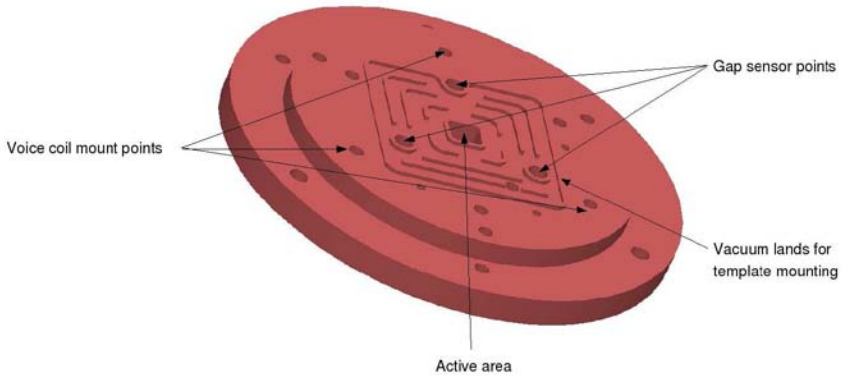

Figure 5.9. The design for the template holder for the hybrid active gap tool.[20]

5.4 CONCLUSION

The use of photocurable monomers offers significant advantage in creating pillars via amplification of electrostatic instabilities. The time frame for the experiment is orders of magnitude less than that of homopolymers above Tg. The need for a transparent top electrode is easily accomplished. There already exist a variety of photocurable systems which allows for great flexibility in formulated systems. The two systems that lend themselves best to the pillar creation process were the thiol-ene and maleimide system. The use of the Hybrid Active gap tool allows one template to be used at a variety of gap sizes and thus allows for more flexibility in creating pillar arrays. The Hybrid Active gap tool also provides a means to increase the aspect ratio of the pillars by allowing the stretching of the still liquid pillars before they are locked into place when exposed. With the ground process work laid finding the ideal systems to utilize and the creation of a machine that allowed fine control of the gap, further experiments were undertaken to judge the ability to control the long range ordering of the created pillars.

5.5 REFERENCES

1. Dickey, M. D.; Collister, E.; Raines, A.; Tsiartas, P.; Holcombe, T.; Sreenivasan, S. V.; Bonnecaze, R. T.; Willson, C. G., Photocurable Pillar Arrays Formed via Electrohydrodynamic Instabilities. *Chemistry of Materials* **2006,** 18, (8), 2043-2049.

2. Dickey, M. D.; Willson, C. G., Kinetic parameters for step and flash imprint lithography photopolymerization. *AIChE Journal* **2006,** 52, (2), 777-784.

3. Decker, C. a. A. D. J., Kinetic approach of oxygen inhibition in ultraviolet- and laser-induced polymerizations. *Macromolecules* **1985,** 18, (6), 1241-1244.

4. Decker, C., The use of UV irradiation in polymerization. *Polymer International* **1998,** 45, (2), 133-141.

5. Decker, C., Kinetic study and new applications of UV radiation curing. *Macromolecular Rapid Communications* **2002,** 23, (18), 1067-1093.

6. Kim, E. K. Development and Study of Nano-Imprint and Electron Beam Lithography Materials for Semiconductor Devices. University of Texas, Austin, 2005.

7. Hoyle, C. E.; Lee, T. Y.; Roper, T., Thiol-enes: Chemistry of the past with promise for the future. *Journal of Polymer Science, Part A: Polymer Chemistry* **2004,** 42, (21), 5301-5338.

8. Jacobine, A. F., Thiol-ene photopolymers. *Radiat. Curing Polym. Sci. Technol.* **1993,** 3, 219-68.

9. Cramer, N. B.; Scott, J. P.; Bowman, C. N., Photopolymerizations of Thiol-Ene Polymers without Photoinitiators. *Macromolecules* **2002,** 35, (14), 5361-5365.

10. Decker, C.; Bianchi, C.; Morel, F.; Jonsson, S.; Hoyle, C., Mechanistic study of the light-induced copolymerization of maleimide/vinyl ether systems. *Macromolecular Chemistry and Physics* **2000,** 201, (13), 1493-1503.

11. Clark, S. C.; Jonsson, S.; Hoyle, C. E., Maleimides with carbonate and urethane groups as photoinitiators for acrylate polymerization. *Polymer Preprints (American Chemical Society, Division of Polymer Chemistry)* **1997,** 38, (2), 363-364.

12. Hoyle, C. E.; Clark, S. C.; Jonsson, S.; Shimose, M., Photopolymerization using maleimides as photoinitiators. *Polymer* **1997,** 38, (22), 5695-5697.

13. Decker, C.; Morel, F.; Jonsson, S.; Clark, S.; Hoyle, C., Light-induced polymerization of photoinitiator-free vinyl ether/maleimide systems. *Macromolecular Chemistry and Physics* **1999,** 200, (5), 1005-1013.

14. Jonsson, E. S. Y., Danning; Viswanathan, Kalyanaraman; Lindgren, Karin; Holye, Charles, Photoinduced Free Radical Ring Opening Copolymerization in Acceptor/Donor Systems. *RadTech Europe 02:[Conference Proceedings], April Session* **2002**.

15. Hoyle, C. E.; Viswanathan, K.; Clark, S. C.; Miller, C. W.; Nguyen, C.; Joensson, S.; Shao, L., Sensitized Polymerization of an Acrylate/Maleimide System. *Macromolecules* **1999,** 32, (8), 2793-2795.

16. Jonsson, S.; Viswanathan, K.; Hoyle, C. E.; Clark, S. C.; Miller, C.; Morel, F.; Decker, C., Recent advances in photoinduced donor/acceptor copolymerization. *Nuclear Instruments & Methods in Physics Research, Section B: Beam Interactions with Materials and Atoms* **1999,** 151, (1-4), 268-278.

17. Yang, D.; Viswanathan, K.; Hoyle, C. E.; Jonsson, S.; Hasselgren, C., Studies of initiation mechanism of maleimide/vinyl ether copolymerizations. *Experience the World of UV/EB, RadTech 2000: The Premier UV/EB Conference & Exhibition, Technical Conference Proceedings, Baltimore, MD, United States, Apr. 9-12, 2000* **2000**, 221-230.

18. Decker, C., et la, Mechanistic study of the light-induced copolymerization of maleimide/vinyl ether systems. *Macromolecular Chemistry and Physics* **2000,** 201, (13), 1493-1503.

19. Dickey, M. D.; Burns, R. L.; Kim, E. K.; Johnson, S. C.; Stacey, N. A.; Willson, C. G., Study of the kinetics of Step and Flash imprint lithography photopolymerization. *AIChE Journal* **2005,** 51, (9), 2547-2555.

20. Raines, A. Nano-Scale Large Area Gap Control for High Throughput Electrically Induced Micro-Patterning. University of Texas, Austin, 2007.

21. Dickey, M. D.; Raines, A.; Collister, E.; Bonnecaze, R. T.; Sreenivasan, S. V.; Willson, C. G., High-aspect ratio polymeric pillar arrays formed via electrohydrodynamic patterning. *Journal of Materials Science* **2008,** 43, (1), 117-122.

Chapter 6

I decided to explore control of long range order in the photocurable systems by using patterned top electrodes. The focus was both on isolated features and arrayed features. My experiments in this area are described in this chapter.

6.1 Inducing Order in Pillar Arrays

During initial experiments, it was observed that the pillars often tended to form first at the edge of the electrode and in a straight line. The formation of the adjunct rows of pillars tended to somewhat follow the edge pillars but lose register with distance from the edge. The ordering of these pillars was different from that of those that initiated in the middle of the active area. It was also observed that pillars form and order differently if there are scratches on the electrode's metal, see Figure 6.1. These observations lead to idea that in order to control the pillars' ordering and growth that a pattern electrode should be used.

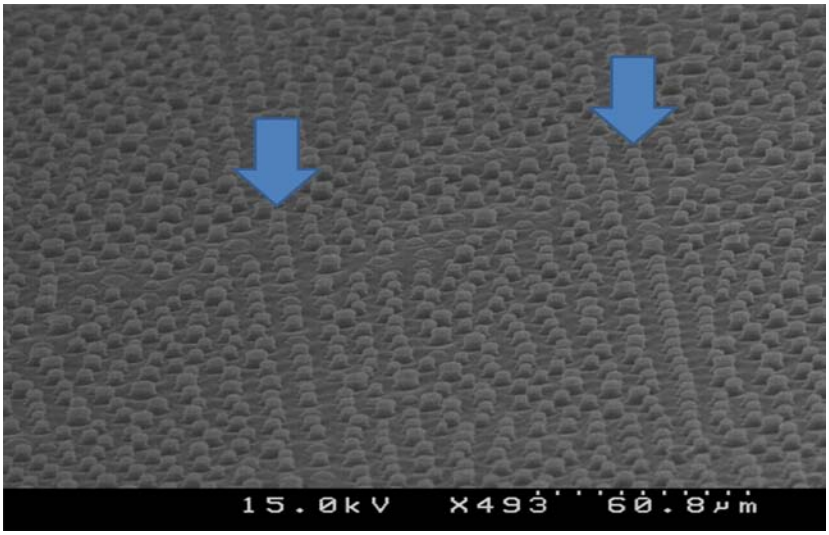

Figure 6.1. A SEM image of a pillar array formed when scratches were present in the metal layer on the top electrode causing the ordering of the resultant features to change. The arrows highlight the two rows that formed in the immediate vicinity of the scratches.

Inducing order in the formation of the pillars created via electrostatic lithography involves the creation of templates with various patterns located in the active area on the mesa. The masks used to create the patterns on the mesa were created via electron beam lithography.

Models have predicted that order is only possible within distances 2-3 times the fastest growing wavelength from the nucleation point when the fill factor is greater than three.[1] It has been observed that hexagonal closed space packing occurs when either a flat upper electrode/template is used or when patterned electrode/template of triangles are used. The use of square protrusions, yields square packing. Models have predicted that arrays of triangles or squares could induce areas of long range order, possibly on the order of centimeters.[2]

When using patterned templates, the pillars first form in the corners of shaped protrusions and then outline the outer most portion of the protrusion before appearing in the next concentric row. In order to achieve uniform diameters of the formed pillars, the length of the patterned

protrusions must be an integer multiple of the maximum characteristic wavelength and the gap must be constant. If that is not the case, in forming the next concentric row, the pillar diameter can decrease in order to keep the proper packing. This ability to frustrate the pillar diameter allows flexibility in patterning.

6.2 TEMPLATE CREATION

The templates were created from a 6025 quartz mask blank. One plate yields four templates. The mask blanks come from the vendor with a coating of 25 nm of chromium under a layer of photoresist, normally positive tone. The mesa was first created by patterning the photoresist on the blank. This was done via UV exposure through a quartz mask that has patterned chromium square of proper size in the center of the mask. After exposure the plate was baked and then developed in the appropriate developer. Once this was done the blank had areas where the chromium was exposed. A chromium etch was then performed using Transcene's chromium etchant. This exposed the quartz areas beneath the exposed chromium. The plate was then recoated with a protective polymer layer and diced into four 65 mm x 65 mm squares and two opposite edges were rounded to provide an area to mount a wire for electrical contact to the templates surface. The protective polymer was stripped and the templates were cleaned in a piranha bath, (3:1 V/V H_2SO_4:H_2O_2). Next the remaining chromium square in the center of the template, was inspected for holes and then mesa etch was performed by immersing the template into a buffered oxide etch (BOE) solution for the desired period of time. In order to reduce the electrical force, mesa heights were usually chosen to be greater than four microns. The mesa heights were checked via profilometery. A brief cartoon of this process is shown in Figure 6.2.

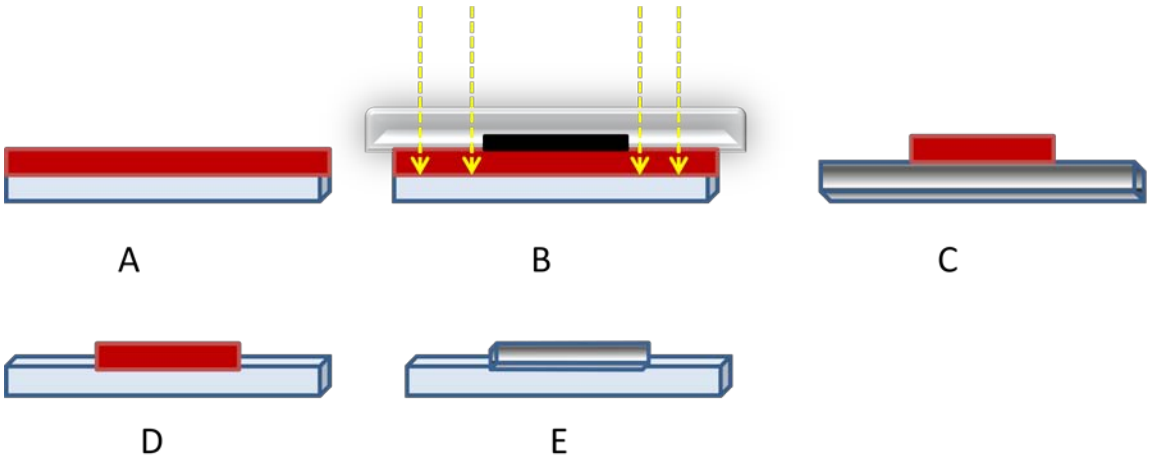

Figure 6.2. The template mesa creation process. (A) The blank quartz template consists of film stack of photoresist on top of chromium. (B) Positive tone mask is pictured, creating the latent image of the mesa in the photoresist. (C) After development, the chromium layer is exposed and only the mesa area is protected by resist. (D) The exposed chromium is then etched to reveal the underlying quartz. (E) The mesa image is etched into the template via a buffered oxide etch and then photoresist is finally stripped from the mesa.

To create a patterned mesa, the template was first coated with an adhesion promoter, like Silicon Resources' AP 410. Then the appropriate tone photoresist for the desired mask image was spin coated onto the template and baked to remove the excess solvent. Due to the thickness of the quartz template, the bake time was at least an hour. Once the template had cooled it was patterned. For the size features reported in this document, contact lithography was utilized. Thus the mask, patterned side down, was brought into contact with the template with the pattern on the mask aligned with the chromium coated etched mesa on the template and then exposed to UV light. If the resist requires, the template was then baked. Next, the image was developed using the appropriate developer. In order to preserve the pattern integrity, the chromium etch was accomplished via reactive ion etch in a Trion etcher. If the desired features were less than a

micron in depth the quartz etch was also conducted in the Trion etcher, if the etch required was deeper the features were transferred into the mesa via BOE due to time constraints. The feature heights were checked via profilometry. The next step in the process was rendering the templates surface electrically active.

6.3 TEMPLATE'S CONDUCTIVE LAYER

The conductive layer that was applied to the template's surface had to be transparent to the wavelength of UV light that initiates the photocurable system being used. For coatings like chromium the transparency has a large dependence on coating thickness, thus films below eighteen nanometers were employed. Aluminum coating allowed for thicknesses of forty nanometers. Indium tin oxide, ITO, allows very thick films on the order of hundreds nanometers or more with a high degree of transmission if the appropriate annealing procedures are followed.

6.3.1 Chromium

Chromium was deposited both by electron beam (e-beam) evaporation, as well as thermal evaporation. The thickness of the films was tracked via quartz crystal microbalances in each of the machines utilized and double checked via profilometery. Typical film thickness was fifteen nanometers. With such thin films of chromium over mesa's with heights between fourteen to eight microns, the mesa would often lose connectivity to with the template surface after tens of experiments. This was undesirable and other conductive layers were tested.

6.3.2 Aluminum

Aluminum was deposited via e-beam evaporation with a typical thickness of forty nanometers. Unfortunately, while the transmission of light was sufficient to cure the applicable photocurable systems, the quartz/Al interface was quite reflective and extraneous signals where a constant problem using white light interferometery sensing in the Hybrid Active Gap Tool. The inability to align the template efficiently with the Aluminum layer led to the need for a different conductive layer to be found.

6.3.3 Indium Tin Oxide (ITO)

Indium tin oxide was deposited via e-beam evaporation with a typical film thickness of one hundred microns. The film as deposited has a grayish purple hue. In order for the film to become more transparent it had to be annealed. Research has shown that in order to achieve high transparency in ITO films it is best to anneal at temperatures around 300^{o}C in the presence of oxygen.[3] Thus the ITO films were annealed at 325^{o}C overnight in ambient atmosphere. The ITO films allowed for the highest transmission of light and were the easiest to align in the hybrid active gap tool. Unfortunately, the ITO layer was also the hardest to protect.

6.4 Interfacial Adhesion at the Template

All of the experimental photocurable systems adhered to the conductive oxide films on the template. It was also found that the photocurable systems containing vinyl ethers could strip the conductive layers from the template. This was evident by residual pillar images in the conductive layer which could be seen in the optical microscope but were not capable of being measured via profilometry, see Figure 6.3.

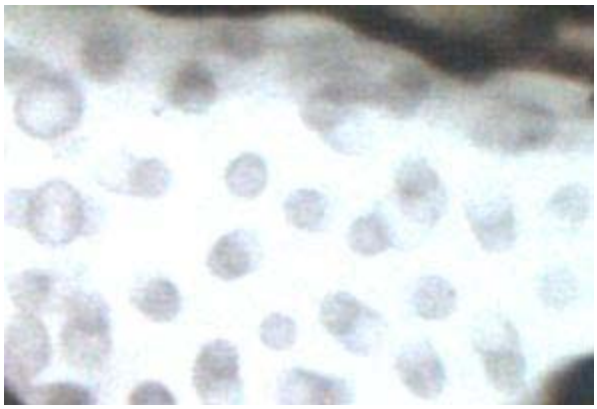

Figure 6.3. Residual pillar images left in aluminum coating after an experiment.

In order to reduce the pillars' adhesion to the template, a fluorinated self-assembled monolayer (FSAM) was applied to the conductive oxide film. The FSAM provides a low surface energy and hence a low adhesion force. This was done by first exposing the template to an oxygen plasma for cleaning and then immersing the template in a solution of toluene with a small amount of a fluorinated chlorosilane for thirty minutes. The reaction of the chlorosilane with the hydroxdyl groups is proposed to proceed with the chlorosilane reacting first with absorbed water creating hydrochloric acid (HCl) and silanol intermediates. The silanol intermediates then go on to undergo condensation reactions with the hydroxyl groups on the quartz to forming a covalent linkage to the quartz.[4] The success of the treatment is apparent by the change in contact angle with water from wetting to approximately 110^{o}. While the treatment works well for SiO_2 surfaces it does not work well for chromium or aluminum. This method also had to be modified for the ITO surface due to the fact that hydrochloric acid, a byproduct of the reaction, etches ITO.

In order to modify the conductive surface to allow better FSAM adhesion a SiO_2 layer was deposited over the conductive layer. The layer was deposited via e-beam evaporation typically to a thickness of one hundred nanometers. This layer provided a better surface for the

FSAM layer to react with although there where instances of failure of the conductive layer/ SiO_2 interface. Unfortunately, the SiO_2 layer was porous and did not completely protect the ITO from the HCl formed. An alternative method was used to treat the ITO conductive layer.

The alternative method used to treat the ITO surface involved the addition of base to the toluene and fluorinated chlorosilane solution. The base, typically pyridine, was added in a one to one ratio with the fluorinated chlorosilane. This helped to stop the stripping of the ITO from the template but the resulting contact angle with water tended to be lower.

It was observed over multiple experiments that the FSAM tended to fail. Since the alignment process of the template is a timely undertaking, a method was sought to protect the FSAM layer. FSAM degradation has been attributed to such things as attack by free radicals,[5-7] UV degradation,[5] mechanical interlocking,[8, 9] and chain scission.[10] Thus if UV degradation was not the main cause of FSAM failure, it was proposed to use a fluorinated surfactant to protect the FSAM, since it is known that fluorinated surfactants migrate towards FSAM treated surfaces.[9]

6.4.1 Surfactant Effects

The requirements for the surfactant are that it is soluble in the photocurable systems and that it is nonvolatile, so that the film does not change over the course of the experiment. The fluorosurfactant chosen was 3M's Novec™ FC-4430. FC-4430 is a non-ionic polymeric fluorosurfactant soluble in both organic and aqueous solutions. It is capable of reducing the static surface tension of distilled water from 78 dynes/cm to 23 dynes/cm with 0.1% weight loading.[11] The surfactant was added to the photocurable formulations in varying concentrations.

It was observed that the surfactant did not in fact protect the FSAM layer regardless of concentration, the contact angle with water degraded after several experiments and experiments

began to fail depending on the system used after four or five experiments. This result of FSAM degradation was also collaborated by similar research performed on FSAM layers with S-FIL acrylate formulations with x-ray photoemission spectroscopy (XPS) studies[12] and with XPS studies on methacrylate based systems as well as vinyl ether systems.[7] While the fluorosurfactant did not protect the FSAM layer it did have a beneficial effect of reducing the surface energy of the photocurable systems which is discussed in section 6.5.

6.5 Interfical Tension at the Substrate

In order to stop the pillars from releasing from the substrate and fouling the template an adhesion promoter was coated onto substrates. The most successful adhesion promoter tested was Silicon Resources' AP 410 since it did not interact with the photcurable systems. The AP 410 also acted to stabilze the photocurable systems when films below 300 nm were to be utilized. The maleimide- acrylate system would not form stable films and would begin dewetting immediately after spin coating films below 300 nm unless AP 410 was applied to the substrate.

The adhesion layer was applied by pipetting the liquid to the substrate and spin coating at 3500 rpm. The film was then baked for at least 30 seconds at 90 ^{o}C and then cooled.

6.6 Experimental Procedure

The patterns created on the mesa were designed for thin films 300 nm and less and for gaps of one micron or below for best packing results. The substrate was first coated with adhesion promoter. Then the template and substrate were first loaded into the machine and the leveling procedure was carried out, see Appendix B. The substrate was then taken out of the machine and a 200 nm film was spin cast on it. The substrate was then reloaded and both the substrate and the template were connected to a voltage source. The planarity was then checked and the template was then slowly moved down to the necessary gap. Once the gap was stable, the potential was applied. The fourth sensor was then moved in order to allow the light guide's

to be placement in the window to the back of the template. Once the desired time has passed a Novacure mercury lamp was used to expose the pillars for sixty seconds. Once cured, the potential was shut off and the template and the substrate were separated.

6.7 Surfactant Effects

The addition of 3M Novec™ 4430 was initially intended to protect the FSAM layer but the fluorsurfactant also reduced the surface energy of the system. The reduction in surface energy meant that for the same gap, film thickness, and applied voltage the system with the surfactant produced smaller and more closely packed pillars, see Figure 6.4. Having more compact pillars can change the wetting ability of fluids on the patterned area.

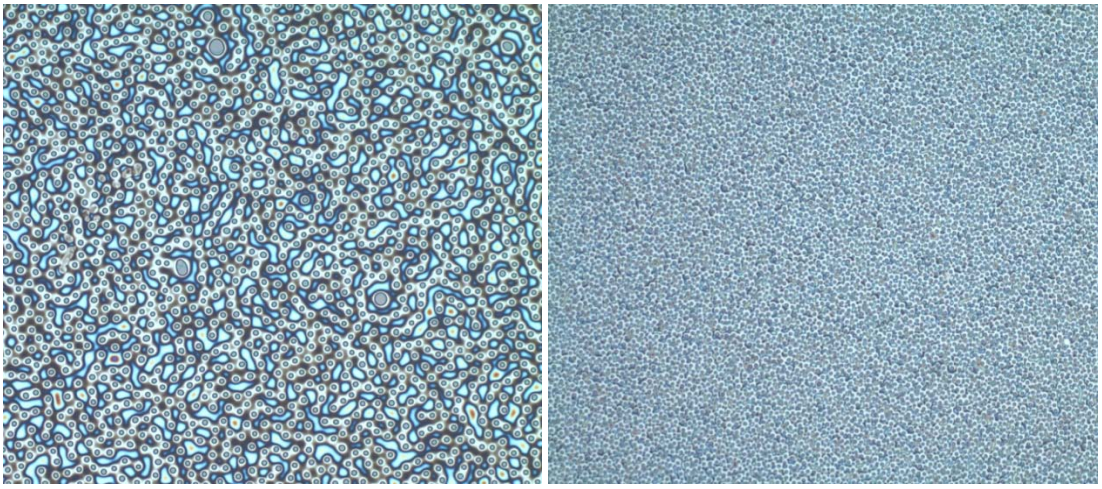

Figure 6.4. A comparison of the effect of fluorosurfactant FC-4430 on the pillars formed in the QB-TA system. The picture from optical microscope on the left shows the pillars form with 0.6 wt% FC-4430 added.

6.8 Isolated Features

Isolated features were used to study pattern frustration as well as the maximum length for the induction of ordering. The easiest pattern to use to guide pillar formation are squares. Other features tested were triangles, pentagons, and hexagons as well as some more random features. Some typical results for the features can be seen in Figure 6.5. As seen in Figure 6.6, pillars begin to grow at the edges of the square and then if space provides they fill in the outline of the square, before moving into the next inner most row.

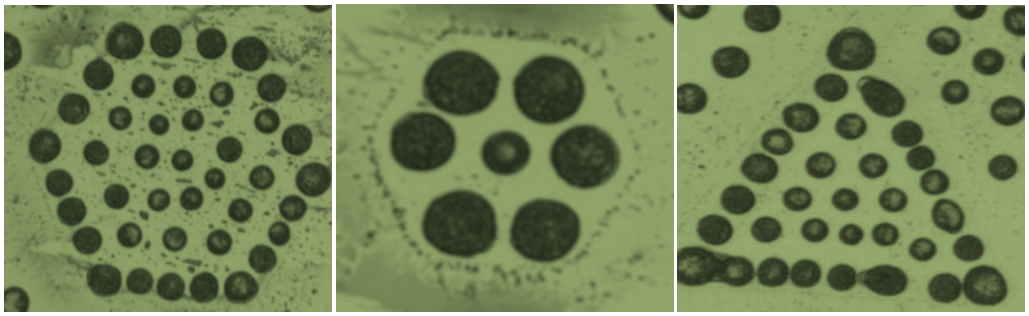

Figure 6.5. Left: Pillars formed under a template patterned with a hexagon. Middle: Pillars formed under a template patterned with a pentagon. Left: Pillars formed under a template patterned with a triangle.

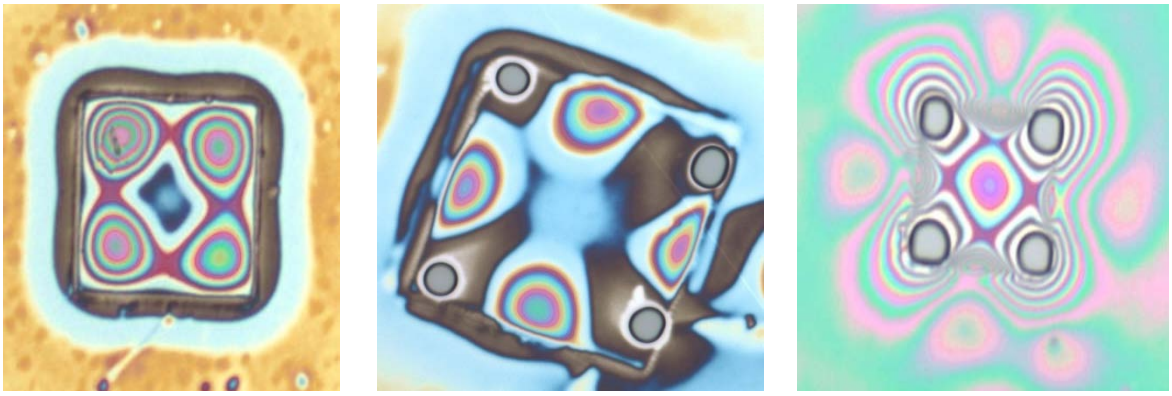

Figure 6.6. Images of the initial stages of pillar formation captured via optical microscope. Left: Pillars begin growing into the four corners of a square. Middle: Pillar captured after the corners have grown in and in the process of growing into a complete the outline of the square. Right: Pillars have grown into the corners of the square and next begin growing in the center of the square.

The images in Figure 6.6 also highlight the size of the area that the pillars draw material from. In each image, it is evident that an area of several microns in size has had the film thinned or taken away. This can impact the ability of pillars to be formed in near-by areas. This is shown in Figure 6.7, the CAD image of the features is given on the left the resulting pillars on the left. The features were designed to see how the packing is affected by the non-ideal size features, i.e. features that are not $2\lambda+D$. In the image on the right, in the first few features in each row it is evident that there was competition for material to create pillars out of.

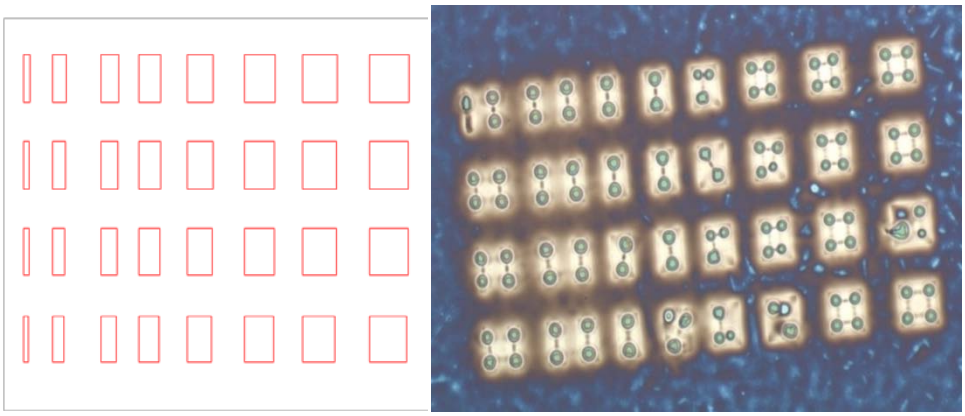

Figure 6.7. Left: CAD image of the features written to a template to test the ability to frustrate the packing of the formed pillars. Right: The resulting pillars from the template in which it is evident that the pillars in the first few features in each row competed for available film to create pillars.

This creates a problem for creating pillars from features that are in close proximity. One way to correct the problem is to use thicker films but then if the fill factor becomes less than three the pillars will coalesce. On these cases the current models fail to predict the behavior of the forming pillars.

The longest range ordering found in isolate features was three orders, although it was not perfect. As seen in Figure 6.8, this ordering was found in both an isolated hexagon and a square. These resulted from a 200 nm film of the thiol-ene system with the FC-4430 surfactant added. The gap was meant to be one micron but was instead 900 nm again alignment was an issue and the gap over the entire active area varied by 300 nm down to 600 nm. A potential of 40 V was applied for five minutes.

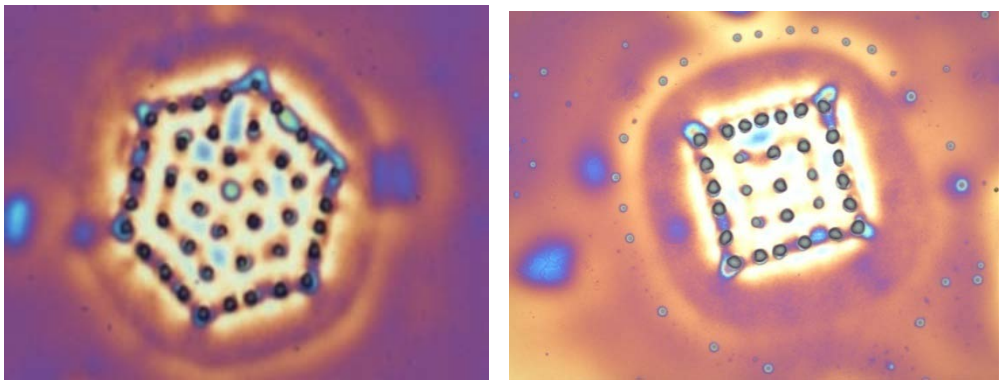

Figure 6.8. The highest ordering of an isolated feature was found to be three as evident in both the hexagon and the square.

6.9 Arrays of Features

In order to create pillar arrays with long range order, the templates need to be created with arrays of protruding patterns on them. The arrays chosen to be tested were arrays of squares. The purpose of the experiments was to see how many pillars per square were possible as well as how well the ordering proceeded.

The first template designed for such purposes was created before the limits of the Hybrid active gap tool were known. It was designed from gaps of 300 nm which the machine is unable to control. The template was designed with an array of 21x21 47 micron squares that are spaced two micron apart and etched to a depth of 220 nm. An initial result is showed in Figure 6.9. This initial result highlighted some of the issues with using white light interfermometry to judge the gap distance and well as the film thickness. The sensors for the experiment read that the gap was 1.5 microns but the SEM results showed the gap was actually 1.1 microns. A 420 nm film of the maleimide system was used and an AC voltage if 6.5 volts was applied for 1.5 minutes. Some of the pillars have coalesced due to the fact that the fill factor was 2.6. This experiment also shows that over long time periods the material creating the pillars will also climb up the edge of the pattern, hence the ability to see the area between the squares.

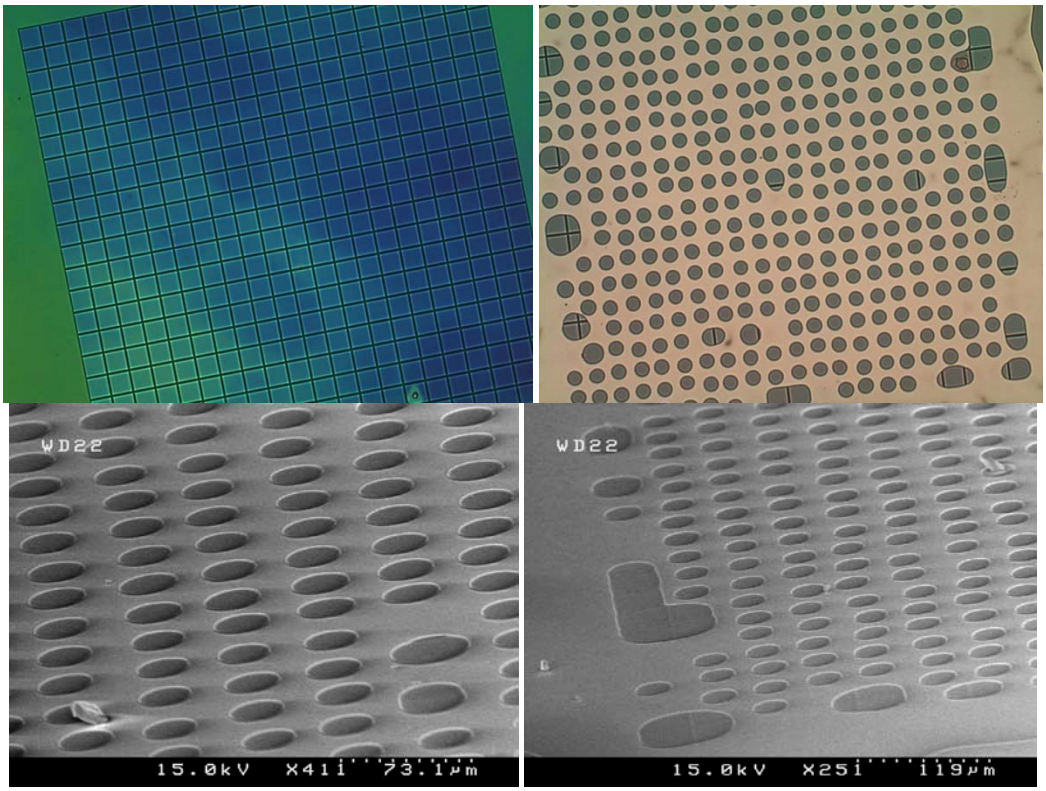

Figure 6.9. Top left: Optical microscope image of the protruded array of 47 microns squares on the template. Top right: Optimal microscope image of the resultant pillars formed, one per square with coalescence evident. Bottom left: SEM image of the pillars formed under each square on the template. Bottom right: SEM image of the pillars formed under each square with some of them having begun to coalesce.

The same template was used later with a 200 nm film from the thiol-ene system with the 3M Novec™ 4430 surfactant added. This experiment was conducted with a gap of one micron. A potential of 40 volts was applied for one minute. The resulting pillar array can be seen in Figure 6.10. Unfortunately, the ordering is not perfect. This is partially due to competition for material; this is evident in the dark areas outlining each square where the material has been depleted. This is also due to the fact that the template was not aligned correctly the gap varied 300 nm across the entire active area.

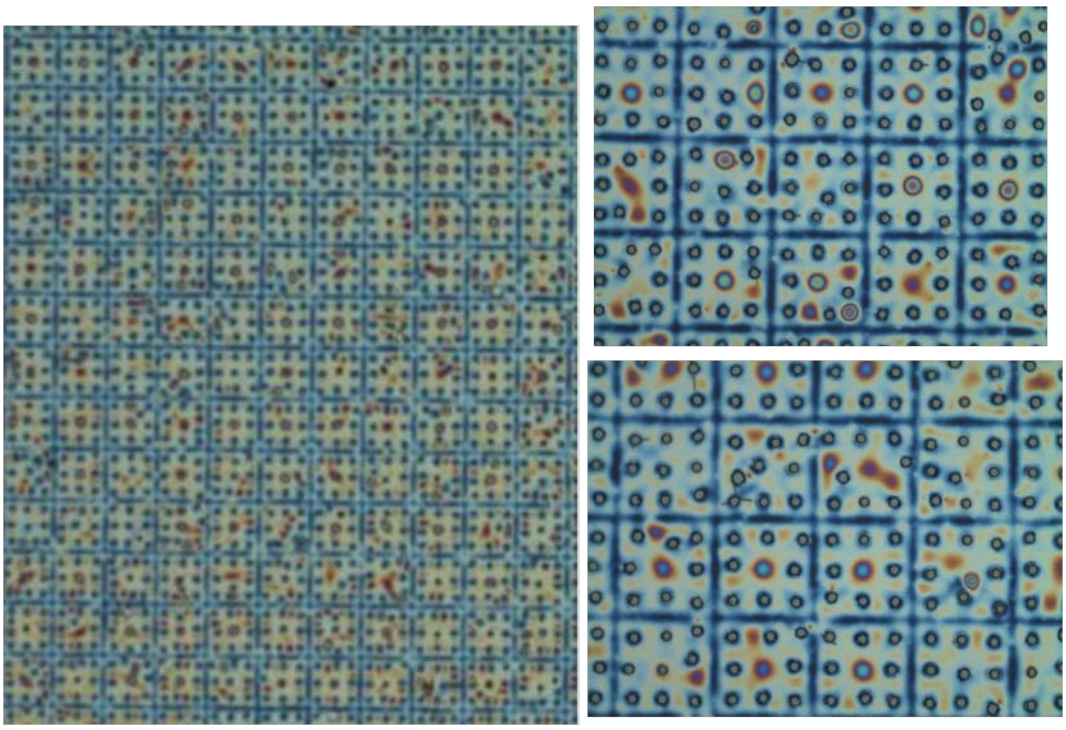

Figure 6.10. Left: Optical microscope image, 10x, of the resulting pillars from the Thiol-ene system with surfactant using a template with a 21x21 array of 47 micron squares. Right: Optical microscope images, 50x, of the some sections of the resulting pillars.

Another template was created to try to induce more pillars to form per square in the array. The squares in the array this time were 109 microns. The template was able to create more pillars per square but the ordering was worse, see Figure 6.11. In this experiment, it is apparent that the material between the square has been exhausted. The experimental conditions consisted of a 200 nm film of the thiol-ene system with the FC-4430 surfactant added. The gap was meant to be one micron but was instead 900 nm again alignment was an issue and the gap over the entire active area varied by 300 nm down to 600 nm. A potential of 40 V was applied for five minutes.

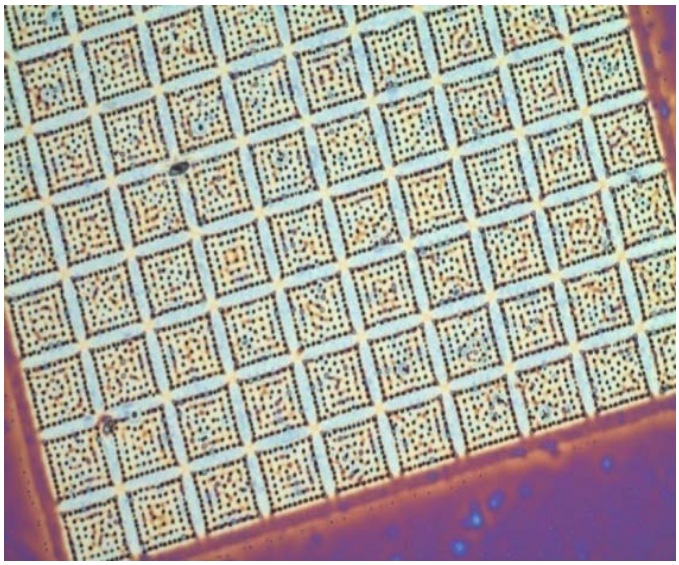

Figure 6.11. Optical microscope image of pillars that formed under a 109 micron square array using a 200 nm film of the thiol-ene system with FC-4330 surfactant added and a 900 nm gap with a potential of 40 V. Poor ordering is evident.

6.10 Pillar Selectivity

Having pillars form just under the patterned features is a result of the gap size, the potential applied, and height of the features, to a smaller extent the time scale of the experiment can affect it as well. It was found that in general for an 800 nm gap and a potential of 40 V the features need to be 2 microns in height off the mesa for best pillar selectivity.

6.11 Discussion

The two most problematic portions of these experiments are getting the pillars to release from the template after multiple experiments and calibrating the mesa height on the template in order to get good planarity with the film. The main sticking point is the template calibration since if it were easier to calibrate the template then it wouldn't be as bothersome to remove and retreat the template for better release. The calibration can take up to 2 hours and then when taking the wafer out to spin coat on the thin film and putting it back in sometimes the calibration is lost. One source of error is that the wafer is not flat due to the fact that it is held in place by a vacuum chuck. The vacuum chuck causes the wafer to bow and it will bow on the millimeter

scale such that the active area is not level. Another cause of error is the distance the sensors are from the active area. It would be easier to planarize the active area if the sensors were all on the active area of at least in its immediate vicinity. Another source of error is the use of white light inferometery. The sensors are unable to read films below 300 nm accurately. One way to accomplish this may be to build spacers on the active area. This of course will cause difficulties when applying the conductive layer and it retracts from the benefits of being able to control the gap size. But if the spacers are well characterized it will provide both an absolute gap size as well as a known measurement to use to calibrate the sensors.

Since it was so difficult to planarize the template to the wafer and differences of up to 400 nm were found across the active area it is difficult to say what the true limit of the inducing ordering in the pillars formed under patterned features. Given that the arrays should have a much lower differences across their area it the 2-3λ seems accurate. The easiest way to design for inducing ordering is to design for creating pillars just at the corners of whichever patterned feature. Of course this detracts some of the gain from the process, but it is easier to ensure the success of the process and it reduces the need to manage the necessary material present.

In order to better control the pillar formation, more work needs to be done to understand the area of influence of each pillar formed. A better material balance will help reduce the competition for pillar material and more uniform pillars will be created. The reason why so many of the models fail is due to the thinning of the film over time.

6.12 CONCLUSIONS

The ability to induce order in the created pillar arrays was inhibited by the inability to planarize the template with the film. The ability to only get 2-3λ seems accurate due to the difficulties with the gap a very accurate and on the low end of the simulated limit in literature. Designing for isolated features is far easier than dealing with arrayed patterns. In order to more easily design experiments for arrayed features models should be adapted to follow the material balance of the film over time, since competition for materials between the patterns can occur.

6.13 REFERENCES

1. Verma, R.; Sharma, A.; Kargupta, K.; Bhaumik, J., Electric Field Induced Instability and Pattern Formation in Thin Liquid Films. *Langmuir* **2005,** 21, (8), 3710-3721.

2. Wu, N.; Pease, L. F., III; Russel, W. B., Electric-Field-Induced Patterns In Thin Polymer Films: Weakly Nonlinear and Fully Nonlinear Evolution. *Langmuir* **2005,** 21, (26), 12290-12302.

3. Wang, R. X. B., C. D. ; Fung, S. ; Djurisic, A. B. ; Ling, C. C. ; Kwong, C. ; Li, S., Influence of annealing temperature and environment on the properties of indium tin oxide thin films. *Journal of Physics D: Applied Physics* **2005,** 38, 2000-2005.

4. Wu, K. Interface study for template release in step and flash imprint lithography. University of Texas, Austin, 2006.

5. Tasker, S., Chambers, R. D., and Badyal, J. P. S., Surface defluorination of PTFE by sodium atoms. *The Journal of Physical Chemistry* **1994,** 98, (47), 12442-12446.

6. Garidel, S., Zelsmann, M., Chaix, N., Voisin, P., Boussy, J., Beaurain, A., and Pelissier, B., Improved release stragety for UV nanoimprint lithography. *Journal of Vacuum Science & Technology, B: Microelectronics and Nanometer Structures* **2007,** 25, (6), 2430-2434.

7. Houle, F. A.; Rettner, C. T.; Miller, D. C.; Sooriyakumaran, R., Antiadhesion considerations for UV nanoimprint lithography. *Applied Physics Letters* **2007,** 90, 213103.

8. Bailey, T.; Choi, B. J.; Colburn, M.; Meissl, M.; Shaya, S.; Ekerdt, J. G.; Sreenivasan, S. V.; Willson, C. G., Step and flash imprint lithography: Template surface treatment and defect analysis. *Journal of Vacuum Science & Technology, B: Microelectronics and Nanometer Structures* **2000,** 18, (6), 3572-3577.

9. Wu, K.; Wang, X.; Kim, E. K.; Willson, C. G.; Ekerdt, J., Experimental and theoretical investagation on the surfactant segregation in imprint lithography. *Langmuir* **2007,** 23, (3), 1166-1170.

10. Tada, Y.; Yoshida, H.; Miyauchi, A., Analysis on the deterioration mechanism of the release layer in nanoimprint process. *Journal of Photopolymer Science and Technology* **2007,** 20, (4), 545-548.

11. 3M Novec(TM) Fluorosurfactant FC-4430. (7/23/2008)

12. Lin, M. Simulation and Design of Planarizing Materials and Interfacial Adhesion Studies for Step and Flash Imprint Lithography. University of Texas, Austin, 2008.

Chapter 7

7.1 Future Work Mesoscale code

7.1.1 Capturing the effects of oxygen

In order to more accurately capture the polymerization conditions the effects of the oxygen in the system should be added to the simulation. Since oxygen quenches the free radical polymerization the overall polymer conversion may be lowered. Previous models have shown that the residual diffused oxygen within the etch barrier is consumed within the first few seconds of the reaction but at perimeter of the template the polymer is subject to the continual presence of ambient oxygen and it can penetrate into the film up to 20 microns at the chosen system conditions.[1]

In order to incorporate this behavior into the simulation, it will be necessary to relate the monte carlo reaction time to the diffusion rate of the oxygen so that a diffusion probability can be defined. The population routine will need to be adjusted to allow the presence of oxygen at the perimeter of the template being simulated. The polymerization routine will need to be adapted to allow for the diffusion of oxygen in the film and also the quenching of oxygen with radicals will need to be added.

7.1.2 Taking Advantage of Parallel Computing

The easiest portion of the mesoscale code to run in parallel is the lattice population routine. The features to be simulated can be sectioned into blocks and each block may be populated individually. Once populated, a global population count can be found by having the processors report back their species count back to the main processor. This will reduce computation time on larger features.

The other routine that could benefit from parallel computing is the polymerization routine. This will require more planning than the population routine due to the fact that there

will be interaction between the blocks. As before one processor may be assigned per block and the routine will run as usual until a species that is on the edge of the block is chosen. Then information will be required from the neighboring block and in order not to corrupt the lattice by having both the block and the neighboring block trying to react the same species the neighboring block's processor will be paused. One way to implement the routine is to create ghost cells to pad an extra layer around each block that contains the cells of the adjacent blocks that will interact with the block (Figure 7.1). When any changes are made in the ghost cell area, the adjacent block is paused and an update is performed to the ghost cells of both blocks as well as the blocks themselves. In order to successful implement this routine, it is necessary to identify the neighbors of each block. The processor savings of this routine will depend on the size of the blocks since it will necessary to pause the adjunct block's processor when changes are being made in the ghost cell area.

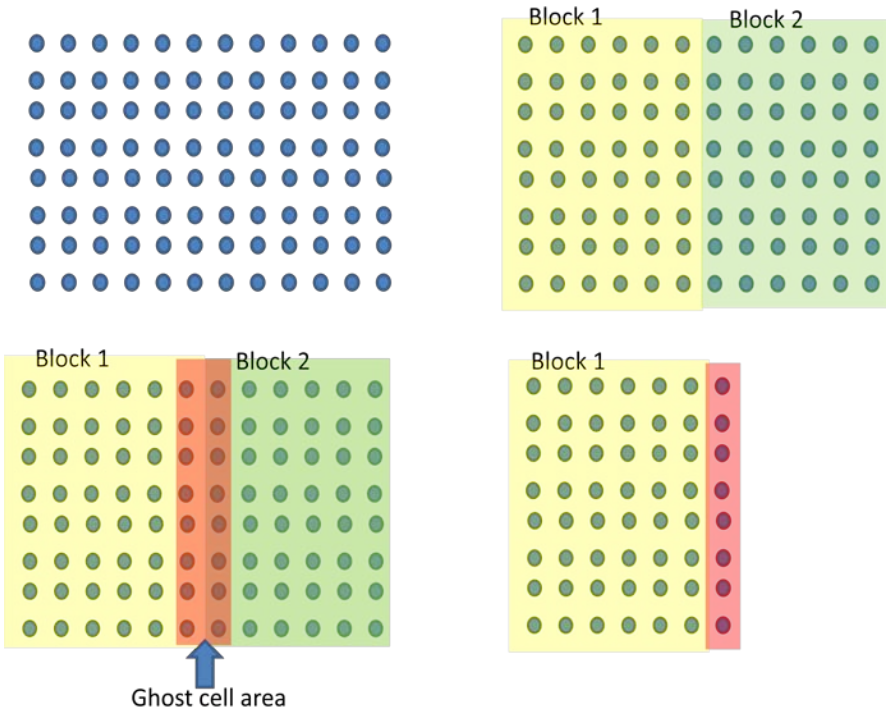

Figure 7.1. An example of a method to utilize parallel computing with the polymerization routine using ghost cells. The feature in the top left is split into two blocks each assigned to a specific processor. Since the species at the edge of each block can react with one another it is important for each block to have accurate knowledge of the cells in the neighboring block. In order to do this a ghost cell area at the shared edge of the blocks is created, so that the each processor actually the block contains an extra area of cells from the each neighboring block, bottom right. If a species is chosen in the cells that neighbors the ghost cells the neighboring processor is stopped to avoid both trying to change the same cells. Once there is a change in the ghost cell region an update is made to the appropriate neighbor to update the changed cells.

7.2 Improving the Inverse Problem

The inverse problem needs to be adjusted so that the mixed potential and the FENE potential case can be calibrated. The FENE potential case should be attempted first since the parameters are easiest to link to known physical data. Since algorithm currently fails in both cases the problem is most probably related to the use of the Lennard-Jones 6-12 potential. The first course of action would be to try to do a hand calculation for a small problem. The inverse problem will then need to be run on the SFIL etch barrier system.

7.3 Changes to the Multiscale Code

In order to simulate more processes in the SFIL process, the multiscale code can be adapted to simulate template release. In order to do this, potential models that allow for bond failure, such as the Morse potential, or creating a limit to the force on a bond before breaking will need to be found or created. A potential interaction between the template and the etch barrier will need to be defined and the parameters for the potential will need to be found. The continuum portion of the code may need to be changed to allow for plastic deformation. There will also need to be some mechanism for crack initiation added to the simulation.

7.4 Creation of Pillar Arrays Experiment Improvements

One of the main problems in the pillar experiments is keeping the template parallel to the film. This is due both to the issues with limits of the sensors as well as the inability to carefully calibrate the template ledges. One method that may help with both these problems is to construct spacers on the template. The spacers would act as an absolute measurement of distance for the gap created by the template and the wafer. The spacers should be designed to be the absolute minimum gap that will be attempted with template pattern, this way other gaps may still be attempted. During the deposition of the electrode metal on the template it will be necessary to mask off the spacers so that they do not have a conductive coating on them. By having better control of the gap across the entire active area it may be possible better induce order in the formed pillars.

Another problem in the pillar experiments is the destruction of the conductive layer on the template by the pillar materials due to the wearing off of the FSAM layer. One method to combat this problem is to find a flourpolymer that will adhere to the chosen conductive layer and can either be patterned to match the templates pattern or can uniformly coat the template's features. This flourpolymer must still be transparent to UV light.

7.5 Modeling the Creation of Pillar Arrays

In the current models of pillar formation, there is need of a model to help accurately monitor the changes in film thickness around the patterned features. That is a model that will help predict the spacing necessary between patterns on the template such that the competition for the material below the patterns is minimized. This will greatly help in the design of arrayed patterns. This can possibly be studied via experiments followed by atomic force microscope measurements.

7.6 REFERENCES

1. Dickey, M. Development of Photocurable Pillar Arrays Formed via Electrohydrodynamic Instabilities. University of Texas, Austin, 2006.

Appendices

Appendix A: Maleimide Synthesis

In searching for ideal materials to use in the pillars project some effort was expended in trying to synthesize maleimide derivatives. A short discussion on the more successful routes follows.

Maleimides feature a nitrogen containing five membered ring as well as two carbonyl groups and an unsaturated bond. Maleimides are reactive to light and radicals. Thus protecting the reactive unsaturated bond in the ring structure was necessary throughout the various reaction steps.

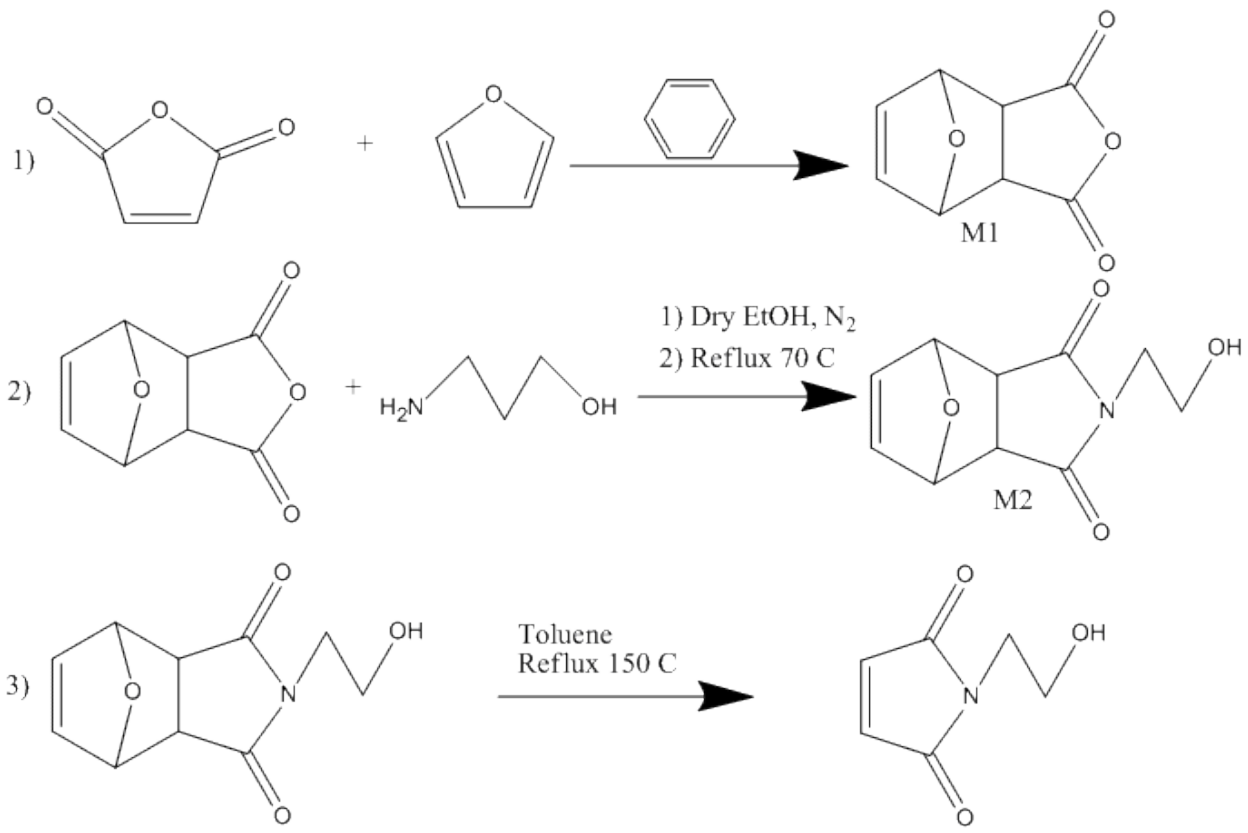

Figure A1. Synthesis route to hydroxyl-ethyl maleimide product.

The most successful route will be discussed with the product hydroxyethyl- maleimide, HEMI, as the end product in three separate steps (Figure A1.).

Step One: To 120 ml of benzene, 27.9g furan and 40.18 g maleic anhydride were added. It was stirred over night at room temperature then placed in the freezer for a day. The Diels-alder product is a white solid that crashes out of solution at 93% yield. The product is filtered and dried under high vacuum. H-NMR is shown in Figure A2.

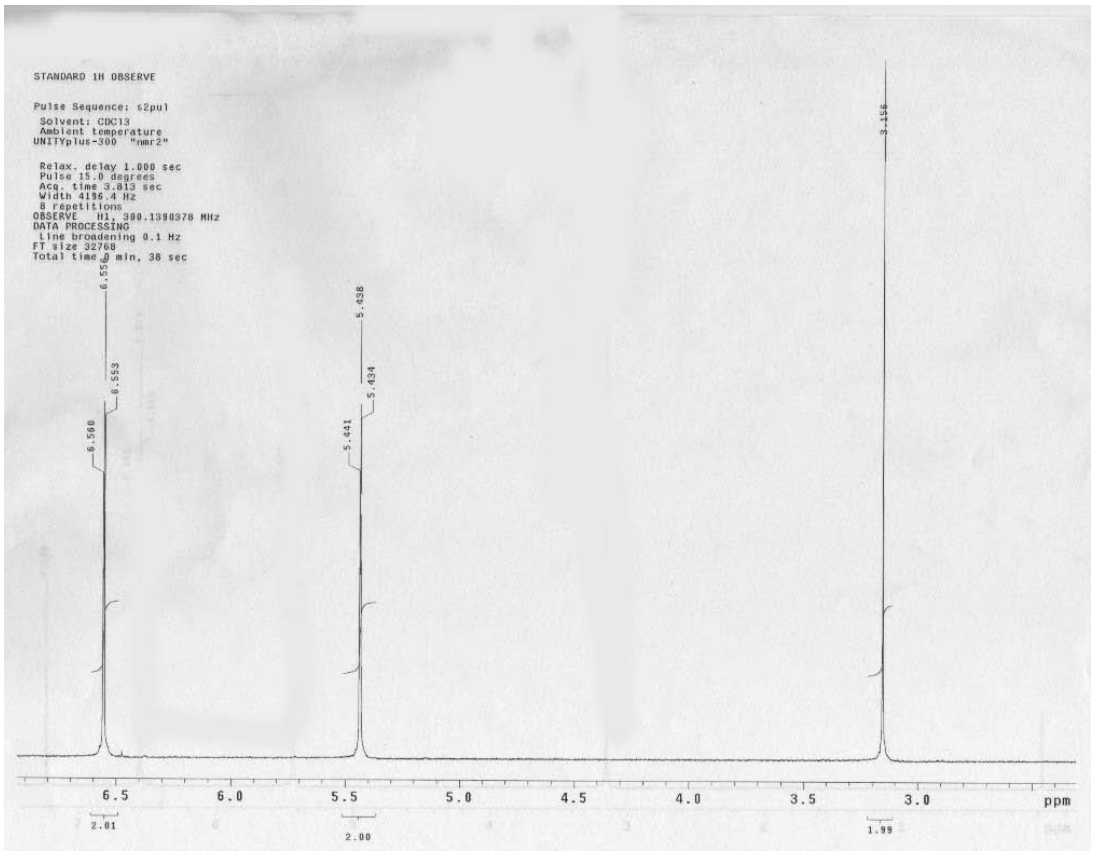

Figure A2. H-NMR of the maleic anhydride/furan Diels-alder product, M1, from step 1 of the synthesis shown in Figure A1.

Step two: 22.74g of M1 are stirred in 80 ml dry methanol for 10 min in a flask fitted with a condenser and under nitrogen. 9 ml of ethanol amine are added to through the condenser and then the solution is refluxed at 70 ^{o}C overnight. 16g product, M2, recovered after the solution was left to crystallize in the freezer overnight. H-NMR shown in Figure A3.

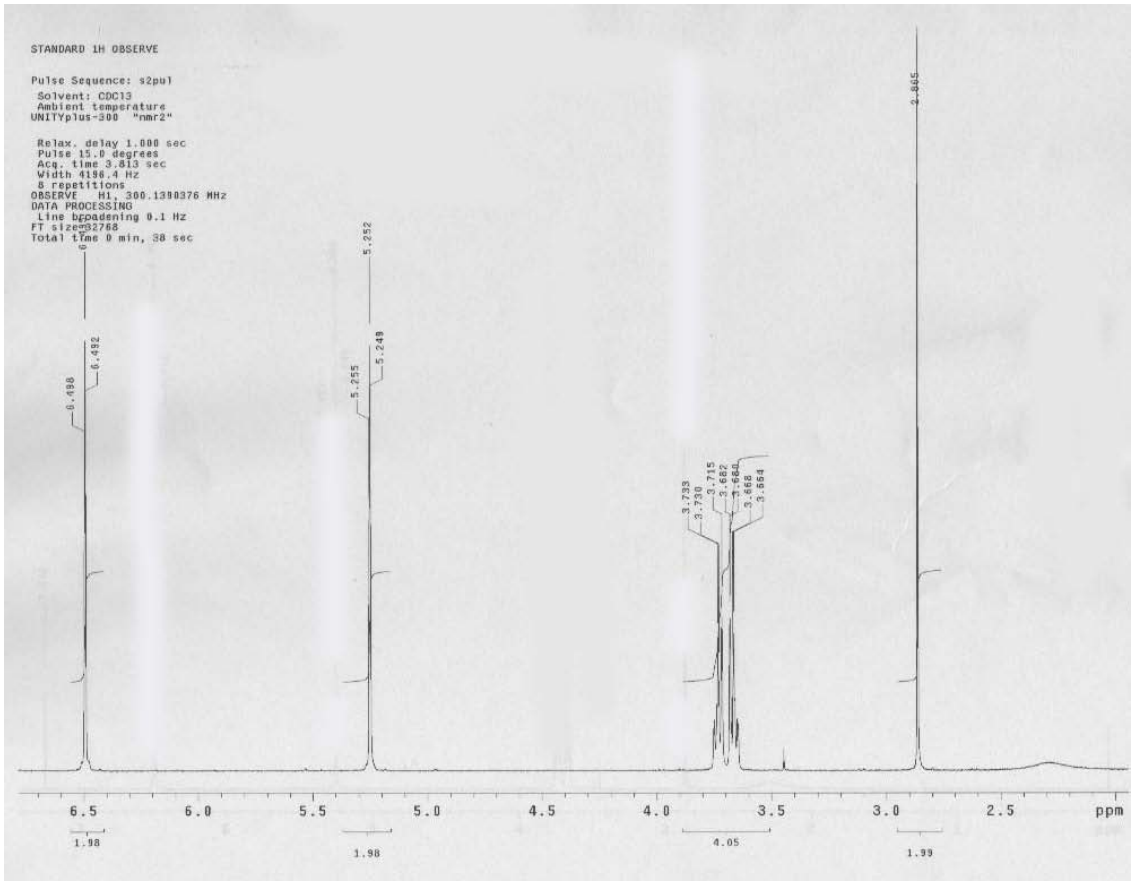

Figure A3. H-NMR of the ethanol amine product of step two of the synthesis in Figure A1.

Step 3: The solid HEMI product is achieved in 92% yield after refluxing the adduct in toluene overnight at 150 ^{o}C followed by hot filtering and allow the product to crystallize out of solution.

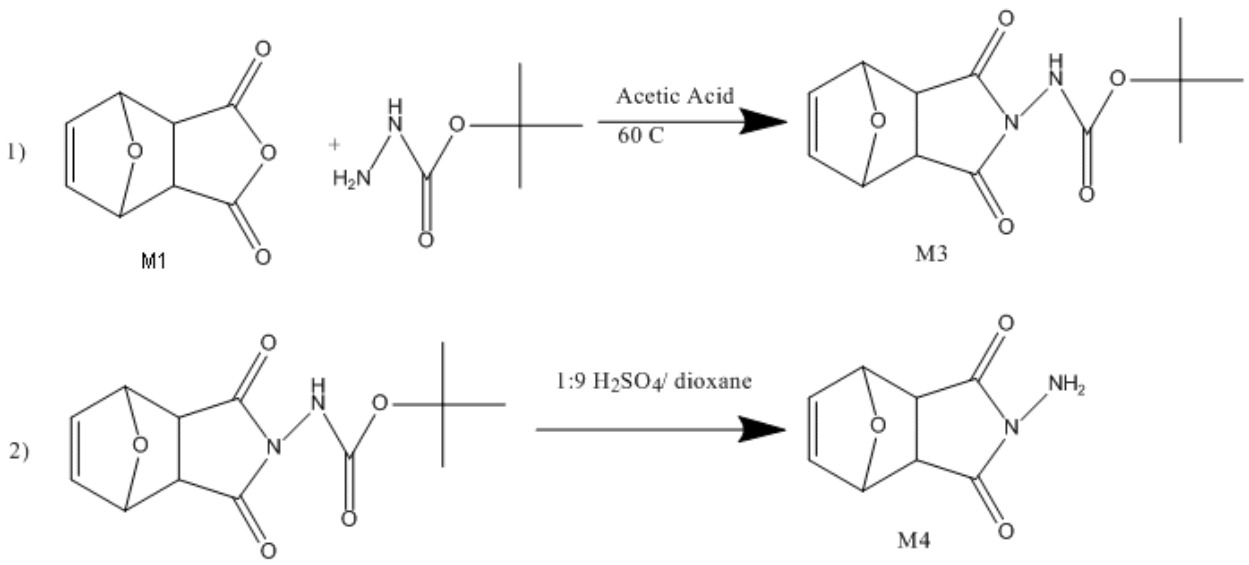

Figure A4. Synthesis route to the amine adduct, M4.

Another molecule synthesized was an amine adduct whose synthesis route is shown in Figure A4.

Step one: A one to one ratio of the maleic anhydride/furan Diels-alder adduct, M1, to tert-butyl carbazate in acetic acid (5.05g Diels-alder adduct, 4.035 g tert-butyl carbazate in 100 ml acetic acid). The reaction was heated to 60 ^{o}C for five hours. The acetic acid was removed via rotoevaporation followed by high vacuum. The product is then recrystalized from ethanol and water. 6.588g t-boc protected adduct product recovered. H-NMR of the product is shown in Figure A5.

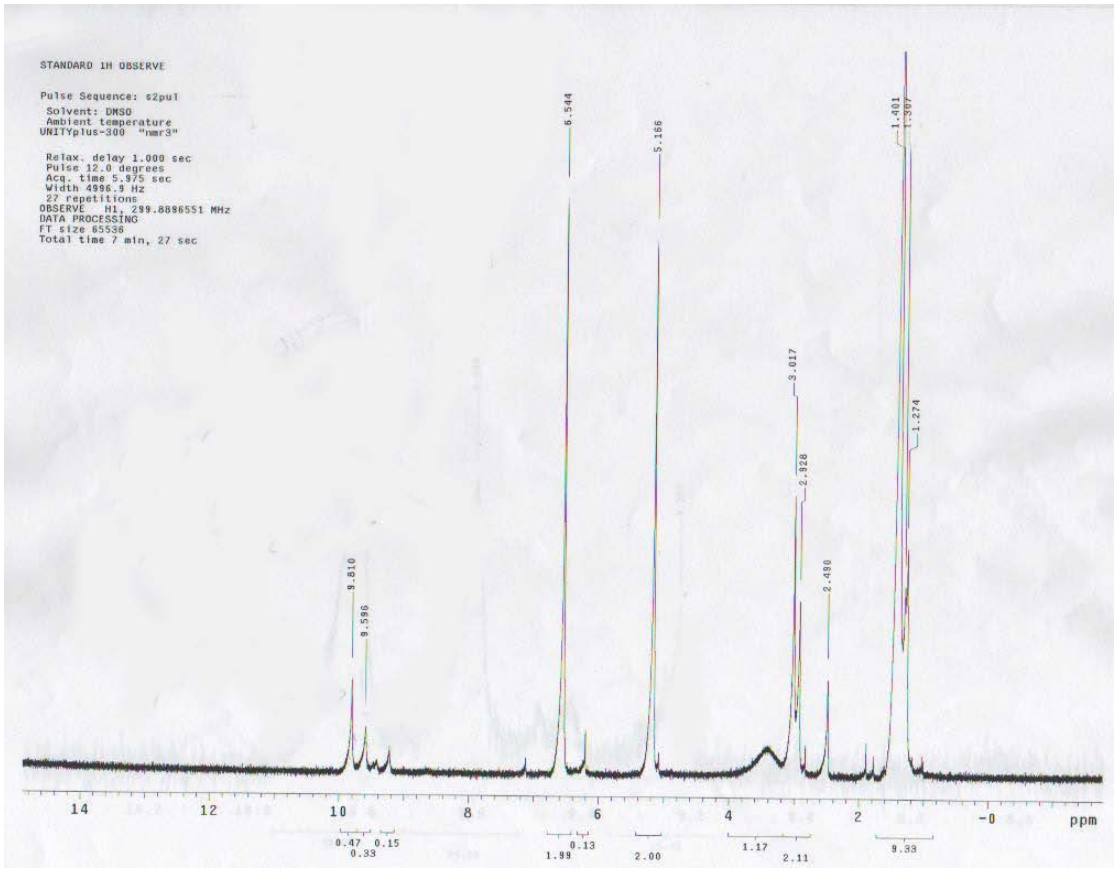

Figure A5. H-NMR of M3 from the first step in the synthesis in Figure A4.

Step two: 0.0975g t-boc protected adduct, M3, is dissolved in 9 ml dioxance in an ice bath until dissolved then 1 ml sulfuric acid added. The reaction is run for two hours then quenched in and ice bath with a saturated sodium bicarbonate solution. The product, M4, is extracted in dichloromethane using an continuous extractor. Yield 3 %.

After testing the HEMI and similar maleimides in the lab it was determined that solubility was an issue. It was then thought that it might be desirable to add additional functionality to the molecules to enhance solubility or to allow the creation of copolymers. The functionalities that were sought to attach to the maleimides were styrene, through the addition of vinyl benzyl chloride, and acrylate through acryloyl chloride. The vinyl benzyl chloride derivative was never

isolated for either the HEMI-adduct or the amine adduct. The acryloyl chloride derivative of the HEMI-adduct was created via the route pictured in Figure A4.

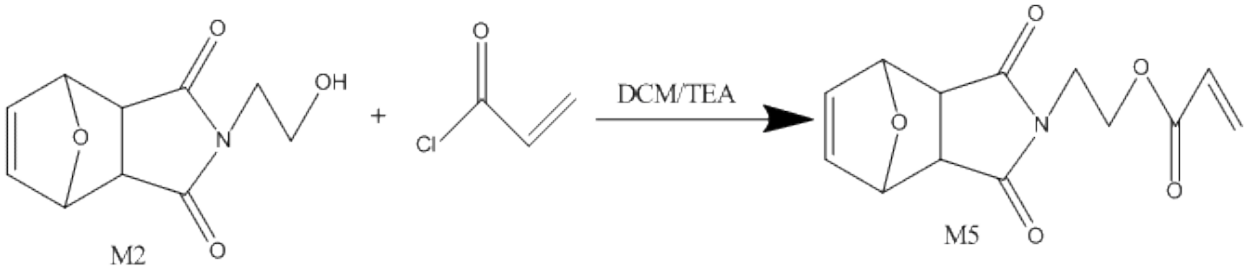

Figure A6. Successful route to the acrylate version of the HEMI-adduct.

The product M5 was created via the synthesis route in Figure A6. To a dry round bottom flask that is kept under nitrogen, 1.8 ml of triethylanime (TEA) were added to 3 grams of M2 along with 30 ml of dry dichloromethane (DCM). A drop funnel is used to add a mixture of 0.9 ml of acryolyl chloride in 10 ml of dry DCM. The reaction is run overnight at room temp. H-NMR of the product M5 is pictured in Figure A7.

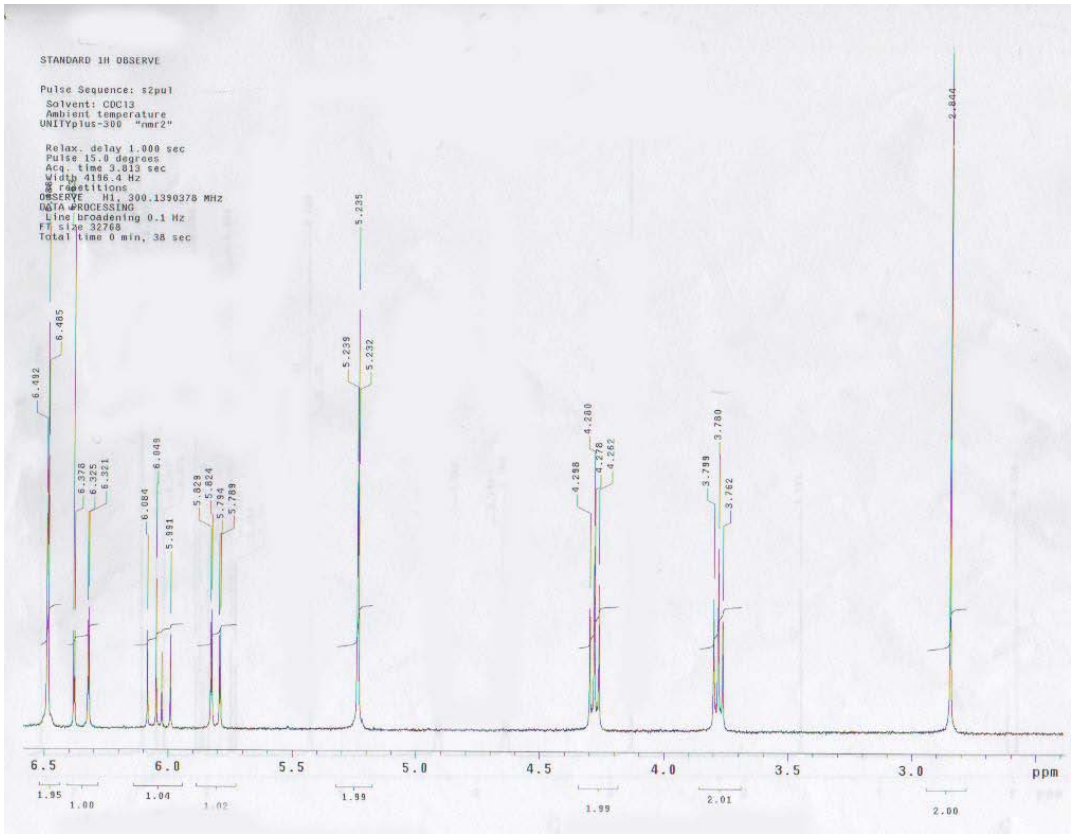

Figure A7. H-MNR of M5 product from synthesis route given in Figure A6.

The next step was to copolymerize the acrylate version of the HEMI-adduct with methyl methacrylate, MMA. A common method to polymerize MMA is to use a thermal radical initiator such as azobisisobutylonitrile, AIBN. This method tends to yield high molecular weight PMMA with a large polydispersity. Due to the effect that low molecular weight polymer tend to form smaller pillars and have lower Tg's, it was decided that low molecular weight PMMA was desirable. A known method to create low molecular PMMA with a low polydisperisty is atom radical transfer radical polymerization, ATRP.

ATRP is a controlled/"living" free radical polymerization discovered at Carnegie Mellon University. The mechanism works to minimize the concentration of free radicals and hence eliminates bimolecular termination, allowing chains to grow at similar rates. This is done by

having the chain ends exist in two states, an active state and a dormant state. The active state occurs when monomer may add to the polymer chain. Thus the polydisperisty of the polymer is capable of being around 1.2. For a typical ATRP reaction, the reaction components include: monomer, solvent, initiator with a halogen attached, copper(I) halide, and a ligand like bipyridine.

I was able to successfully form low molecular weight poly(methylmethacrylate), PMMA. Unfortunately, when the copolymerization was attempted the end product was an insoluble crosslinked solid mass. Even when AIBN was employed the result was the same. Thus this method was abandoned.

The maleimides as a pillars system were saved by the generous donation of two liquid maleimide compounds by Dr. Hoyle of the University of Southern Mississippi. It is these compounds which I used in creating an ideal maleimide system.

APPENDIX B: USING THE HYBRID ACTIVE GAP TOOL

The Hybrid Active Gap Tool is controlled by code run by Labview software package. The following is the procedure used in running a pillars experiment using the Labview interface. The two main interfaces are Motor mode (Figure B1), for large scale movement, and Piezo Mode (Figure B2).

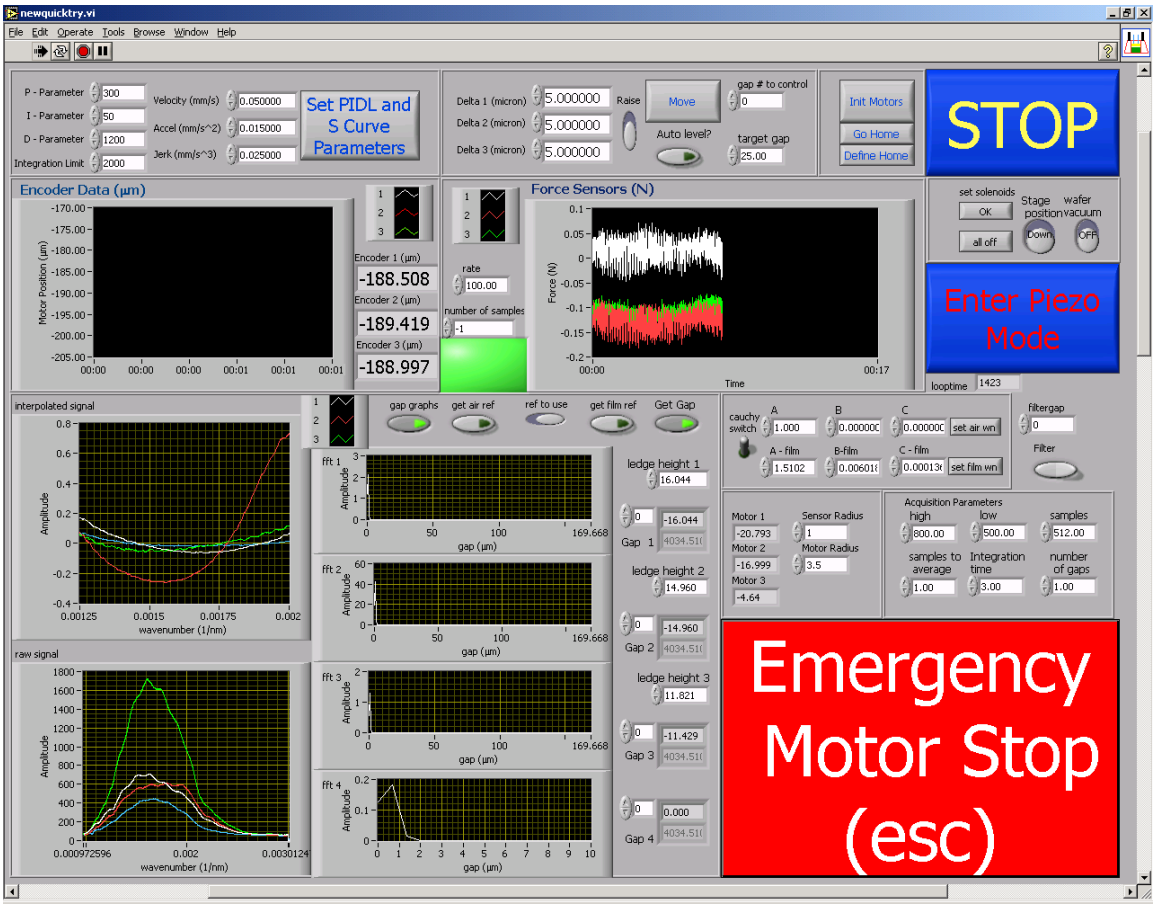

Figure B1. The main control vi for the Hybrid Active gap tool

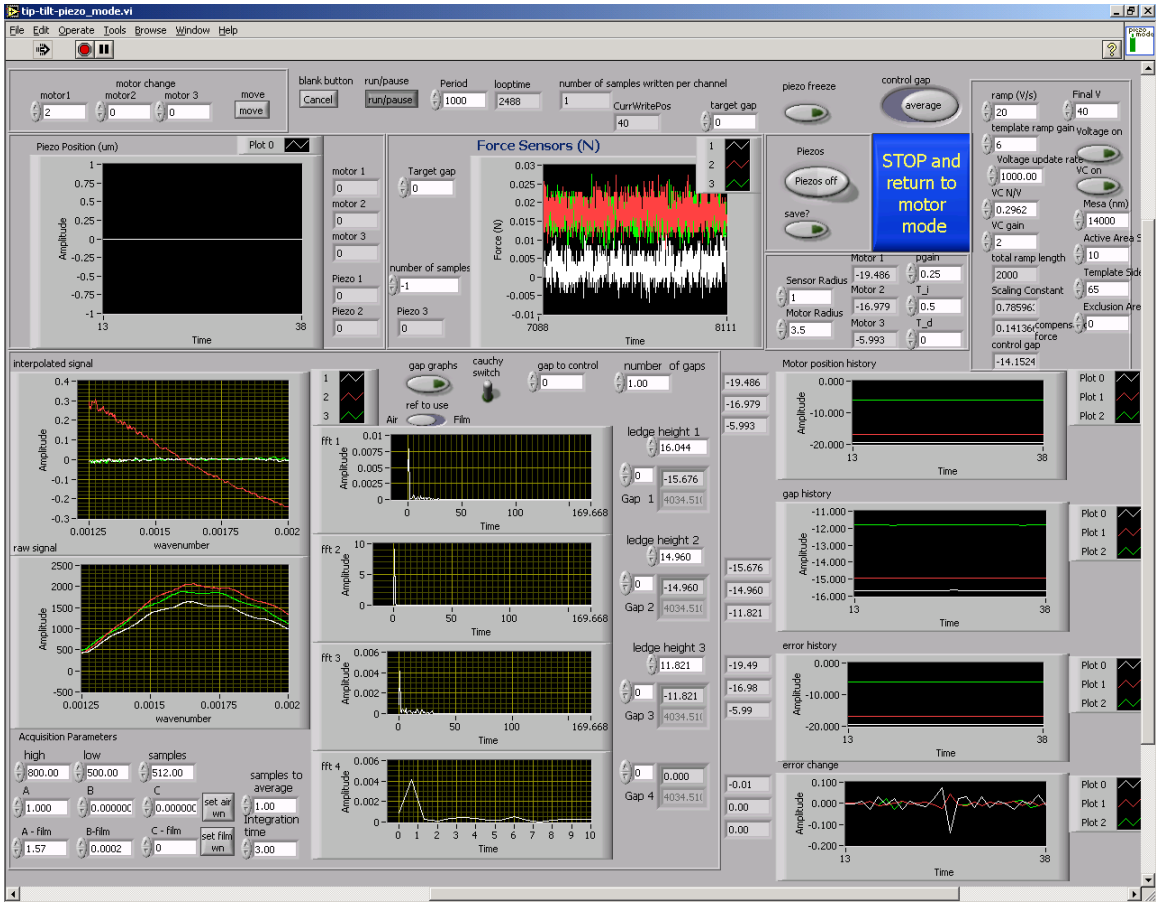

Figure B2. The control vi for peizo control of the Hybrid Active Gap Tool.

B.1 Experimental Procedure

1. Open the current vi
    a. Once LabView Loaded click on GO
        i. The vi will crash on initial start up, close out the screen that pops up and hit Go again

    (Instructions will refer to the vi in Figure B1 unless otherwise stated)

2. Click the Initiate Motors (top button on the left of the STOP button) and the Set PIDL and S Curve Parameters buttons (top left button on screen)

3. Set the stage by ensuring the stage up and vacuum on options are selected (under the STOP button, clicking them changes their status) then hit the set solenoid button to change the status (ok button).
4. Once a wafer is loaded get an air reference, ensure amplitude is about 2500, 4 signals should be present
    a. Hit the air ref button, this will open another interface at 200
        i. Hit the Get ref button
        ii. Once collected hit the stop button
5. Align the wafer chuck and template, by checking motor positions and gap. This is done by entering the amount you want to move in microns into the 3 spaces provided, labeled delta 1, delta 2 and delta then clicking the MOVE button on the right. To move down ensure the Raise lever is down to move up drag the lever up.
    a. Move the template until the gap is approximately 25 microns.
        i. Make sure all signals are registering and that sensor 4 has amplitude of approximately 200.
    b. Move back to 200 microns and retake air reference
6. When a film is present
    a. Fill in Cauchy variables
    b. Fill in mesa heights
    c. Get film reference
        i. Move down to 25 microns
        ii. Get film thickness from using the air reference with the film Cauchy and the 4^{th} signal

d. Ensure template and wafer are still aligned else adjust, until all within 0.5 microns

7. Enter Piezo mode
    a. Enter mesa heights
    b. Turn on piezos
    c. Turn on the gap graphs

When moving the motors try to keep the motors amplitude at zero or close to it (negative numbers move motor up).

If an error occurs while using the piezos turn them off them wait 30 seconds before turning them back on.

1. Turn on the Voice Coils (button labeled VC on), use the button to toggle on the voice coils when voltage is present
2. Note the starting positions of the motors
3. Input the voltage required, then turn on to begin experiment
4. Note drift or suck down
5. Conduct experiment and cured the film
6. Separate in Piezo mode
    a. Turn off
        i. Voltage
        ii. piezoes
7. Once separated go back to motor mode

B2. Determining the Mesa heights (motor mode)

1) Zero all the ledge heights

2) Move to approx 10 microns

3) Minimize the fringe pattern, by looking down through the template to the wafer

4) Then use sensor 4 to do three readings across the active area to get the ledge heights

    a) Record the readings into the ledge calibration spread sheet

        (a) Enter piezo mode, enter the calculated ledge heights, adjust the gap to the gap that experiments will take place at, turn on the piezoes and let them stablize

        (b) Using sensor 4 take the current readings for the ledge heights

            (i) Enter the data into ledge calibration spread sheet

            (ii) Turn off Piezoes, update the ledge height

5) Repeat until the ledge heights give a gap within 50 nm of the reading at sensor four in the center of the active area.

APPENDIX C: INVERSE PROBLEM SUPPORT

C1. Potential Parameter Estimation

The potential parameters for the Lennard-Jones and FENE systems were estimated via group contribution theory. In order to use Equation 2.8 and 2.9, it was necessary to find the accentric factor w, the critical temperature (T_{cr}), and the critical pressure (P_{cr}).

For the chosen group contribution theory[1] the accentric factor, w, is approximated by:

$$exp\left(\frac{w}{a}\right)^{b} - C = \sum_i N_i w_{1i} + A \sum_j M_j w_{2j} \qquad \text{(C1.1)}$$

where w_{1i} is the contribution of the first order group type I that occurs N_i times and w_{2j} is the contribution of the second order j group that occurs. The parameters a,b,c are universal constants having values of 0.4085, 0.5050, and 1.1507. The parameter A is 1 if a second order group is present and 0 if not.

To find T_{cr} and P_{cr} another group contribution theory was chosen, which is based on three orders of contributing groups.[2] The relationships are similar to those of the accentric factor.

$$exp\left(\frac{T_{cr}}{231.239\ K}\right) = \sum_i N_i\, T_{c1i} + \sum_j M_j\, T_{c2j} + \sum_k O_k\, T_{c3k} \qquad \text{(C1.2)}$$

$$(P_{cr} - 5.9827\ bar)^{-0.5} - 0.18998\ bar^{-0.5} = \sum_i N_i\, P_{c1i} + \sum_j M_j\, P_{c2j} + \sum_k O_k\, P_{c3k} \qquad \text{(C1.3)}$$

A sample calculation for methyl methacyrlate:

1st Order Group	Occurrences	Pc1	Tc1	w1
CH_2=CH	1	0.025745	3.2295	0.40842
COO	1	0.013087	4.7346	0
CH_3	2	0.018615	1.7506	0.29602

Table C1.1. The first order groups that contribute to the Tcr, Pcr and w for methyl methacrylate.

2nd Order Group	Occurrences	Pc2	Tc2	w2
CH_2=CHCOOC	1	0.000044	-0.088	0

Table C1.2. The second order groups that contribute to the Tcr, Pcr and w for methyl methacrylate.

P contrib	T contrib	w contrib	Pcr (bar)	Tcr (K)	w
0.076106	11.3773	1.00046	35.16828	562.2854	0.240963

Table C1.3. The overall group that contribute to the Tcr, Pcr and w for methyl methacrylate and the calculated values for Pcr, Tcr and w.

Name	Pcr (bar)	Tcr (K)	w
Methyl Methacrylate	35.16828	562.2854	0.240963
EGDA	27.85054	673.6701	0.273077
t-Butyl Acrylate	29.71365	592.7728	0.230561
Gelest SIA-0210	13.82783	768.1916	0.503785
Darocur 1173	29.10372	787.6451	0.779403

Table C1.4. The calculated values for Pcr, Tcr and w for the etch barrier components and methyl methacrylate.

C2. Inverse Problem Basis

Definition of terms:

M: number of parameters

N: number of molecules

J: number of observations

P: vector of parameters

Z: vector of observations

L: observation function

$A_{\alpha,\beta}$: set of molecules

X_α: vector of molecules$_\alpha$

X_α^o: initial vector of molecules$_\alpha$

u_α: $X_\alpha - X_\alpha^o$ displacement

$U=\{ u_\alpha\}$ set of all displacements

ε: regulation parameter

k: spring constant

l: equilibrium distance

C: constraint equations

f: applied force

λ: step size

The inverse problem is based on minimizing the error found when comparing the calculated observation function from that of the experimental value. In our case, it is the uniaxial strain of a polymer sample. The method employed is the least square method. So given:

$$Q^{LS}(\overline{P}) = \sum_{j=1}^{J} L\left(U(\overline{P}) - z_j\right)^2 + \frac{\varepsilon}{2}\left\|\overline{p} - p^o\right\| \tag{C2.1}$$

we wish to find:

$$\frac{\partial Q}{\partial \overline{P}} = \frac{\partial Q}{\partial U}\frac{dU}{\partial \overline{P}} = 2\sum_{j=1}^{J} L\left(U(\overline{P}) - z_j\right)\frac{\partial L}{\partial P}\bigg|_{U(P)}\frac{dU}{\partial \overline{P}} \tag{C2.2}$$

(note the regularization term has been dropped).

The energy for the harmonic potential model is given by:

$$E^H_{\alpha,\beta} = \frac{1}{2}k_{\alpha\beta}\left(\left\|\overline{x}_\alpha - \overline{x}_\beta\right\| - l^0_{\alpha\beta}\right)^2 \tag{C2.3}$$

Minimizing the energy gives:

$$\frac{\partial E}{\partial u_\alpha} = 0 \tag{C2.4}$$

The constraint equation which factors in the applied force is then:

$$\overline{C}(U(\overline{P}), \overline{P}) = \sum_{\beta=1}^{N}\frac{\partial E_{\alpha\beta}}{\partial u_\alpha} - f_\alpha = 0 \tag{C2.5}$$

In order to find $\frac{dU}{\partial \overline{P}}$, the derivation of the constraint equation is necessary.

$$\frac{d\overline{C}_\alpha}{d\overline{P}} = \frac{\partial \overline{C}_\alpha}{\partial \overline{P}} + \frac{\partial \overline{C}_\alpha}{\partial U}\bigg|_{Uj}\frac{\partial U_j}{\partial \overline{P}} = \frac{\partial \overline{C}_\alpha}{\partial \overline{P}} + A\frac{\partial U_j}{\partial \overline{P}} = 0 \tag{C2.6}$$

Thus

$$-\frac{\partial \overline{C}_\alpha}{\partial \overline{P}} = A\frac{\partial U_j}{\partial \overline{P}} \tag{C2.7}$$

or

$$\frac{\partial U_j}{\partial \overline{P}} = -A^{-1}\frac{\partial \overline{C}_\alpha}{\partial \overline{P}} \tag{C2.8}$$

Substituting back into C2.2 gives

$$\frac{\partial Q}{\partial \overline{\overline{P}}} = \frac{\partial Q}{\partial U}\left(- A^{-1} \frac{\partial \overline{C}_{\alpha}}{\partial \overline{\overline{P}}} \right) \tag{C2.9}$$

Let

$$v = -\frac{\partial Q}{\partial U} A \tag{C2.10}$$

The dual problem is then:

$$vA = -\frac{\partial Q}{\partial U} \tag{C2.11}$$

OR

$$v^T A^T = -\left(\frac{\partial Q}{\partial U} \right)^T \tag{C2.12}$$

The parameters are updated according to:

$$P_{i+1} = P_i - \lambda \frac{\partial Q}{\partial P}\bigg|_{Pi} \tag{C2.13}$$

And continue to solve and update until $\frac{\partial Q}{\partial \overline{\overline{P}}}$ is within tolerance.

C3. References

1. Constantinou, L.; Gani, R.; O'Connell, J. P., Estimation of the acentric factor and the liquid molar volume at 298 K using a new group contribution method. *Fluid Phase Equilibria* **1995,** 103, (1), 11-22.

2. Marrero, J.; Gani, R., Group-contribution based estimation of pure component properties. *Fluid Phase Equilibria* **2001,** 183-184, 183-208.

Sources Cited

CHAPTER 1

1. Moore, G. E., Cramming more Components onto Integrated Circuits. *Electronics Magazine* **1965,** 19.

2. Thompson, L. F. W., C. G.; Bowden, M. J., *Introduction to Microlithography*. Second ed.; American Chemical Society: Washington, DC, 1994.

3. Trenkler, H. E. a. J., EUV lithography: technology for the semiconductor industry in 2010. *Europhysics News* **2004,** 35, (5).

4. Taylor, J. C. Advanced lithographic patterning technologies: materials and processes. University of Texas, Austin, 2007.

5. French, R. H.; Tran, H. V.; Adelman, D. J.; Rogado, N. S.; Kaku, M.; Mocella, M.; Chen, C. Y.; Hendrickx, E.; Van Roey, F.; Bernfeld, A. S.; Derryberry, R. A., High-index immersion fluids enabling cost-effective single-exposure lithography for 32 nm half pitches. *Proceedings of SPIE* **2008,** 6924, (Pt. 1, Optical Microlithography XXI), 692417/1-692417/8.

6. Furukawa, T.; Kishida, T.; Yasuda, K.; Shimokawa, T.; Liu, Z.; Slezak, M.; Hieda, K., High refractive index materials design for the next generation ArF immersion lithography. *Proceedings of SPIE* **2008,** 6924, (Pt. 1, Optical Microlithography XXI), 692412/1-692412/8.

7. Liberman, V.; Rothschild, M.; Palmacci, S. T.; Bristol, R.; Byers, J.; Turro, N. J.; Lei, X.; O'Connor, N.; Zimmerman, P. A., High-index immersion lithography: preventing lens photocontamination and identifying optical behavior of LuAG. *Proceedings of SPIE* **2008,** 6924, (Pt. 1, Optical Microlithography XXI), 692416/1-692416/11.

8. Sewell, H.; Mulkens, J.; Graeupner, P.; McCafferty, D.; Markoya, L.; Donders, S.; Cortie, R.; Meijers, R.; Evangelista, F.; Samarakone, N., High-n immersion lithography. *Proceedings of SPIE* **2008,** 6924, (Pt. 1, Optical Microlithography XXI), 692415/1-692415/12.

9. Tran, H. V. Evaluation of Next Generation Fluids for ArF Immersion Lithography Beyond Water. http://www2.dupont.com/Semi_Fabrication/en_US/assets/downloads/pdf/science/ArFImmersionpaper.pdf

10. Wilson, R. Immersion-lithography road map hits dead end. http://www.edn.com/index.asp?layout=article&articleid=CA6355060 (7/27/2008),

11. Chandhok, M.; Lee, S. H.; Bacuita, T., Effects of flare in extreme ultraviolet lithography: Learning from the engineering test stand. *Journal of Vacuum Science & Technology, B: Microelectronics and Nanometer Structures* **2004,** 22, (6), 2966-2969.

12. Lammers, D. Intel: 'EUV Facts Don't Add Up' for 22 nm in 2011. http://www.semiconductor.net/article/CA6553758.html

13. Mutschler, A. S. Why design engineers need to know about lithography. http://www.edn.com/article/CA6504364.html (7/27/2008),

14. Hua, F.; Sun, Y.; Gaur, A.; Meitl, M. A.; Bilhaut, L.; Rotkina, L.; Wang, J.; Geil, P.; Shim, M.; Rogers, J. A.; Shim, A., Polymer Imprint Lithography with Molecular-Scale Resolution. *Nano Letters* **2004,** 4, (12), 2467-2471.

15. Ding, Y.; Ro, H. W.; Germer, T. A.; Douglas, J. F.; Okerberg, B. C.; Karim, A.; Soles, C. L., Relaxation Behavior of Polymer Structures Fabricated by Nanoimprint Lithography. *ACS Nano* **2007,** 1, (2), 84-92.

16. Schmid, G. M.; Stewart, M. D.; Wetzel, J.; Palmieri, F.; Hao, J.; Nishimura, Y.; Jen, K.; Kim, E. K.; Resnick, D. J.; Liddle, J. A.; Willson, C. G., Implementation of an imprint damascene process for interconnect fabrication. *Journal of Vacuum Science & Technology, B: Microelectronics and Nanometer Structures--Processing, Measurement, and Phenomena* **2006,** 24, (3), 1283-1291.

17. Palmieri, F.; Stewart, M. D.; Wetzel, J.; Hao, J.; Nishimura, Y.; Jen, K.; Flannery, C.; Li, B.; Chao, H.-L.; Young, S.; Kim, W. C.; Ho, P. S.; Willson, C. G., Multi-level step and flash imprint lithography for direct patterning of dielectrics. *Proceedings of SPIE-The International Society for Optical Engineering* **2006,** 6151, (Pt. 1, Emerging Lithographic Technologies X), 61510J/1-61510J/9.

18. Stewart, M. D.; Wetzel, J. T.; Schmid, G. M.; Palmieri, F.; Thompson, E.; Kim, E. K.; Wang, D.; Sotodeh, K.; Jen, K.; Johnson, S. C.; Hao, J.; Dickey, M. D.; Nishimura, Y.; Laine, R. M.; Resnick, D. J.; Willson, C. G., Direct imprinting of dielectric materials for dual damascene processing. *Proceedings of SPIE-The International Society for Optical Engineering* **2005,** 5751, (Pt. 1, Emerging Lithographic Technologies IX), 210-218.

19. Sreenivasan, S. V.; Willson, C. G.; Schumaker, N. E.; Resnick, D. J. In *Cost of Ownership Analysis for Patterning Using Step and Flash Imprint Lithography*, Proc. SPIE 4688, 2002; 2002.

20. Kanellos, M. Soaring costs of chipmaking recast industry. http://news.cnet.com/Semi-survival/2009-1001_3-981418.html (11/21/2008),

21. Chou, S. Y.; Zhuang, L., Lithographically induced self-assembly of periodic polymer micropillar arrays. *Journal of Vacuum Science & Technology, B: Microelectronics and Nanometer Structures* **1999,** 17, (6), 3197-3202.

22. Pease, L. F.; Russel, W. B., Electrostatically induced submicron patterning of thin perfect and leaky dielectric films: A generalized linear stability analysis. *Journal of Chemical Physics* **2003,** 118, (8), 3790-3803.

23. Yan, X.; Liu, G.; Dickey, M.; Willson, C. G., Preparation of porous polymer membranes using nano- or micro-pillar arrays as templates. *Polymer* **2004,** 45, (25), 8469-8474.

24. Hawker, C. J.; Russell, T. P., Block copolymer lithography: Merging "bottom-up" with "top-down" processes. *MRS Bulletin* **2005,** 30, (12), 952-966.

25. Karim, A.; Berry, B. C.; Bosse, A.; Jones, R. L.; Douglas, J. F., Evolution of orientational order in directed assembly of block copolymer films. *Abstracts of Papers, 235th ACS National Meeting, New Orleans, LA, United States, April 6-10, 2008* **2008**, POLY-562.

26. Yang, J.; Sekine, R.; Aoki, H.; Ito, S., Localization and Orientation of Homopolymer in Block Copolymer Lamella: A Near-Field Optical Microscopy Study. *Macromolecules* **2007,** 40, (21), 7573-7580.

27. Mita, K.; Tanaka, H.; Saijo, K.; Takenaka, M.; Hashimoto, T., Cylindrical Domains of Block Copolymers Developed via Ordering under Moving Temperature Gradient. *Macromolecules* **2007,** 40, (16), 5923-5933.

28. Tsori, Y., Lamellar Phases in Nonuniform Electric Fields: Breaking the In-Plane Rotation Symmetry and the Role of Dielectric Constant Mismatch. *Macromolecules* **2007,** 40, (5), 1698-1702.

29. Olszowka, V.; Hund, M.; Kuntermann, V.; Scherdel, S.; Tsarkova, L.; Boeker, A.; Krausch, G., Large scale alignment of a lamellar block copolymer thin film via electric fields: a time-resolved SFM study. *Soft Matter* **2006,** 2, (12), 1089-1094.

30. Boeker, A.; Schmidt, K.; Knoll, A.; Zettl, H.; Haensel, H.; Urban, V.; Abetz, V.; Krausch, G., The influence of incompatibility and dielectric contrast on the electric field-induced orientation of lamellar block copolymers. *Polymer* **2006,** 47, (3), 849-857.

31. Schmidt, K.; Boeker, A.; Zettl, H.; Schubert, F.; Haensel, H.; Fischer, F.; Weiss, T. M.; Abetz, V.; Zvelindovsky, A. V.; Sevink, G. J. A.; Krausch, G., Influence of Initial Order on the Microscopic Mechanism of Electric Field Induced Alignment of Block Copolymer Microdomains. *Langmuir* **2005,** 21, (25), 11974-11980.

32. Xiang, H.; Lin, Y.; Russell, T. P., Electrically Induced Patterning in Block Copolymer Films. *Macromolecules* **2004,** 37, (14), 5358-5363.

33. DeRouchey, J.; Thurn-Albrecht, T.; Russell, T. P.; Kolb, R., Block Copolymer Domain Reorientation in an Electric Field: An in-Situ Small-Angle X-ray Scattering Study. *Macromolecules* **2004,** 37, (7), 2538-2543.

34. Boeker, A.; Elbs, H.; Haensel, H.; Knoll, A.; Ludwigs, S.; Zettl, H.; Zvelindovsky, A. V.; Sevink, G. J. A.; Urban, V.; Abetz, V.; Mueller, A. H. E.; Krausch, G., Electric field induced alignment of concentrated block copolymer solutions. *Macromolecules* **2003,** 36, (21), 8078-8087.

35. Xu, T.; Hawker, C. J.; Russell, T. P., Interfacial Energy Effects on the Electric Field Alignment of Symmetric Diblock Copolymers. *Macromolecules* **2003,** 36, (16), 6178-6182.

36. Tsori, Y.; Tournilhac, F.; Leibler, L., Orienting Ion-Containing Block Copolymers Using Ac Electric Fields. *Macromolecules* **2003,** 36, (15), 5873-5877.

37. Elhadj, S.; Woody, J. W.; Niu, V. S.; Saraf, R. F., Orientation of self-assembled block copolymer cylinders perpendicular to electric field in mesoscale film. *Applied Physics Letters* **2003,** 82, (6), 871-873.

38. Huang, E.; Russell, T. P.; Harrison, C.; Chaikin, P. M.; Register, R. A.; Hawker, C. J.; Mays, J., Using Surface Active Random Copolymers To Control the Domain Orientation in Diblock Copolymer Thin Films. *Macromolecules* **1998,** 31, (22), 7641-7650.

39. Mansky, P.; Liu, Y.; Huang, E.; Russell, T. P.; Hawker, C., Controlling polymer-surface interactions with random copolymer brushes. *Science* **1997,** 275, (5305), 1458-1460.

40. Braunecker, W. A.; Matyjaszewski, K., Controlled/living radical polymerization: Features, developments, and perspectives. [Erratum to document cited in CA147:486671]. *Progress in Polymer Science* **2008,** 33, (1), 165.

41. Matyjaszewski, K.; Spanswick, J., Controlled/living radical polymerization. *Plastics Engineering* **2005,** 70, (Handbook of Polymer Synthesis (2nd Edition)), 895-941.

CHAPTER 2

1. Colburn, M. Step and flash imprint lithography: a low-pressure, room-temperature nanoimprint lithography. University of Texas, Austin, 2001.

2. Palmieri, F. Step and Flash Imprint Lithography: Materials and Applications for the Manufacture of Advanced Integrated Circuits. University of Texas, Austin, 2008.

3. Colburn, M.; Johnson, S.; Stewart, M.; Damle, S.; Bailey, T. C.; Choi, B.; Wedlake, M.; Michaelson, T.; Sreenivasan, S. V.; Ekerdt, J.; Willson, C. G., Step and flash imprint lithography: a new approach to high-resolution patterning. *Proceedings of SPIE-The International Society for Optical Engineering* **1999,** 3676, (Pt. 1, Emerging Lithographic Technologies III), 379-389.

4. Johnson, S. C. Step and flash imprint lithography materials and process development. University of Texas, Austin, 2005.

5. Johnson, S.; Burns, R.; Kim, E. K.; Schmid, G.; Dickey, M.; Meiring, J.; Burns, S.; Stacey, N.; Willson, C. G.; Convey, D.; Wei, Y.; Fejes, P.; Gehoski, K.; Mancini, D.; Nordquist, K.; Dauksher, W. J.; Resnick, D. J., Step and flash imprint lithography modeling and process development. *Journal of Photopolymer Science and Technology* **2004,** 17, (3), 417-420.

6. Bohme, T. R.; de Pablo, J. J., Evidence for size-dependent mechanical properties from simulations of nanoscopic polymeric structures. *Journal of Chemical Physics* **2002,** 116, (22), 9939-9951.

7. Stoykovich, M. P.; Yoshimoto, K.; Nealey, P. F., Mechanical properties of polymer nanostructures: measurements based on deformation in response to capillary forces. *Applied Physics A: Materials Science & Processing* **2008,** 90, (2), 277-283.

8. Cheng, W.; Sainidou, R.; Burgardt, P.; Stefanou, N.; Kiyanova, A.; Efremov, M.; Fytas, G.; Nealey, P. F., Elastic Properties and Glass Transition of Supported Polymer Thin Films. *Macromolecules* **2007,** 40, (20), 7283-7290.

9. Yoshimoto, K.; Jain, T. S.; Van Workum, K.; Nealey, P. F.; De Pablo, J. J., Mechanical Heterogeneities in Model Polymer Glasses at Small Length Scales. *Physical Review Letters* **2004,** 93, (17), 175501/1-175501/4.

10. Fryer, D. S.; Nealey, P. F.; de Pablo, J. J., Scaling of Tg and reaction rate with film thickness in photoresist: A thermal probe study. *Journal of Vacuum Science & Technology, B: Microelectronics and Nanometer Structures* **2000,** 18, (6), 3376-3380.

11. Torres, J. A.; Nealey, P. F.; de Pablo, J. J., Molecular Simulation of Ultrathin Polymeric Films near the Glass Transition. *Physical Review Letters* **2000,** 85, (15), 3221-3224.

12. Burns, R. L.; Johnson, S. C.; Schmid, G. M.; Kim, E. K.; Dickey, M. D.; Meiring, J.; Burns, S. D.; Stacey, N. A.; Willson, C. G.; Convey, D.; Wei, Y.; Fejes, P.; Gehoski, K. A.; Mancini, D. P.; Nordquist, K. J.; Dauksher, W. J.; Resnick, D. J., Mesoscale modeling for SFIL

simulating polymerization kinetics and densification. *Proceedings of SPIE-The International Society for Optical Engineering* **2004,** 5374, (Pt. 1, Emerging Lithographic Technologies VIII), 348-360.

13. Dickey, M. D.; Burns, R. L.; Kim, E. K.; Johnson, S. C.; Stacey, N. A.; Willson, C. G., Study of the kinetics of Step and Flash imprint lithography photopolymerization. *AIChE Journal* **2005,** 51, (9), 2547-2555.

14. Dickey, M. D.; Willson, C. G., Kinetic parameters for step and flash imprint lithography photopolymerization. *AIChE Journal* **2006,** 52, (2), 777-784.

15. Bailey, T.; Choi, B. J.; Colburn, M.; Meissl, M.; Shaya, S.; Ekerdt, J. G.; Sreenivasan, S. V.; Willson, C. G., Step and flash imprint lithography: Template surface treatment and defect analysis. *Journal of Vacuum Science & Technology, B: Microelectronics and Nanometer Structures* **2000,** 18, (6), 3572-3577.

16. Reid, R. C. P., J.M.;Sherwood, T.K., *The Properties of Gases and Liquids*. McGrawHill: 1977.

17. Constantinou, L.; Gani, R.; O'Connell, J. P., Estimation of the acentric factor and the liquid molar volume at 298 K using a new group contribution method. *Fluid Phase Equilibria* **1995,** 103, (1), 11-22.

18. Marrero, J.; Gani, R., Group-contribution based estimation of pure component properties. *Fluid Phase Equilibria* **2001,** 183-184, 183-208.

19. Retkute, R.; Gleeson, J. P., Dynamics of two coupled particles: comparison of Lennard-Jones and spring forces. *Proceedings of SPIE-The International Society for Optical Engineering* **2005,** 5845, (Noise in Complex Systems and Stochastic Dynamics III), 61-71.

20. Balay, S.; Buschelman, K.; Gropp, W. D.; Kaushik, D.; Knepley, M. G.; McInnes, L. C.; Smith, B. F.; Zhang, H. PETSc Web page. http://www.mcs.anl.gov/petsc

21. S. Benson, L. C. M., J. Morre, T. Munson, and J. Sarich TAO
user manual (revision 1.9). http://www.mcs.anl.gov/tao

22. Bauman, P. T. Adaptive Multiscale Modeling of Polymeric Materials Using Goal-Oriented Error Estimation, Arlequin Coupling, and Goals Algorithms. University of Texas, Austin, 2008.

CHAPTER 3

1. Marin, G. B., *Advances in Chemical Engineering: Multiscale Analysis [electronic resource]*. Elsevier: Burlington, 2005; p 323.

2. Naqui, S. I.; Robinson, I. M., Review Tensile dilatomeric studies of deformation in polymeric materials and their composites. *Journal of Materials Science* **1993,** 28, 1421-1429.

3. Bauman, P. T. Adaptive Multiscale Modeling of Polymeric Materials Using Goal-Oriented Error Estimation, Arlequin Coupling, and Goals Algorithms. University of Texas, Austin, 2008.

4. Ben Dhia, H., Multiscale mechanical problems: the Arlequin method. *C. R. Acad. Sci., Ser. IIb: Mec., Phys., Astron.* **1998,** 326, (12), 899-904.

CHAPTER 4

1. Chou, S. Y.; Krauss, P. R.; Renstrom, P. J., Imprint of sub-25 nm vias and trenches in polymers. *Applied Physics Letters* **1995,** 67, (21), 3114-16.

2. Schaffer, E.; Thurn-Albrecht, T.; Russell, T. P.; Steiner, U., Electrically induced structure formation and pattern transfer. *Nature (London)* **2000,** 403, (6772), 874-877.

3. Chou, S. Y.; Zhuang, L., Lithographically induced self-assembly of periodic polymer micropillar arrays. *Journal of Vacuum Science & Technology, B: Microelectronics and Nanometer Structures* **1999,** 17, (6), 3197-3202.

4. Chou, S. Y.; Zhuang, L.; Guo, L., Lithographically induced self-construction of polymer microstructures for resistless patterning. *Applied Physics Letters* **1999,** 75, (7), 1004-1006.

5. Schaffer, E.; Thurn-Albrecht, T.; Russell, T. P.; Steiner, U., Electrohydrodynamic instabilities in polymer films. *Europhysics Letters* **2001,** 53, (4), 518-524.

6. Lin, Z.; Kerle, T.; Baker, S. M.; Hoagland, D. A.; Schaffer, E.; Steiner, U.; Russell, T. P., Electric field induced instabilities at liquid/liquid interfaces. *Journal of Chemical Physics* **2001,** 114, (5), 2377-2381.

7. Pease, L. F.; Russel, W. B., Electrostatically induced submicron patterning of thin perfect and leaky dielectric films: A generalized linear stability analysis. *Journal of Chemical Physics* **2003,** 118, (8), 3790-3803.

8. Pease, L. F., III; Russel, W. B., Limitations on length scales for electrostatically induced submicrometer pillars and holes. *Langmuir* **2004,** 20, (3), 795-804.

9. Deshpande, P.; Pease, L. F., III; Chen, L.; Chou, S. Y.; Russel, W. B., Cylindrically symmetric electrohydrodynamic patterning. *Physical Review E: Statistical, Nonlinear, and Soft Matter Physics* **2004,** 70, (4-1), 041601/1-041601/12.

10. Wu, N.; Pease, L. F., III; Russel, W. B., Electric-Field-Induced Patterns In Thin Polymer Films: Weakly Nonlinear and Fully Nonlinear Evolution. *Langmuir* **2005,** 21, (26), 12290-12302.

11. Wu, N.; Russel, W. B., Dynamics of the formation of polymeric microstructures induced by electrohydrodynamic instability. *Applied Physics Letters* **2005,** 86, (24), 241912/1-241912/3.

12. Verma, R.; Sharma, A.; Kargupta, K.; Bhaumik, J., Electric Field Induced Instability and Pattern Formation in Thin Liquid Films. *Langmuir* **2005,** 21, (8), 3710-3721.

13. Dickey, M. Development of Photocurable Pillar Arrays Formed via Electrohydrodynamic Instabilities. Doctor of Philosophy, University of Texas, Austin, 2006.

14. Dickey, M. D.; Gupta, S.; Leach, K. A.; Collister, E.; Willson, C. G.; Russell, T. P., Novel 3-D Structures in Polymer Films by Coupling External and Internal Fields. *Langmuir* **2006,** 22, (9), 4315-4318.

15. Leach, K. A.; Gupta, S.; Dickey, M. D.; Willson, C. G.; Russell, T. P., Electric field and dewetting induced hierarchical structure formation in polymer/polymer/air trilayers. *Chaos* **2005,** 15, (4), 047506/1-047506/5.

16. Morariu, M. D.; Voicu, N. E.; Schaeffer, E.; Lin, Z.; Russell, T. P.; Steiner, U., Hierarchical structure formation and pattern replication induced by an electric field. *Nature Materials* **2003,** 2, (1), 48-52.

CHAPTER 5

1. Dickey, M. D.; Collister, E.; Raines, A.; Tsiartas, P.; Holcombe, T.; Sreenivasan, S. V.; Bonnecaze, R. T.; Willson, C. G., Photocurable Pillar Arrays Formed via Electrohydrodynamic Instabilities. *Chemistry of Materials* **2006,** 18, (8), 2043-2049.

2. Dickey, M. D.; Willson, C. G., Kinetic parameters for step and flash imprint lithography photopolymerization. *AIChE Journal* **2006,** 52, (2), 777-784.

3. Decker, C. a. A. D. J., Kinetic approach of oxygen inhibition in ultraviolet- and laser-induced polymerizations. *Macromolecules* **1985,** 18, (6), 1241-1244.

4. Decker, C., The use of UV irradiation in polymerization. *Polymer International* **1998,** 45, (2), 133-141.

5. Decker, C., Kinetic study and new applications of UV radiation curing. *Macromolecular Rapid Communications* **2002,** 23, (18), 1067-1093.

6. Kim, E. K. Development and Study of Nano-Imprint and Electron Beam Lithography Materials for Semiconductor Devices. University of Texas, Austin, 2005.

7. Hoyle, C. E.; Lee, T. Y.; Roper, T., Thiol-enes: Chemistry of the past with promise for the future. *Journal of Polymer Science, Part A: Polymer Chemistry* **2004,** 42, (21), 5301-5338.

8. Jacobine, A. F., Thiol-ene photopolymers. *Radiat. Curing Polym. Sci. Technol.* **1993,** 3, 219-68.

9. Cramer, N. B.; Scott, J. P.; Bowman, C. N., Photopolymerizations of Thiol-Ene Polymers without Photoinitiators. *Macromolecules* **2002,** 35, (14), 5361-5365.

10. Decker, C.; Bianchi, C.; Morel, F.; Jonsson, S.; Hoyle, C., Mechanistic study of the light-induced copolymerization of maleimide/vinyl ether systems. *Macromolecular Chemistry and Physics* **2000,** 201, (13), 1493-1503.

11. Clark, S. C.; Jonsson, S.; Hoyle, C. E., Maleimides with carbonate and urethane groups as photoinitiators for acrylate polymerization. *Polymer Preprints (American Chemical Society, Division of Polymer Chemistry)* **1997,** 38, (2), 363-364.

12. Hoyle, C. E.; Clark, S. C.; Jonsson, S.; Shimose, M., Photopolymerization using maleimides as photoinitiators. *Polymer* **1997,** 38, (22), 5695-5697.

13. Decker, C.; Morel, F.; Jonsson, S.; Clark, S.; Hoyle, C., Light-induced polymerization of photoinitiator-free vinyl ether/maleimide systems. *Macromolecular Chemistry and Physics* **1999,** 200, (5), 1005-1013.

14. Jonsson, E. S. Y., Danning; Viswanathan, Kalyanaraman; Lindgren, Karin; Holye, Charles, Photoinduced Free Radical Ring Opening Copolymerization in Acceptor/Donor Systems. *RadTech Europe 02:[Conference Proceedings], April Session* **2002**.

15. Hoyle, C. E.; Viswanathan, K.; Clark, S. C.; Miller, C. W.; Nguyen, C.; Joensson, S.; Shao, L., Sensitized Polymerization of an Acrylate/Maleimide System. *Macromolecules* **1999,** 32, (8), 2793-2795.

16. Jonsson, S.; Viswanathan, K.; Hoyle, C. E.; Clark, S. C.; Miller, C.; Morel, F.; Decker, C., Recent advances in photoinduced donor/acceptor copolymerization. *Nuclear Instruments & Methods in Physics Research, Section B: Beam Interactions with Materials and Atoms* **1999,** 151, (1-4), 268-278.

17. Yang, D.; Viswanathan, K.; Hoyle, C. E.; Jonsson, S.; Hasselgren, C., Studies of initiation mechanism of maleimide/vinyl ether copolymerizations. *Experience the World of UV/EB, RadTech 2000: The Premier UV/EB Conference & Exhibition, Technical Conference Proceedings, Baltimore, MD, United States, Apr. 9-12, 2000* **2000**, 221-230.

18. Decker, C., et la, Mechanistic study of the light-induced copolymerization of maleimide/vinyl ether systems. *Macromolecular Chemistry and Physics* **2000,** 201, (13), 1493-1503.

19. Dickey, M. D.; Burns, R. L.; Kim, E. K.; Johnson, S. C.; Stacey, N. A.; Willson, C. G., Study of the kinetics of Step and Flash imprint lithography photopolymerization. *AIChE Journal* **2005,** 51, (9), 2547-2555.

20. Raines, A. Nano-Scale Large Area Gap Control for High Throughput Electrically Induced Micro-Patterning. University of Texas, Austin, 2007.

21. Dickey, M. D.; Raines, A.; Collister, E.; Bonnecaze, R. T.; Sreenivasan, S. V.; Willson, C. G., High-aspect ratio polymeric pillar arrays formed via electrohydrodynamic patterning. *Journal of Materials Science* **2008,** 43, (1), 117-122.

CHAPTER 6

1. Verma, R.; Sharma, A.; Kargupta, K.; Bhaumik, J., Electric Field Induced Instability and Pattern Formation in Thin Liquid Films. *Langmuir* **2005,** 21, (8), 3710-3721.

2. Wu, N.; Pease, L. F., III; Russel, W. B., Electric-Field-Induced Patterns In Thin Polymer Films: Weakly Nonlinear and Fully Nonlinear Evolution. *Langmuir* **2005,** 21, (26), 12290-12302.

3. Wang, R. X. B., C. D. ; Fung, S. ; Djurisic, A. B. ; Ling, C. C. ; Kwong, C. ; Li, S., Influence of annealing temperature and environment on the properties of indium tin oxide thin films. *Journal of Physics D: Applied Physics* **2005,** 38, 2000-2005.

4. Wu, K. Interface study for template release in step and flash imprint lithography. University of Texas, Austin, 2006.

5. Tasker, S., Chambers, R. D., and Badyal, J. P. S., Surface defluorination of PTFE by sodium atoms. *The Journal of Physical Chemistry* **1994,** 98, (47), 12442-12446.

6. Garidel, S., Zelsmann, M., Chaix, N., Voisin, P., Boussy, J., Beaurain, A., and Pelissier, B., Improved release stragety for UV nanoimprint lithography. *Journal of Vacuum Science & Technology, B: Microelectronics and Nanometer Structures* **2007,** 25, (6), 2430-2434.

7. Houle, F. A.; Rettner, C. T.; Miller, D. C.; Sooriyakumaran, R., Antiadhesion considerations for UV nanoimprint lithography. *Applied Physics Letters* **2007,** 90, 213103.

8. Bailey, T.; Choi, B. J.; Colburn, M.; Meissl, M.; Shaya, S.; Ekerdt, J. G.; Sreenivasan, S. V.; Willson, C. G., Step and flash imprint lithography: Template surface treatment and defect analysis. *Journal of Vacuum Science & Technology, B: Microelectronics and Nanometer Structures* **2000,** 18, (6), 3572-3577.

9. Wu, K.; Wang, X.; Kim, E. K.; Willson, C. G.; Ekerdt, J., Experimental and theoretical investagation on the surfactant segregation in imprint lithography. *Langmuir* **2007,** 23, (3), 1166-1170.

10. Tada, Y.; Yoshida, H.; Miyauchi, A., Analysis on the deterioration mechanism of the release layer in nanoimprint process. *Journal of Photopolymer Science and Technology* **2007,** 20, (4), 545-548.

11. 3M Novec(TM) Fluorosurfactant FC-4430. (7/23/2008)

12. Lin, M. Simulation and Design of Planarizing Materials and Interfacial Adhesion Studies for Step and Flash Imprint Lithography. University of Texas, Austin, 2008.

CHAPTER 7

1. Dickey, M. Development of Photocurable Pillar Arrays Formed via Electrohydrodynamic Instabilities. University of Texas, Austin, 2006.

APPENDICES

1. Constantinou, L.; Gani, R.; O'Connell, J. P., Estimation of the acentric factor and the liquid molar volume at 298 K using a new group contribution method. *Fluid Phase Equilibria* **1995,** 103, (1), 11-22.

2. Marrero, J.; Gani, R., Group-contribution based estimation of pure component properties. *Fluid Phase Equilibria* **2001,** 183-184, 183-208.

Vita

Elizabeth Collister was born on January 29, 1979, in a suburb of Cleveland, Ohio. She is the daughter of Linda Collister, an obstetrics nurse, and Gary Collister, a machinist. She has an older brother Brian Collister born January 26, 1978. Her forays into research began in 1995 with an internship at NASA Lewis Research Center in polymer composites. She graduated as the salutatorian of the 1997 class of Midpark high school. She returned to NASA, now Glenn Research Center at Lewis Field for another internship with the combustion branch prior to college. She attended the University of Akron, located in Akron, Ohio. There she did undergraduate research with Dr. Ju and had co-op work periods with Parker Hannifin O-ring Division in Lexington, KY and Foxboro in Middleburg Hts, OH. She graduated summa cum laude in 2002 with a B.S. in Chemical Engineering as well as a polymer specialization and minors in Chemistry and Compute Information Systems. In fall 2002, Elizabeth enrolled in the University of Texas at Austin under the supervision of Dr. C. Grant Willson.

Permanent address: 7484 Briarcliff PkWy., Middleburg Hts., Ohio 44130

This dissertation was typed by the author